ABSTRACT

Title of Document:	TRANSVERSE CHARACTERIZATION AND CONTROL OF BEAMS WITH SPACE CHARGE
	Kamal Poor Rezaei, PhD, 2013
Directed By:	Professor Patrick G. O'Shea Professor Rami A. Kishek Department of Electrical & Computer Engineering

The characterization of the transverse phase space of beams is a fundamental requirement for particle accelerators. As accelerators shift toward higher intensity beam regimes, the transverse dynamics of beams becomes more influenced by interparticle forces known as the space charge forces. Therefore, it is increasingly important to take space charge into account in studying the beam dynamics. In this thesis, two novel approaches are presented for measurement of transverse emittance for beams with space charge, an important quality indicator of transverse phase space. It is also discussed the experimental work on orbit characterization and control done for space charge dominated beams of the University of Maryland Electron Ring (UMER).

The first method developed for measuring the emittance, utilizes a lens-drift-screen setup similar to that of a conventional quadrupole scan emittance

measurement. Measurements of radius and divergence that can be obtained from beam produced radiation, e.g. optical transition, are used to calculate the beam cross correlation term and therefore the rms emittance. A linear space charge model is used in the envelope equations; hence the errors in the measurement relate to the non-uniformity of the beam distribution. The emittance obtained with our method shows small deviation from those obtained by WARP simulations for beams with high space charge, in contrast to other techniques.

In addition, a second method is presented for determining emittance that works for beams with intense space charge and, theoretically, does not require an *a priori* assumption about the beam distribution. In this method, the same lens-drift-screen setup as the previous method is used, except that the beam size and divergence are scanned to find the minimum of product of the measured quantities. Such minimum is shown to be equal to the rms emittance under specific conditions that usually can be satisfied by adjusting the experiment parameters such as the drift length. The result of numerical analysis of the method done for a realistic accelerator confirms the applicability of method for intense beams with nonuniform distribution.

Finally, the experimental work for characterization and control of beam centroid motions in UMER are discussed. Such work is important because at high space charge intensities, the nonlinearities of the lenses impose stricter constraints on the swing of beam centroid in the pipe. On the characterization side, we show new methods for more accurate measurements of the average orbit of particles, including inside the quadrupoles where there is no monitor. Based on this more precise orbit information, the beam orbit is corrected and its result is presented.

TRANSVERSE CHARACTERIZATION AND CONTROL OF BEAMS WITH SPACE CHARGE

By

Kamal Poor Rezaei

Dissertation submitted to the Faculty of the Graduate School of the
University of Maryland, College Park, in partial fulfillment
of the requirements for the degree of
Doctor of Philosophy
2013

Advisory Committee:
Professor Patrick G. O'Shea, Chair/Advisor
Research Professor Rami A. Kishek
Professor Thomas M. Antonsen
Professor Victor L. Granatstein
Research Professor Ralph B. Fiorito
Professor Richard F. Ellis, Dean's representative

Dedication

To My Dear Wife
Elham Rasti

Acknowledgements

I am deeply grateful to many people who have helped me during my study and research at the University of Maryland. I would like to thank my advisor Dr. Patrick G. O'Shea for his invaluable guidance and enthusiastic support to this successful completion of my PhD dissertation. I wish to thank my co-advisor Dr. Rami A. Kishek for his direct assistance in the research and patient revisions of my papers and dissertation. He has led me into the accelerator physics field and provided me a positive environment of independent research. I would also like to thank Dr. Ralph B. Fiorito for his great comments and support throughout most of my research.

My thanks also go to Dr. Thomas M. Antonsen, Dr. Victor L. Granatstein, and Dr. Richard F. Ellis for serving on my PhD defense committee.

Moreover, I am thankful to all of the University of Maryland Electron Ring staff, Dr. David Sutter, Dr. Massimo Cornacchia, Dr. Irving Haber, Dr. Santiago Bernal, Dr. Timothy Koeth, and Dr. Brian Beaudoin as this work would have not been possible without their assistance and encouraging remarks. I am also grateful to the past and present fellow students of UMER, Dr. Christos Papadopoulos, Dr. Karen Fiuza, Yichao Mo, Kiersten Ruisard, William Stem, and Hao Zhang. I wish to express my gratitude to my best friend Dr. Mehdi Kalantari whose encouragement and support greatly helped me to embark on a path toward PhD. I also wish to thank Dr. John Power, Dr. Cecile Limborg, Dr. Manoel Conde, and Dr. Alex Friedman for the helpful discussions.

Most of all, I would like to thank my wife and my family for their support and love.

Table of Contents

List of Tables

List of Figures

Chapter 1: Introduction

It is important to measure, characterize, and control the transverse dynamics of beams to quantify the beam quality and match the optics in an accelerator beam line. The transverse beam emittance and beam trajectories are the main transverse properties of the beam that directly affect the beam sustainability in a circular accelerator and demand precise characterizations and control. Most beams of interest are space-charge-dominated near the source and low energy transport section, where the beam dynamics are mostly determined by interparticle forces rather than the beam pressure represented by emittance. In this work, we present methods for measuring emittance that take space charge into account. We also discuss the experimental work on orbit characterization and control done for space charge dominated beams of UMER.

Measuring emittance for high intensity beams poses the most challenges as space charge usually modifies and degrades the performance of emittance measurement methods such as quadrupole scan technique [1-5]. The quadrupole scan (or "quad-scan") is one of the simplest and most common methods used to measure emittance. In a quad-scan, the emittance can be deduced from measurements of beam radius as a function of the strength of a quadrupole upstream. Since space charge forces are a function of the beam radius, space charge confounds the analysis because an initial beam distribution has to be assumed *a priori* in order to calculate the space charge term. In the case of extreme space charge, quad-scans become ineffective since the beam radius is determined largely by space charge, and wide variations in emittance lead to negligible change in beam radius. Several amendments have been proposed in literature to enhance the accuracy of quadrupole scan method for high intensity beams [6-7].

From the symmetry of the expression for the rms emittance [8]

$$\tilde{\epsilon}^2 = < x^2 >< x'^2 > - < x \cdot x' >^2$$

it is obviously possible to determine emittance with a quadrupole scan technique using measurements of either the beam radius or divergence . The usual implementation of the method is to perform a quadrupole scan of beam size only. However, by measurement of both the near field and the far field angular distribution of optical radiation produced by interaction of the beam with foils (transition radiation), magnetic fields (synchrotron or edge radiation) or apertures (diffraction radiation), it is possible to obtain simultaneous, high-quality measurements of beam size and divergence [9-12].

In order to use these observables to determine the rms emittance at focus points other than a beam waist condition, which is not necessarily the same as a beam size minimum obtained by magnetic focusing, we need a methodology which relates the measured observables, i.e. divergence and beam size to the cross-correlation ($< x \cdot x' >$) term. We will show how this can be done by taking the cross-correlation term as a control variable for matching beam envelopes to their actual envelopes with the constraint that the beam radii and divergences at the screen are the same as measured values. First, we show that when space charge is negligible, emittance for either the horizontal or vertical plane can be given in a closed form in one plane either knowing a) the beam size and divergence at a minimum value of the size; or b) from any two values of beam radius and divergence measured in that plane. We then extend this later approach to determine emittance for the more general case of beams with space charge. Finally, we discuss the results of applying this approach to simulated beams with a prescribed value of emittance.

Circular accelerators and storage rings are among the most efficient ways of accelerating beams. It is desirable to keep the beam in the ring for a longer period of time. To achieve this goal, beam should be guided as close as possible along the axis of the ring shaped pipe. This requires specific beam orbit measurement and optimization techniques to be applied.

Small research rings are supposed to be configured for diverse beams with charge varying over a large range. Such rings have constraints on the orbit measurements and rely on relatively fewer numbers of steerers as well. In addition, they are more easily affected by environmental perturbations like Earth's magnetic field especially when they are operated at low energies. Therefore, beam steering optimization methods used for large rings is not fully applicable to such research rings. It was essential to develop fast and robust steering methods according to the imperfect nature of such small machines.

In this work, methods are proposed to address various issues in UMER, which is a good example of a small research ring, developed to study the dynamics of space charge dominated beams [13-14]. While my approaches and experiments are developed around specific needs of this ring, they are simply extendable to similar small and low energy machines.

The forces between particles in a beam, called space charge forces, can indirectly affect the orbit of beam centroid. Steering (orbit control) solutions developed for lower charge beams are not readily usable for medium to extreme space charge cases. Such high intensity beams are so sensitive to the lens nonlinearities and as such nonlinearities increases off-center toward the wall of the ring (especially for imperfect lenses used in research rings), beam excursions inside lenses should be limited more. In addition, space charge increases the strength of image charge forces, which consequently lead to larger centroid excursions inside the quadrupoles. Some experimental verification of these phenomena is presented in this thesis.

In small research rings there is no Beam position Monitor (BPM) inside or next to each quadrupole (mostly due to the lack of space) and thus orbit information is not known inside these important focusing elements. Because of the limited number of BPMs, the beam is under-diagnosed. Furthermore, as beam excursions have bigger amplitudes inside quadrupoles, beam

loss happens mostly inside these focusing elements. Therefore, it is important to know the beam centroid positions inside the quadrupoles. To address this problem, a method is presented which indirectly infers beam positions inside quadrupoles.

Optimizing beam injection is another subject as it is essential, especially for high SC beams, to have small betatron oscillations. In fact, a good orbit can be simply made useless by bad injection that leads to high beam excursions. A method has been presented to address this issue.

1.1 Previous Work & Background

Drs. Chris Papadopoulos [15] and Diktys Stratakis [l6] are the two UMER students who have done intensive work in measuring the beam emittance. Stratakis, in fact, worked on tomography techniques for characterizing the phase space of the beam. Obviously, from such measurements the emittance can be determined. He addresses the space charge problem throughout his research and finds approximation for emittance growth under the intense space charge.

Papadopoulos collaborated with Dr. Ralph Fiorito in 2009, which led to proposing a method for finding emittance from beam size and divergence measurements made by Fiorito. His method is based on calculating the emittance at minimum of the beam size scan. Such approach was only applicable to beams with negligible space charge, and therefore, it was necessary to extend this work and find approaches that could utilize size and divergence measurements to determine emittance for any beam including beams with space charge.

It should be noted that due to low energy nature of UMER, the divergence cannot be measured. This was shown experimentally by the work of Dr. Kai Tian [l7]. Therefore, my

proposed emittance measurements, which rely on knowing the beam divergence, could not be tested experimentally here in UMER.

As it was pointed out earlier the quadrupole scan is the most common method for measuring the emittance. References [1-5] cover application of the method to various accelerators and rings. Some work has been done to modify the quadrupole scan method so that it could be applied to beams with space charge. Dr. C. G. Limborg et al. [6] present a sophisticated method that apparently includes space charge; however, authors provided limited numerical results to confirm the accuracy of the method under the influence of space charge forces. Dr. J. Rosenzweig, *et al.* [18] present a comprehensive analysis of space charge force effects on emittance measurements, although their work does not provide any solution for canceling or limiting such effects.

Controlling the beam orbit has been very important for UMER and during the past few years many students have worked on this subject. While there have been many methods for beam steering in the rings such as harmonic correction [19], eigenvector method [20], orbit response matrix [21], and LOCO [22] past studies have shown that such techniques are not directly applicable to a research ring like UMER.

First beam steering activities for UMER were done by Drs. Hui Li [23] and Mark Walter [24-25]. Li developed algorithms for beam steering and envelope matching before the UMER ring was closed. His control technique used the linear optics theory and involved scanning the quadrupoles, taking beam photos at downstream phosphor screens, and computing resulting beam position changes. He also worked on beam injection. He was not much successful in this procedure, as the numbers of correctors in both planes were far less than the number of orbit control points around the ring. For instance, in the horizontal plane there are 36 dipoles as

correctors opposed to 72 quadrupoles. Therefore, a solution giving zero for beam orbit inside all quadrupoles theoretically could not exist. Overall, such steering works resulted in the multi-turn commissioning of UMER and laid the foundation for later steering research.

Walter used the quadrupole scan technique for beam centroid to find the centers of quadrupoles, which led to a coarse steering solution. He also set up an initial complete beam steering configuration; however, this method did not offer a good multi-turn solution. Although Walter's approach works for beam steering, it either leads to a local optimal steering solution, cannot converge easily, or even diverge.

Dr. Chao Wu [26-27] continued the job of beam steering and did many refinements to UMER beam orbits based on "Response Matrix" method. He applied the response matrix method to equilibrium orbit also known as "Closed Orbit" and through some iterations was able to refine the closed orbit considerably. The lowest current beam of UMER could survive in the ring for more than 1000 turns due to response matrix based smoothing of the closed orbit. However, several problems remained to be addressed in the later works. First, although the quality of the closed orbit was improved to a good extent, it was not acceptable for high current beams with intensive space charge. Second, as we can see later, the response matrix method is very dependent on good initial settings and therefore it was not possible to apply the technique immediately to new ring configurations or geometries. In fact, it was necessary to manually trim the orbit and make it acceptable for response matrix method by making the ring response linear. In addition, while the response matrix correction was successful for correcting closed orbit in the horizontal plane, it could not do much for smoothing vertical closed orbit. It was necessary to address this steering problem through my research.

Correcting injection was another issue that needed to be investigated. Past work by Chao relied on treating transport line steerers like ring dipoles and engaging them similarly through the response matrix. However, this approach cannot fine tune the injection parameters by minimizing betatron oscillations. A section of the chapter 6 is devoted to proposing a new systematical method for injecting the beam on closed orbit.

1.2 Organization of Thesis

The rest of the dissertation is organized as six chapters. In chapter two, we discuss the theoretical background of transverse beam dynamics. Next, in chapter three, we give a brief introduction to basics of beam measurements including size, divergence, emittance, and finally the closed orbit.

In chapter four, first, we discuss the proposed method for measuring emittance of beams with space charge, and then we present the extensive numerical results of testing the method for various grades of space charge. In chapter five, another novel method for including space charge in emittance measurements is discussed. The chapter ends with providing the simulation analysis of the method for a specific linear accelerator. Next, we present our experimental studies of UMER orbit characterization and control throughout four sections.

Finally in chapter seven, we draw conclusions and list suggested ideas for related experiments and simulations that could assist in continuing the exploration on measuring emittance and orbit control for beams with space charge.

Chapter 2: Theoretical Background of Beam Transverse Dynamics

In this chapter, first, we review some concepts of transverse beam physics followed by the beam emittance basics in section 2.1. A basic discussion of Courant Snyder theory is given in the section 2.2. Finally, we introduce the space charge dynamics and then the envelope equations in section 2.3.

2.1 Fundamental Concepts of Beam Dynamics

2.1.1 Phase Space Representation of Beam

In Classical Physics, a charged particle is well described by its position (x, y, z) and velocity (v_x, v_y, v_z), in addition to its mass m and charge q. In the case of a beam, the movement of the charged particles is highly directional along longitudinal direction, which we define to be z. The other two components of the velocity specify the motion in the plane perpendicular to the z, which together with x and y specify the transverse phase space coordinates of the particle. As the velocity along z is far higher than the transverse velocities, we can thus utilize the so-called paraxial approximation [28], and simplify the analysis by defining slope variable x' and y' as:

$$\begin{cases} x' = \dfrac{dx}{dz} = \dfrac{v_x}{v_z} \\ y' = \dfrac{dy}{dz} = \dfrac{v_y}{v_z} \end{cases} \tag{2.1}$$

The angles x' and y', closely related to the velocities v_x and v_y are used in conjunction with x and y as the trace space coordinates of the particle.

To fully specify the particle, it is also necessary to take z and Δv_z into account hence each particle's status is determined by a 6 dimensional system. It is presumed that all the

particles have the same longitudinal velocity v_z , and hence the dimensionality of the problem can be reduced from 6 to 4. This is the case where the beam is an infinitely long cylinder, and therefore, the transverse dynamics is decoupled from the longitudinal physics. Throughout the dissertation, it is also assumed that the beam is not being accelerated as it travels along the transport channel. Hence, the longitudinal velocity v_z is taken to be constant, unless otherwise indicated.

Given above mentioned assumptions, the most general description of the beam can be obtained with a Probability Density Function (PDF), $f = f(x, x', y, y')$, which is a function of 4-dimensional phase space (x, x', y, y'). Moments of the distribution for a general function g can be written as:

$$\langle g \rangle = \int\int\int\int g \; f(x, x', y, y')\, dx \; dx' dy \, dy' \tag{2.2}$$

The rms beam size and the rms beam divergence are the two average quantities or moments that are important in characterizing the transverse space. These moments are defined by the following relations:

$$x_{rms} = \sqrt{\langle x^2 \rangle} = \left(\int\int\int\int x^2 \; f(x, x', y, y')\, dx \; dx' dy \, dy' \right)^{\frac{1}{2}} \tag{2.3}$$

and,

$$x'_{rms} = \sqrt{\langle x'^2 \rangle} = \left(\int\int\int\int x'^2 \; f(x, x', y, y')\, dx \; dx' dy \, dy' \right)^{\frac{1}{2}} \tag{2.4}$$

Likewise, similar rms values can be defined for the y plane. It should be noted that, in general, rms quantities of x and y might not to be equal. The beam divergence is related to the beam temperature T in the corresponding transverse direction, as shown here:

$$k_B T_u = \gamma m {v_z}^2 u'^2 \tag{2.5}$$

where k_B is Boltzmann's constant, and u represents either of the x or y planes.

2.1.2 Emittance

In this dissertation emittance always refers to the transverse emittance. Emittance, a major quality indicator for the beam, is used to measure the random thermal motions of the particles in the beam. As figure 2.1 shows, for a beam with low emittance, the particles inside the beam tend to keep moving parallel to each other, while for a high emittance beam, they seem more diverging from each other.

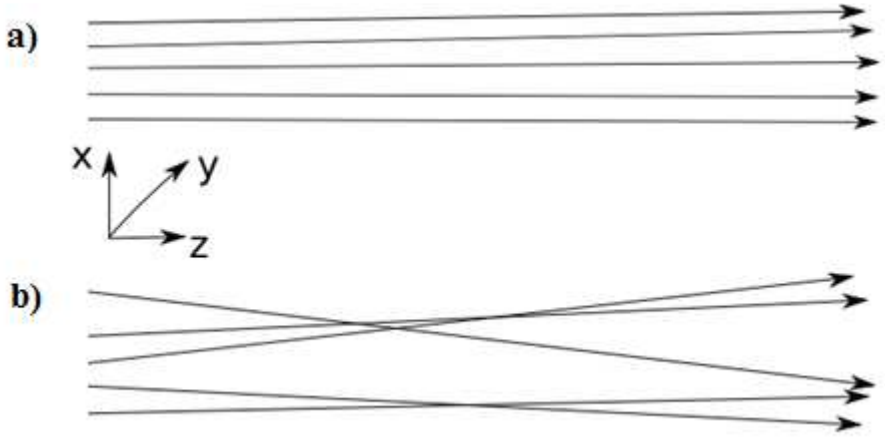

Figure 2.1: (a) Laminar or low emittance beam and (b) High emittance beam.

Different definitions of emittance are given in the literature, however, emittance can be best described as a measure of the compactness of the phase space occupied by the particles. Based on this view of emittance, it can be defined as the effective area of phase space or trace space distribution. The emittance calculated this way is known as the total emittance, ϵ_t. When there is no acceleration, this area is constant even if the particles go under nonlinear focusing

forces. This may be regarded as a disadvantage for this definition of emittance as it cannot show the effect of nonlinear forces on the beam. Figure 2.2 shows a sample trace space with an ellipse encompassing the majority of beam particles. In the next section, we will see that for linear forces such area can always be represented as an ellipse.

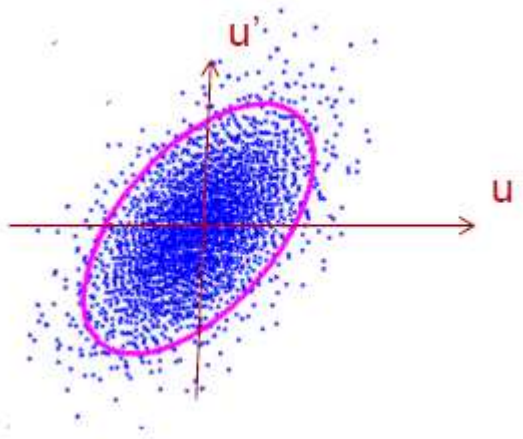

Figure 2.2: A typical trace space with an ellipse encompassing the effective part of the beam [Limb].

The rms emittance is defined as the product of the beam rms size and rms divergence while the cross-correlation between these two quantities are known and taken into account. Such cross-correlation is calculated from the general moment given in Eq. (2.2) as:

$$\langle xx' \rangle = \int\int\int\int xx' \; f(x, x', y, y') \, dx \; dx' dy \, dy' \tag{2.6}$$

Starting at the source, cross-correlation is zero as it is expected due to the randomness of particle emission from the cathode. As we will see, in beam focusing elements, forces applied to particles are proportional to x which leads to non-zero values for cross-correlation for most parts of the lattice. In fact, the cross-correlation term is negative if the beam is contracting with increasing z and positive if the beam is expanding. Based on these, the rms emittance can be calculated from rms beam size, divergence and cross-correlation through the following equation:

$$\tilde{\epsilon}_x = \sqrt{\langle x^2 \rangle \langle x'^2 \rangle - \langle xx' \rangle^2} \tag{2.7}$$

Likewise, y rms emittance can be written in terms of corresponding y plane quantities. As was the case with size and divergence, the emittances in x and y might not be equal. We will use mostly this definition of emittance throughout this dissertation. The unit usually used for emittance is $\mu m - rad$, which is often written as μm.

For a specific beam distribution where all particles lie uniformly inside an ellipse, the rms values can be related to maximum values of size and divergence by a factor of 2 [28]. This leads to another definition known as the effective emittance, which can be expressed as:

$$\epsilon_x = 4\tilde{\epsilon}_x = 4\sqrt{\langle x^2 \rangle \langle x'^2 \rangle - \langle xx' \rangle^2} \tag{2.8}$$

Similar to the total emittance, both the effective and rms emittances are conserved under the linear focusing forces. However, if there is acceleration all these emittances change. It is helpful to modify the latest emittance formulas so that they preserve their values by acceleration. This modification comes from the factor, $\beta\gamma$, where β and γ are relativistic parameters defined as $\beta = v_z/c$ and $\gamma = (1 - \beta^2)^{-1/2}$ where c is the speed of light [29]. The emittances defined by a product of rms and effective emittances with this factor are known as normalized rms or normalized effective emittance and is shown as $\tilde{\epsilon}_{nx}$ and ϵ_{nx}:

$$\tilde{\epsilon}_{nx} = \beta\gamma\sqrt{\langle x^2 \rangle \langle x'^2 \rangle - \langle xx' \rangle^2} \tag{2.9}$$

and similarly with an extra factor of 4 for ϵ_{nx}.

The table 2.1 summarizes all the widely used emittance definitions and their properties regarding variation with energy (acceleration) and linear or nonlinear focusing forces.

Table 2.1: Widely used emittance definitions and their properties [30].

Type	**Origin**	**Linear Forces**	**Non-linear Forces**
Total Emittance, ϵ_t	Conservation of phase space	Conserved	Conserved
RMS Emittance, $\tilde{\epsilon}$	Average over distribution	Conserved	Not Conserved
Effective Emittance, ϵ ($4\times \tilde{\epsilon}$)	Correspond to total emittance of uniform beam	Conserved	Not Conserved

Although the beam emittance is a quality indicator for beam, generally, it is not enough to have beams with mere low emittance preserved over the whole length of the lattice. One can reduce the beam emittance by using slits or holes, however this reduces the total current of the beam as well. In fact, it is the number of particles for a given emittance that counts for beam quality. Hence, a quantity known as *brightness* and is defined as $B = dJ/d\Omega$ which is current per unit solid angle is introduced. Brightness is a measure of the density of particles in phase space. Often, it is more convenient to use the averaged brightness, which is directly related to the beam emittance. In exact mathematical formulation, the average beam brightness, as a quantitative measure to the concept of beam quality, is given as:

$$\bar{B} = \frac{I}{8\pi^2 \tilde{\epsilon}_x \tilde{\epsilon}_y} \tag{2.10}$$

Therefore, how small the emittance should be for a specific application depends directly on how much current the beam has. High brightness requires both high current and low emittance in the x and y directions. The emittance of 10 μm may seem a good value for a current of 100 mA, however, for the beam current of 10 mA the emittance should be decreased as low as 1 μm to have the same beam brightness. Finally, it should be pointed out that normalized brightness can be defined by using normalized emittances at the denominator of Eq. (2.10).

2.2 Courant-Snyder Theory

The Courant-Snyder theory presents the general solution for beam size and divergence variation in an accelerator structure [31]. We start from the single particle equation of motion for a beam transport channel. The periodic focusing channel is the simplest focusing channel, where the external force applied to confine the beam is periodic in s, and a linear function of distance from the beam axis. Such focusing force is given by:

$$F_Q(r) = m{v_z}^2 \kappa\, r \tag{2.11}$$

where m is the mass of beam particles, κ is a measure of the focusing strength and r can be either of x or y. The single particle equation of motion in x plane is given in literature as [?]:

$$x'' + \kappa(s)x = 0 \tag{2.12}$$

where $\kappa(s)$ is a periodic function with lattice period S:

$$\kappa(s + S) = \kappa(s) \tag{2.13}$$

The general solution to the motion equation can be written as:

$$x(s) = Aw(s)\cos(\psi(s) + \phi) \tag{2.14}$$

This solution is quasi-periodic with the phase term, $\psi(s)$, and the amplitude term, $w(s)$. The derivative of the phase term, $\psi'(s)$ is given as:

$$\psi'(s) = \frac{1}{w(s)^2} \tag{2.15}$$

By plugging the solution (2.14) into Eq. (2.12) and writing the equation in terms of only w(s), using the Eq. (2.15), we receive the following equation of motion:

$$w(s)'' + \kappa(s)w(s) - \frac{1}{w(s)^3} = 0 \tag{2.16}$$

To know the trace space shape and area, we can calculate the x' and then use the envelope equation for $w(s)$ to obtain the following relation between x and x':

$$\left(\frac{1}{w(s)^2}+w'(s)^2\right)\,x(s)^2-2w(s)w'(s)x(s)x'(s)+w(s)^2x'(s)^2=A^2 \tag{2.17}$$

We can write this equation in the following form:

$$\hat{\gamma}\,x^2+2\hat{\alpha}\,xx'+\hat{\beta}\,x'^2=\tilde{\epsilon}_x \tag{2.18}$$

where, implicitly, all variables are functions of s.

The Eq. (2.18) describes an ellipse in trace space and the $\hat{\alpha}$, $\hat{\beta}$, and $\hat{\gamma}$ are known as Courant Snyder parameters. These parameters are equal to their corresponding factors of x^2, xx', and x'^2 in Eq. (2.17). Of these parameters, $\hat{\beta}$ is known as beta function and it represents the beam envelope (for so-called emittance dominated beam; see section 2.3). In fact, one can determine the $\hat{\beta}\,(s)$ for a lattice and calculate all other two parameters from the following equations:

$$\begin{cases}\hat{\alpha}=-\dfrac{\hat{\beta}'}{2}\\ \hat{\gamma}=\dfrac{1+\hat{\alpha}^2}{\hat{\beta}}\end{cases} \tag{2.19}$$

Notice that we replaced the A^2 with the rms emittance, $\tilde{\epsilon}_x$. This means that the ellipse with $A^2=\tilde{\epsilon}_x$ is the largest ellipse that particles in trace space can be found on. Obviously, all other particles with smaller amplitudes lie inside this ellipse. Figure 2.3 shows a typical ellipse highlighting several important points on the circumference of the ellipse.

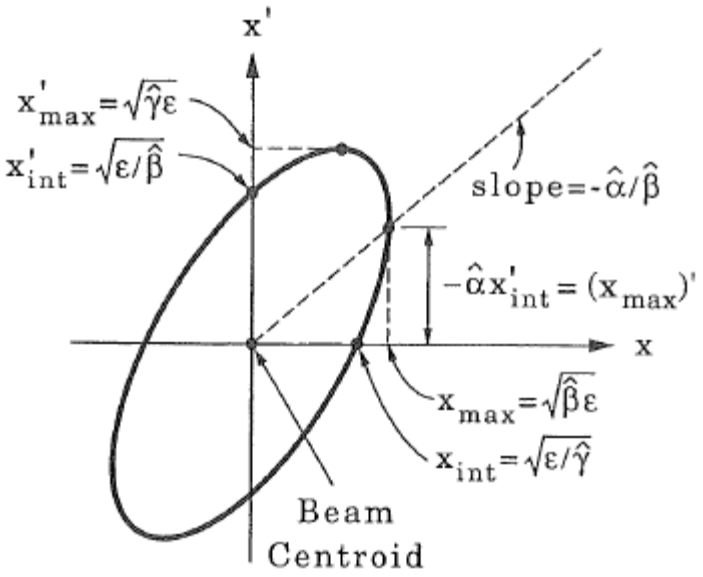

Figure 2.3: Trace space ellipse described by equation $\hat{\gamma}\, x^2 + 2\hat{\alpha}\, xx' + \hat{\beta}\, x'^2 = \tilde{\epsilon}_x$, and relations of some important points [28].

2.3 Beam Transport Under Space Charge

In beam transport, there are two factors causing the expansion of the beam. One is space charge, originating from the self-forces of similarly charged particles inside the beam which is generally known as space charge forces; the other is the emittance, coming from the thermal motion of particles. External focusing is applied to counteract these two forces and prevent the beam from expansion. In this section, we discuss a quantitative measure to include space charge forces in beam transport through envelope equation.

2.3.1 Modeling Space Charge

The generation and transport of electron beams with high brightness and low emittance is constrained by the mutual repulsion among electrons, which is known as space-charge. Intense beams consist of many charged particles that can create magnetic and electric fields. In a simplistic beam distribution where all beam particles lie inside a cylinder with radius R, we can

calculate such forces. According to the figure 2.4, the electric field at the distance r from the axis of the beam can be derived by using Guess theorem as:

$$E_r = \frac{Ir}{2\pi\varepsilon_0 R^2 v_z} \quad , r < R \tag{2.20}$$

where I is the beam current, and ε_0 is the free space permittivity. Likewise, the azimuthal magnetic field at r can be derived by using Ampere's law as:

$$B_\theta = \frac{\mu_0 Ir}{2\pi R^2} \quad , r < R \tag{2.21}$$

where μ_0 is the free space permeability.

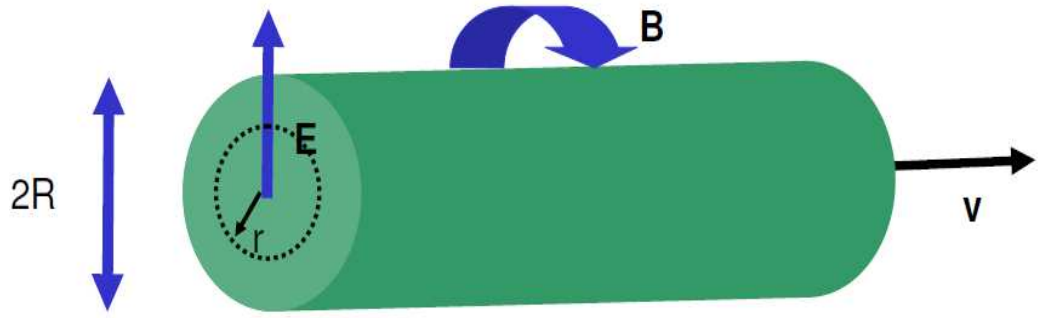

Figure 2.4: Diagram showing the pillbox model of the beam with radial electric and azimuthal magnetic fields [30].

The electric field is along r, while the magnetic field is along θ. By using the relation $\mu_0\varepsilon_0 = \frac{1}{c^2}$, the magnetic field can be written in terms of electric field as:

$$B_\theta = \frac{v_z E_r}{c^2} \tag{2.22}$$

These fields can result in a net repelling force on a test charge particle located at r given by:

$$F = q(E_r - v_z B_\theta) = q\left(1 - \frac{{v_z}^2}{c^2}\right)E_r = \frac{qE_r}{\gamma^2} \tag{2.23}$$

In general, this self-field force combined with external focusing forces applied through magnetic lenses (e.g. quadrupoles) determines the motions of particles inside the beam and consequently the beam envelope. One immediate implication of Eq. (2.23) is that when the beam is relativistic (v_z comparable to c) space charge force becomes negligible as both electric and magnetic field forces cancel each other. In other words, space charge is more important for non-relativistic, low and medium energy beams. For relativistic beams, single particle behavior dominates and each particle moves only under the influence of the external focusing forces. However, near the source, where the energy is low, space charge becomes comparable to the external fields. In such high space charge regions, the particle-to-particle interactions occurring through the Coulomb forces give way to collective behavior of particles. In this case, the beam can be viewed as a non-neutral plasma where the average focusing forces replace the neutralizing background [28].

The uniform distribution we used for modeling the space charge forces is generally known as Kapchinskij-Vladimirskij (KV) distribution [32]. It provides a simple model for theoretically analyzing beam behavior affected by all factors mentioned above. In this model, as we saw earlier, the space charge force is linear and the beam phase space area, represented by emittance, remains constant. In reality, for the forces to be linear in the transverse direction, the paraxial approximation must be satisfied and the changes in the beam envelope must occur slowly enough for the longitudinal forces to be negligible.

2.3.2 Beam Envelope Equations

To derive the equation for beam envelope, we start from the single particle equation of motion for a beam transport channel. The smooth focusing channel is the simplest focusing channel, where the external force applied to confine the beam is constant in z, azimuthally symmetric and a linear function of distance from the beam axis. As we saw in section 2.2 such focusing force is expressed by Eq. (2.11). The single particle equation of motion in x plane, given in Eq. (2.12), can be modified to include the space charge linear forces as [33]:

$$x'' + \left(\kappa - \frac{K}{R^2}\right)x = 0 \tag{2.24}$$

where dimensionless quantity,

$$K = \frac{qI}{2\pi\epsilon_0 m(c\beta\gamma)^3} = \frac{2I}{I_0(\beta\gamma)^3} \tag{2.25}$$

is defined as the generalized perveance representing space charge defocusing forces. In Eq. (2.25), I is the beam current and I_0 is the characteristic current given by:

$$I_0 = \frac{4\pi\epsilon_0 mc^3}{q} \tag{2.26}$$

For electrons, $I_0 = 17000\ A$. The evolution of the beam envelope size, R, can be obtained by taking moments of Eq. (2.24) as:

$$\begin{cases} R_x''(s) + \kappa\, R_x(s) - \dfrac{K}{R_x(s)} - \dfrac{\epsilon_x^2}{R_x(s)^3} = 0 \\ R_y''(s) + \kappa\, R_y(s) - \dfrac{K}{R_y(s)} - \dfrac{\epsilon_y^2}{R_y(s)^3} = 0 \end{cases} \tag{2.27}$$

where s denotes the longitudinal variable along the beam path, and the derivations are calculated with respect to ds. One realistic implementation of a smooth focusing channel is a long solenoid magnet. For a solenoid channel, if a round beam enters the channel, it remains round although x and y emittances may still be different. Normally, emittances are the same and we can have the

same envelope equation for both planes. Eqs (2.27) are known as nonlinear second-order ordinary differential equation (ODE), and a closed form solution can be given for it. Hence, it should be solved numerically in packages like MATLAB [34-35].

On the other hand, the transport channel may be non-uniform and non-axisymmetric. In this case, the transport channel is comprised of magnetic or electric quadrupoles. Quadrupoles focus in one transverse plane while defocusing in the other plane and by reversing their polarity, we can exchange the directions of focusing and defocusing. Hence, by placing magnets of alternating polarity along a transport channel, the beam is focused on average. It should be noticed that for such channel, the beam has no longer an azimuthal symmetry, and the beam envelope is described by two following coupled equations:

$$\begin{cases} R_x''(s) + \kappa\, R_x(s) - \dfrac{2K}{R_x(s) + R_y(s)} - \dfrac{\epsilon_x^2}{R_x(s)^3} = 0 \\ R_y''(s) - \kappa\, R_y(s) - \dfrac{2K}{R_x(s) + R_y(s)} - \dfrac{\epsilon_y^2}{R_y(s)^3} = 0 \end{cases} \tag{2.28}$$

As can be seen from Eqs. (2.28), the coupling results from the space charge factor (generalized perveance) K. Therefore, for the case where space charge is negligible (e.g. highly relativistic beam) the x and y envelope equations can be treated independently.

The solutions of beam envelope equations are in general oscillatory, however, in the case of a uniform focusing channel; there is a roughly constant solution that can be obtained by plugging $R_x''(s) = 0$ in Eq. (2.27). This case is commonly referred to as a matched beam, and the matched beam radius R_m is calculated as:

$$\kappa\, R_m = \frac{K}{R_m} + \frac{\epsilon_x^2}{{R_m}^3} \tag{2.29}$$

The beam envelope equation is essentially a balance between three forces, namely the external focusing force, F_{foc}, the internal space charge defocusing force, F_{sc}, and the emittance

defocusing force, F_{em}. Obviously, for a matched beam we have:

$$F_{foc} = F_{sc} + F_{em} \tag{2.30}$$

The dimensionless ratio of internal space charge forces to external focusing forces is defined as the intensity parameter, , and can be derived as:

$$\chi = \frac{F_{sc}}{F_{foc}} = \frac{K}{\kappa {R_m}^2} \tag{2.31}$$

This parameter, accepting values between 0 and 1, is a measure of space charge effects for a matched beam. Generally, beams are classified as two categories based on value of χ. In the case of $\chi < 0.5$ the emittance term is dominant, and hence the beam is said to be emittance dominated beam, while for $\chi > 0.5$ the beam is called to be space charge dominated.

Chapter 3: Introduction to Beam Measurements

This chapter mainly discusses major transverse beam parameter measurements. As the proposed emittance determination methods of chapters 4 and 5 are relying on beam size and divergence measurements, the first section describes the techniques for measuring them. Then next section presents the two conventional approaches for measuring the emittance. The chapter continues with the discussion of beam centroid dynamics and, especially, how perturbations may affect the beam centroid motions. Finally, last two sections give brief introductions of two accelerators that are used for experiments or simulations.

3.1 Determining Beam Size and Divergence

Measuring the beam size is a routine operation in accelerator facilities. The most widely used method is to place a YAG or phosphorous screen on the beam line. When the charged particles hit the screen, photons are emitted and the optical image taken by a CCD camera truly represents the transverse distribution of the beam particles. The beam divergence is also directly measurable, either by a pinhole, which is a common method for measuring the divergence in laser beams, or by measuring the properties of the Optical Transition Radiation (OTR) emitted when the particle beam passes through a metallic foil.

Optical Transition Radiation is a well-known diagnostic tool to measure the beam distribution as well as beam size and divergence [9]. When a charged particle beam with a constant velocity passes through two different mediums with different dielectric constants, for example, from the vacuum to a metal plate, the fields generated from the particle beam will change quickly and some of the field energy is converted to optical transition radiation [36]. This

process can also be described by a collapsing electrostatic dipole. As the charge particle beam approaches the metal surface, the image charge is also approaching the metal surface. When it reaches the surface and stops suddenly, radiation is generated.

Ginsburg and Frank made the first theoretical prediction of the OTR in 1945 [37]. The first use of OTR as a beam diagnostic tool was made in 1979 by Wartski. He demonstrated that for a highly relativistic beam the OTR image could be used to measure the beam intensity profile, and the angular distribution of the OTR pattern can be used to measure its energy [17]. Since then, OTR has been widely used for measurement of the beam size, divergence and energy.

3.1.1 Setup for Optical Transition Radiation

Figure 3.1 shows the diagram of OTR setup used for imaging both the beam intensity profile and its divergence [10]. A thin metallic foil placed on the beam line is the pivotal part of any OTR system. When the beam particles hit this thin foil, it produces both forward and backward OTR radiation. The backward radiation is generated when the beam enters the metallic foil from the vacuum and the forward OTR is generated when the beam enters the vacuum from the foil. The magnitude and angular distribution of both radiations are similar. However, the center of backward OTR intensity is in the direction of optical reflection of the incident beam and that of the forward OTR is aligned with the direction of beam propagation [38]. In order to measure the beam divergence, an OTR interferometer comprised of two parallel thin metallic foils oriented 45 degree with respect to the incident beam, is used. The forward OTR from the first foil and the backward OTR from the second foil give rise to interference patterns which their visibility can be used to calculate the rms beam divergence when the distance between these two foils is comparable with the vacuum coherent length [11].

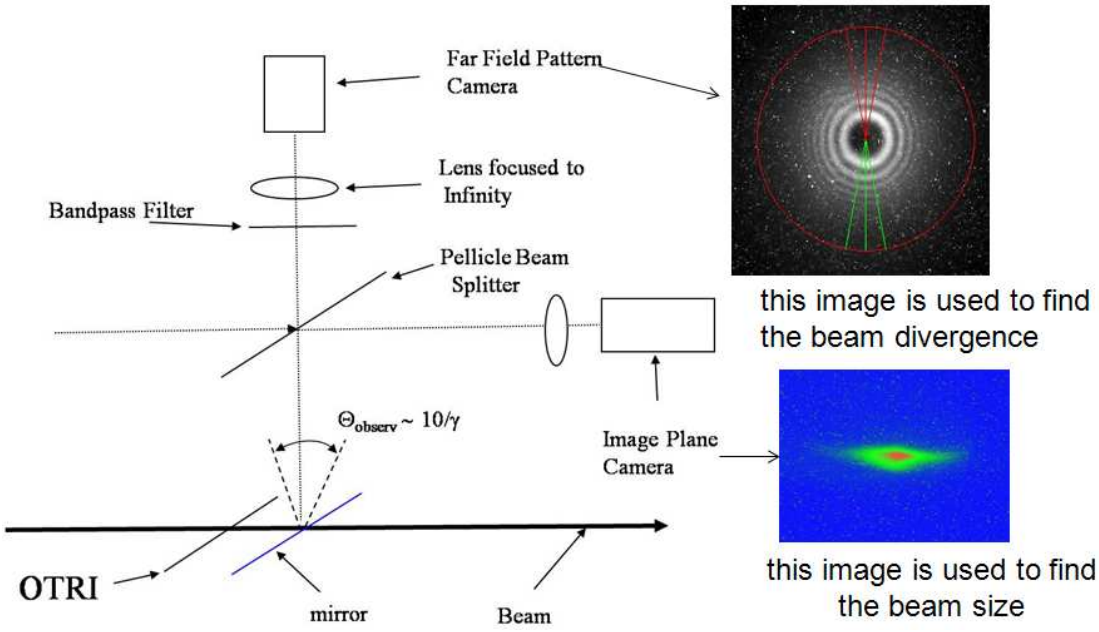

Figure 3.1: The diagram of OTR setup for imaging the beam size and divergence [9].

The angular distribution of OTR radiation, produced by a single electron incident on a perfect conductor, can be described as [11]:

$$\frac{d^2W}{d\omega d\Omega} = \frac{e^2\beta^2}{4\pi^2 c}\left(\frac{\sin(\theta - 2\psi)}{1+\beta\cos(\theta - 2\psi)} + \frac{\sin(\theta)}{1+\beta\cos(\theta)}\right) \tag{3.1}$$

where W is the energy of the radiation, ω is the angular frequency of the radiation, Ω is the solid angle, e is the electron charge, and β is the velocity of the electron divided by the speed of light. The observation angle in the horizontal plane, , is formed by the velocity vector of the electron $\boldsymbol{V}$ and ψ is the angle between $\boldsymbol{V}$ and normal to the screen unit vector, $\boldsymbol{n}$. Figure 3.2 illustrates the orientation of the OTR imager relative to the incident beam and also the field of view of the OTR radiation.

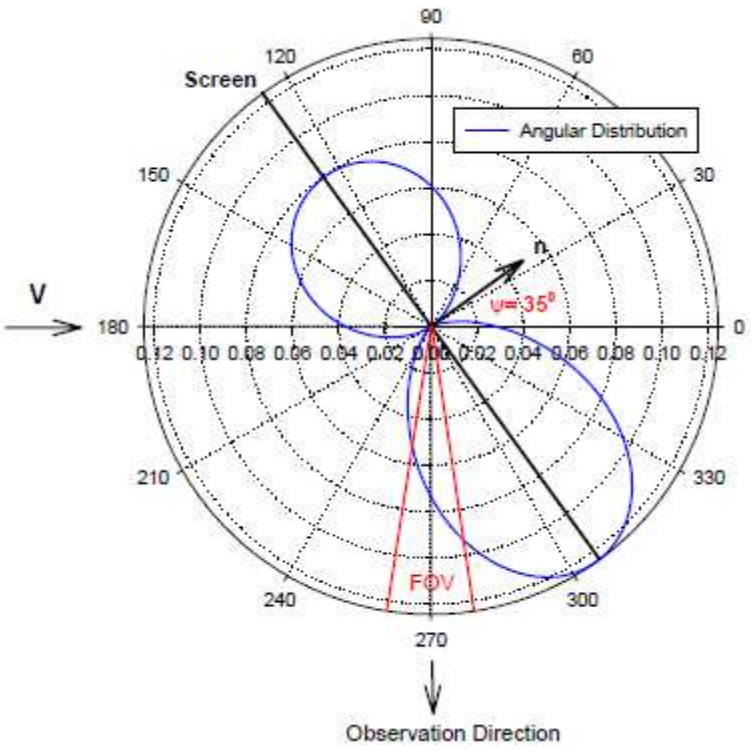

Figure 3.2: Typical OTR radiation pattern [12].

3.1.2 OTR Interferometry for Measuring Beam Divergence

As scattering in the first foil of the OTR interferometer dominates and obscures the beam divergence, conventional OTR interferometry cannot be used for low emittance beams. Ralph and Anatoly have shown that to overcome this problem, a perforated foil (mesh) can be used in front of the first foil in combination with a solid mirror after the second foil [11].

For low energy beams the inter foil spacing, $L \sim \gamma^2\lambda$, is too small to observe the interferences of forward Optical Diffraction Radiometry (ODR) from the mesh and backward OTR from the mirror. For example, at beam energy of 8 MeV and wavelength of λ=632nm, L becomes less than 1 mm. A transmission interferometer using a transparent dielectric foil as a second foil can be used to address this limitation. The forward ODR produced by the mesh passes through the dielectric foil and interferes with forward radiation produced by the dielectric itself. A transport mirror is used to redirect the interfering radiations into the optical

measurement system as can be seen in figure 3.3. Based on this, an optical diffraction dielectric foil transmission interferometer was designed and used to measure the divergence of the Argonne National Labs Advanced Wakefield Accelerator operating at 8 − 14 MeV [11].

The above mentioned researchers use the codes BEAMDR and CONVD, described in [39], to calculate the interference pattern produced by the ODR from the mesh and the dielectric foil radiation. The code CONVD considers the full radiation properties of the dielectric and also takes into account the refraction, reflection, and attenuation of radiation from the mesh. The code CONVD needs the exact values of thickness and refractive index of the dielectric foil. In order to find these values, the OTR produced by the low energy beam passing through a single metallic foil and also the radiation from interferometer produced by the same beam are recorded. Figure 3.4 shows the angular distributions of the OTR in left image and the radiation from interferometer in right image. Corresponding vertical scans of intensity are shown in figure 3.5 as dashed lines with red as interferometer and blue as OTR. Fitting of the experimental dashed curves and theoretical solid curves allows finding the beam and interferometer parameters including the thickness of the dielectric foil used in the interferometer.

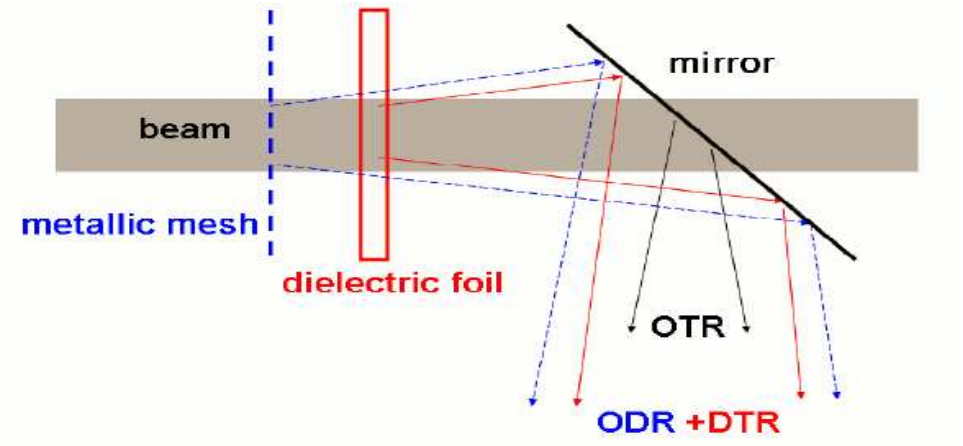

Figure 3.3: Mesh-dielectric foil transmission interferometer [12].

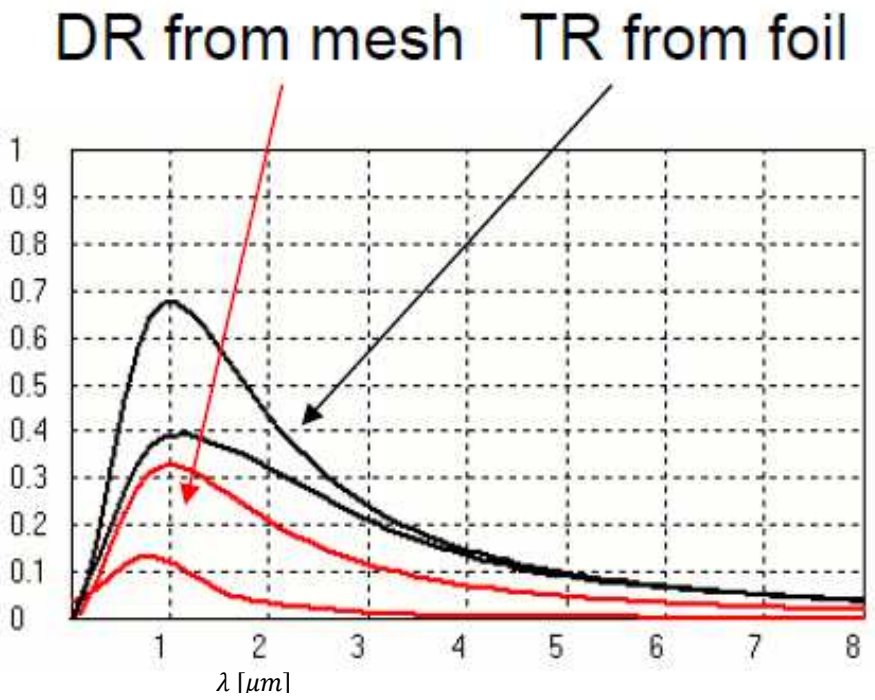

Figure 3.4: Normalized spectrum of Diffraction Radiation (DR) from the mesh and Transition Radiation (TR) from the foil of OTR setup in figure 3.3 [12].

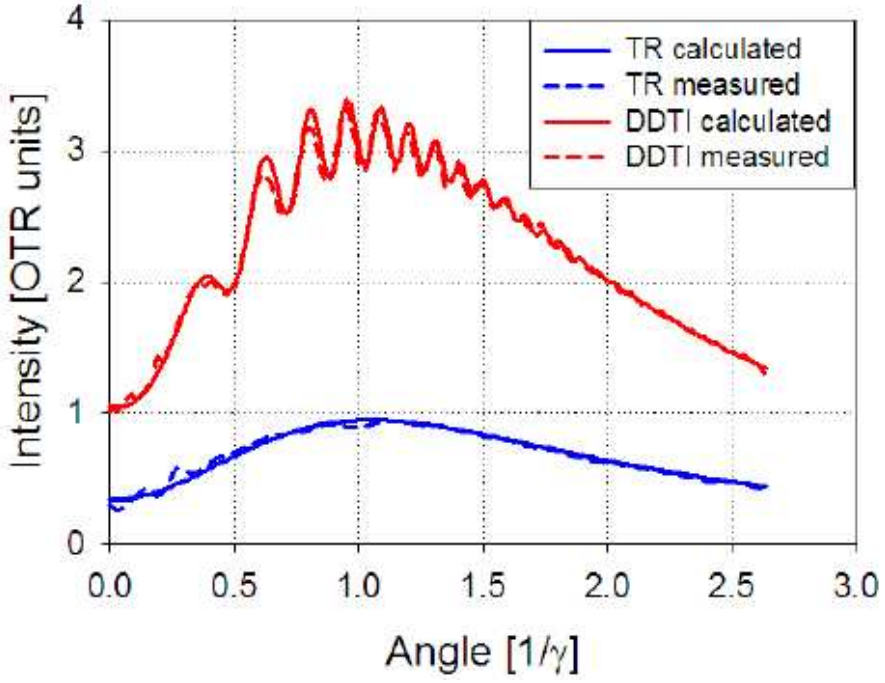

Figure 3.5: Measured and calculated angular distribution of radiation from metallic foil and interferometer [12].

3.2 Standard Techniques for Emittance Measurement

In this section, we discuss about the common techniques for measuring the emittance and report their advantages and disadvantages. Two well-known and mostly used of such methods are quadrupole scan and pepper pot.

3.2.1 Quadrupole Scan technique

In qudrupole scan method, the focal strength of the quadrupole is changed to have different beam sizes on a screen at distance L from the lens [4]. It can be shown that for an emittance dominated beam a quadratic can be fitted to beam size scan curve, and emittance can be determined as a parameter of the quadratic fit [40]. Figure 3.6 shows a typical setup for quadrupole scan. The screen usually is the first foil of the OTR setup.

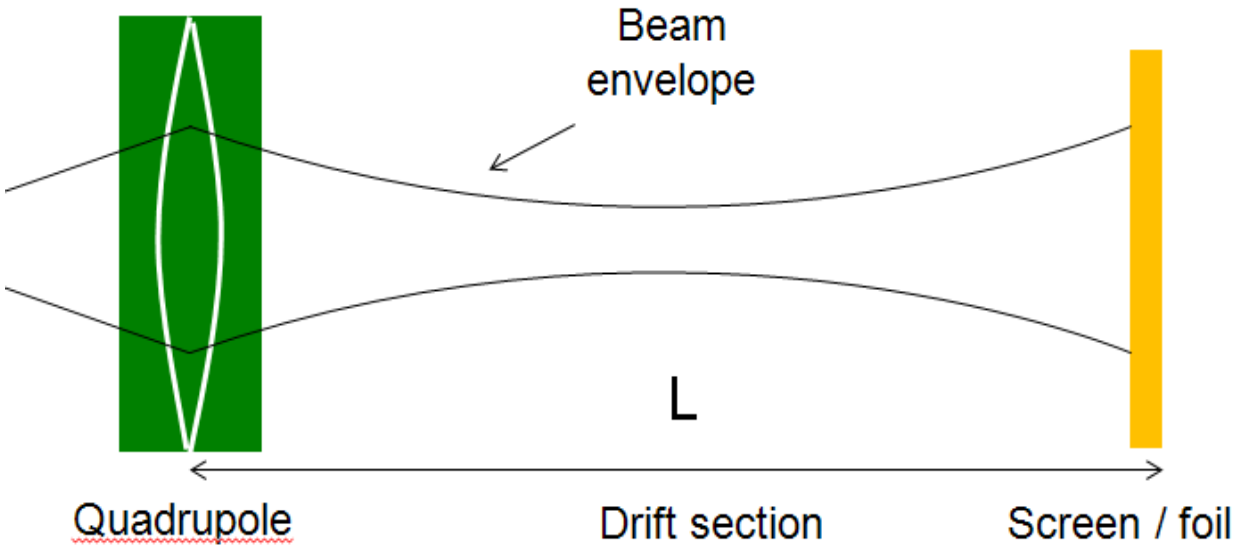

Figure 3.6: Typical quadrupole scan experiment setup.

As it was discussed in the precious chapter, the beam phase space can be described by an ellipse with Courant-Snyder (CS) parameters $\hat{\alpha}$, $\widehat{\beta}$, and $\hat{\gamma}$. We can write the CS parameters at the screen in terms of CS parameters at the lens through following equation [29]:

$$\begin{bmatrix} \hat{\beta}_S \\ \hat{\alpha}_S \\ \hat{\gamma}_S \end{bmatrix} = \begin{bmatrix} {m_{11}}^2 & -2m_{11}m_{12} & {m_{12}}^2 \\ m_{11}m_{21} & m_{11}m_{22} + m_{21}m_{12} & -m_{12}m_{22} \\ {m_{21}}^2 & -m_{21}m_{22} & {m_{22}}^2 \end{bmatrix} \begin{bmatrix} \hat{\beta}_Q \\ \hat{\alpha}_Q \\ \hat{\gamma}_Q \end{bmatrix} \tag{3.2}$$

where m_{ij} are the elements of the transfer matrix between the lens and the screen. The square of beam size at screen is related to the CS parameters at the initial position through:

$$\tilde{x}^2 = \hat{\beta}_S\tilde{\epsilon} = {m_{11}}^2\hat{\beta}_S\tilde{\epsilon} - 2m_{11}m_{12}\hat{\alpha}_S\tilde{\epsilon} + {m_{12}}^2\hat{\gamma}_S\tilde{\epsilon} \tag{3.3}$$

Transfer matrix for the drift section of the quadrupole scan setup can be obtained as:

$$T_{QS} = \begin{bmatrix} m_{11} & m_{12} \\ m_{21} & m_{22} \end{bmatrix} = \begin{bmatrix} 1 & L \\ 0 & 1 \end{bmatrix} \begin{bmatrix} 1 & 0 \\ -\frac{1}{f} & 1 \end{bmatrix} \tag{3.4}$$

In the quadrupole scan technique, the CS parameters at the screen can be found by measuring beam size corresponding to the several values of the focal strength $\frac{1}{f}$. Then by measuring the beam size at that point as a function of the quadrupole focusing strengths and curve fitting the data we can obtain $\hat{\beta}_Q$, $\hat{\alpha}_Q$, $\hat{\gamma}_Q$, as well as the emittance. A typical scanned data with the quadratic curve-fitting is shown in figure 3.6. It should be pointed out that the mentioned technique can only be applied to emittance dominated beams. As we will see in the next chapter, by going to high space beam, there are huge errors associated with determining emittance with CS parameter fitting for beams with high space charge.

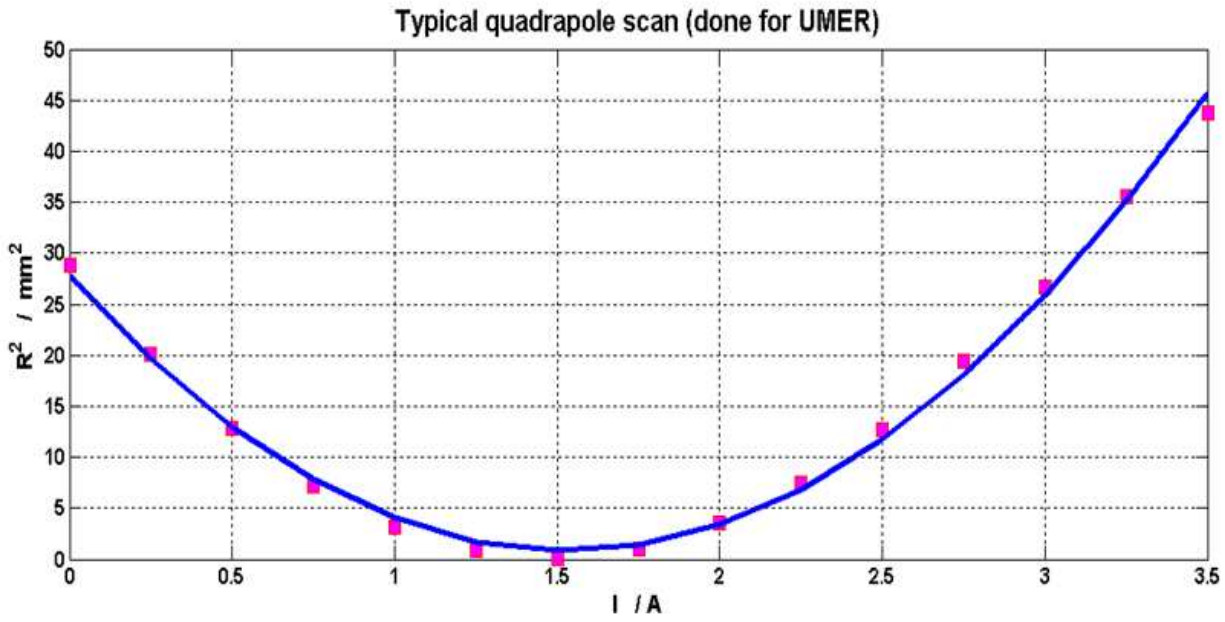

Figure 3.7: Typical scanned size data measured for UMER. The beam size $\tilde{x}^2$ is plotted versus the quadrupole focusing strength and a quadratic (shown in red) is fitted to the actual data (black dots).

3.2.2 Pepper pot Based Emittance Measurement

In pepper pot technique, the phase space distribution and consequently the beam emittance can be measured by using apertures to sample smaller regions in transverse space. The beam is intercepted at pepper pot plate, which is normal to the beam and contains a regular array of identical holes over its entire surface. A diagram of the pepper pot experiment is shown in figure 3.8. Each subsection of the beam passing through a hole is known as beamlet. A downstream screen measures the location and intensity of each beamlet. The holes are small enough so that the beams passing through become emittance dominated. Therefore, the beam drifts along a straight line between the pepper pot and the screen. Knowing the position of the beamlets at mask, x_{Sj} , and screen, x_j and the distance between them, L, the divergence angle x' can be calculated as:

$$x' = \frac{x_j - x_{sj}}{L} \tag{3.5}$$

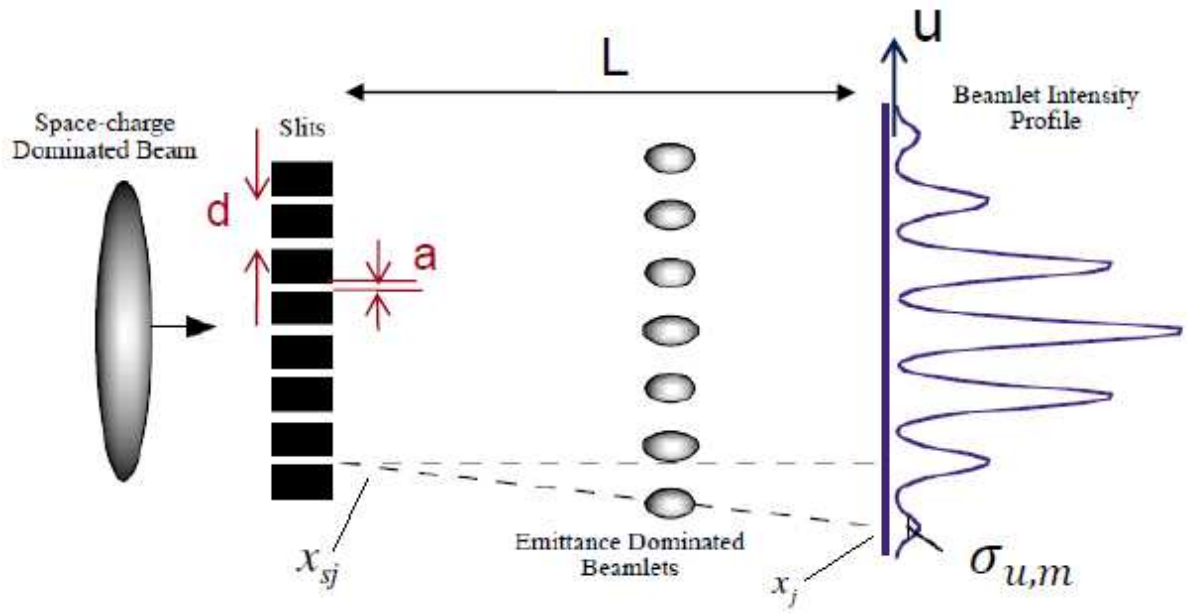

Figure 3.8: Layout of the pepper-pot experiment [41].

Although pepper pots are commonly used in the accelerator community, there are several major drawbacks in using them. In order to get a good resolution of the reconstructed phase space, a sufficient number of beamlets should be produced. Therefore, when the beam size is small, very small and closely spaced holes are necessary. In this regime, construction of such mask would pose serious practical difficulties. Additionally, when the holes are very close, the images of the beamlets may overlap increasing the error in the measurement. Finally, being an intercepting diagnostic, the hole reduces the beam intensity and therefore it make the detection of faint beamlets more difficult.

3.3 Beam Centroid Motion Characterization

3.3.1 Trajectory and Closed Orbit

The coordinate system for studying beam dynamics is shown in figure 3.9.

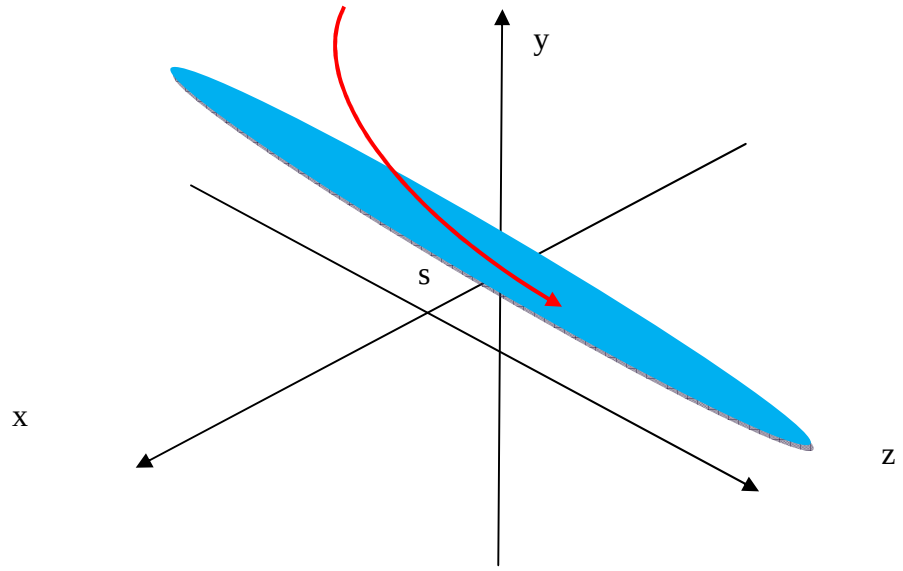

Figure 3.9: Coordinates of beam dynamics, where *x* and *y* define the transverse direction, *z* defines the longitudinal direction, and *s* is the actual direction where beam travels.

Assuming the transverse beam distribution $f(x, x', y, y')$ the centroid $< x >$ is defined as follows:

$$< x >= \frac{1}{N} \int \int \int \int x f(x, x', y, y') dx dx' dy dy' \tag{3.6}$$

and similarly the y centroid is defined.

The two dimensional transverse motion in x and y planes are described by the following differential equations [42]:

$$\begin{cases} x'' + (\kappa + \frac{1}{\rho^2}).x = \frac{\Delta B_y}{B\rho} \\ y'' - \kappa.y = \frac{\Delta B_x}{B\rho} \end{cases} \tag{3.7}$$

Where $\frac{\Delta B_x}{B\rho}$, $\frac{\Delta B_y}{B\rho}$ are the normalized magnetic field imperfections due to the dipole field errors. ρ is the radius of the ring, and B is the dipole field for bending the beam with radius ρ. There are two solutions for these equations; the homogenous (no field error) and the particular solution. The homogenous part gives rise to betatron oscillations of the particles described in details by:

$$\begin{cases} x_\beta(s) = \sqrt{\tilde{\epsilon}\beta(s)}\cos\left(\nu \cdot \varphi(s) + \varphi_{x0}\right) \\ y_\beta(s) = \sqrt{\tilde{\epsilon}\beta(s)}\cos\left(\nu \cdot \varphi(s) + \varphi_{y0}\right) \end{cases} \tag{3.8}$$

Where $\beta(s)$ is the beta function, $\varphi(s)$ is the betatron phase and φ_{x0} & φ_{y0} are the initial phases right after the beam injection into the ring [31].

The particular solution takes into account the field errors and generates the "Closed Orbit" (CO). For just one dipole error the horizontal closed orbit is described by [43]:

$$x_{co-i}(s) = \frac{\sqrt{\beta(s)\cdot\beta_i}}{2\sin(\pi\cdot\nu)} \cdot cos(\nu \cdot |\varphi(s) - \varphi_i| - \pi \cdot \nu) \tag{3.9}$$

and similarly for y closed orbit. The index i denotes the i-th dipole or corrector, and β_i & φ_i are measured inside this dipole. The error in dipole i generates the kick: $\theta_i = \frac{\Delta B_i l}{B\rho}$ where l is the effective length of the dipole. In fact, this kick generates the closed orbit. The full closed orbit is superposition of all N_D (number of dipoles) kicks around the ring and can be written as:

$$x_{co}(s) = \sum_{i=1}^{N_D} x_{co-i}(s) \tag{3.10}$$

The total solution for motion equations can then be obtained as:

$$x(s) = x_\beta(s) + x_{co}(s) \tag{3.11}$$

It can be noticed that x_{co} is DC part of the full solution. In the other words, closed orbit describes the average value of betatron oscillations at each location. This is why CO is sometimes called the "Equilibrium Orbit".

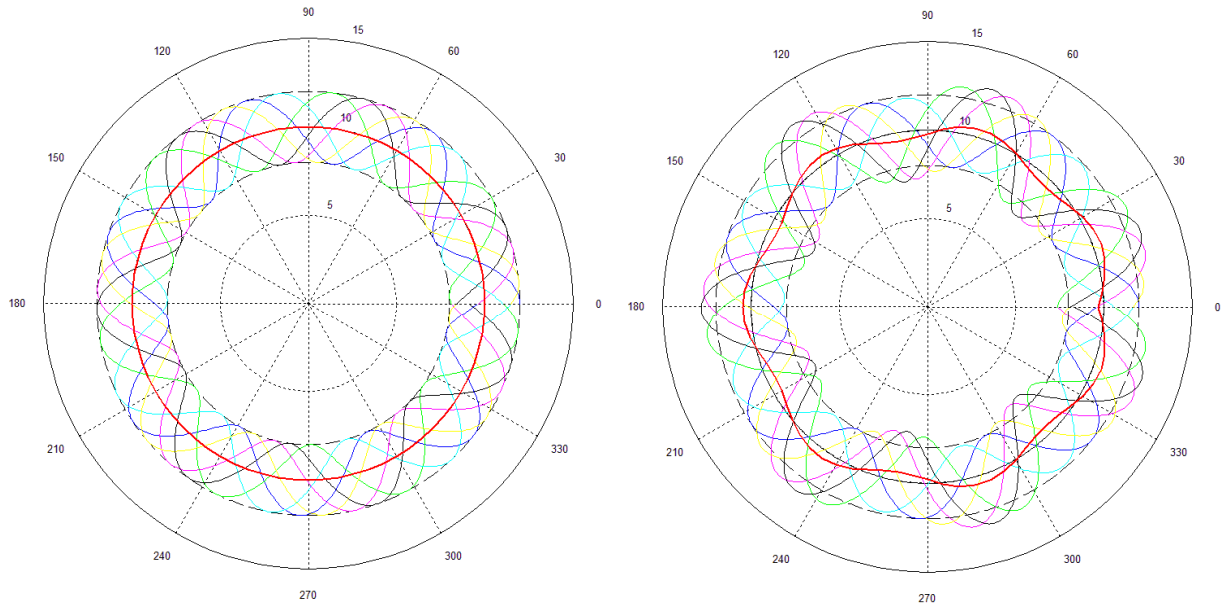

Figure 3.10: Left plot shows a hypothetical ring without any perturbation. Red curve is the reference orbit. The right plot shows a distorted closed orbit with perturbation $\theta = 30^{\circ}$ introduced (in the dipole) located at the angle 0. Non-red curves show betatron oscillations up to turn 6.

If there is no perturbation anywhere in the ring then the closed orbit reduces to the so-called "Reference Orbit" (RO) or "design orbit". Obviously:

$$\begin{cases} x_{RO}(s) = 0 \\ y_{RO}(s) = 0 \end{cases}$$

i.e. there is no DC part and the beam moves right along the center of the pipe. Therefore, the task of steering optimization can simply be described as making CO as similar as possible to RO. Figure 2.3 shows both the CO and the RO for a hypothetical ring with a $\theta = 30^{\circ}$ perturbation applied at the angle 0. Usually the CO is only known inside the Beam Position Monitors (BPMs) and the steering makes the quantized CO similar to quantized RO. As far as sampling the CO is carried out by a relatively high frequency (4-6 BPMs per betatron period) correcting sampled CO makes the whole CO close to RO.

3.4 Introduction to UMER

UMER, standing for University of Maryland Electron Ring [13], is a low energy high current circular accelerator intended for the study of beam physics from emittance to space charge dominated beams. The beam current in UMER can be varied from 0.6 mA to 100 mA, which covers a wide range of space charge levels. Figure 2.1 shows a schematic of UMER layout, and Table 2.1 lists its key parameters.

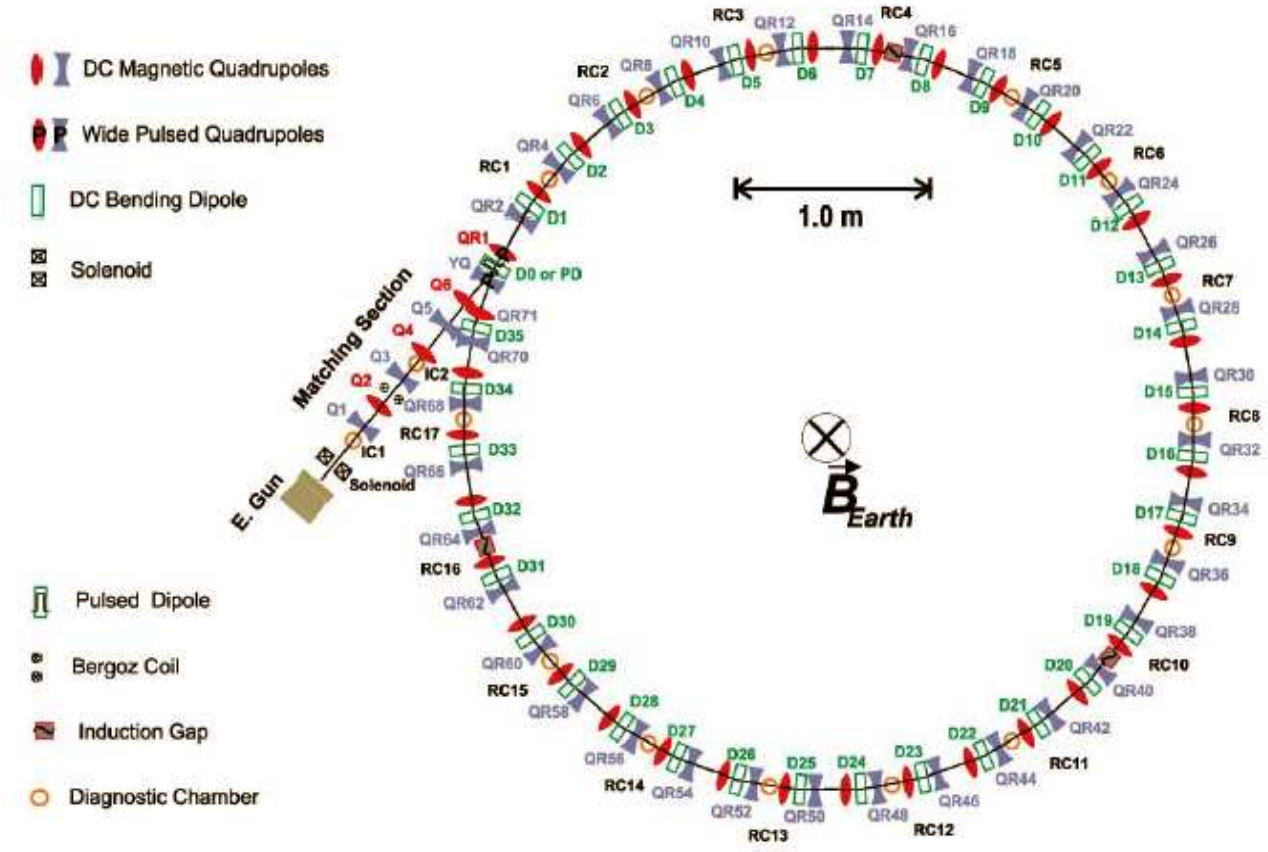

Figure 3.11: Schematic layout of UMER.

Table 3.1: UMER design parameters.

Beam Energy	**10 KeV**
$\beta = v / c$	0.2
Pulse Length	20-120 ns
Current	0.5-100 mA
Ring Circumference	11.52 m
Lap Time	197 ns
Pulse Repetition Rate	60 Hz
FODO period	0.32 m
Beam size at the aperture (100 mA)	3.2 mm
Beam size at the aperture (0.6 mA)	0.25 mm

UMER has three parts: injection, ring, and recirculation. As shown in figure 2.1, the electron beam is first generated at the E-Gun, and then introduced into the ring through the matching section. After that, the beam recirculates in the ring with the help of dipoles.

A key feature of UMER is the ability to vary the beam intensity. The related intensity parameter, χ, can be varied from 0.2 (emittance dominated beam) to 0.99 (space charge dominated beam). The beam intensity is varied by using different apertures to change the beam current. The variable beam intensity allows the study of steering schemes for various beams. Table 2.2 shows a list of aperture size, current, emittance and intensity parameters.

Table 3.2: Beam configurations in UMER.

Aperture#	$r0\ (mm)$	**I (mA)**	$\varepsilon\ (\mu m)$	χ
1	0.25	0.6	7.6	0.27
2	0.875	6	25.5	0.6
3	1.5	21	39.0	0.72
4	2.85	80	86.6	0.84
5	3.2	100	97.3	0.90

3.4.1 Earth's Magnetic Field Perturbations on Vertical Orbits

As the beam energy in UMER is low, the beam orbit is so sensitive to field perturbations caused by Earth's magnetic field. The Earth's field, which contributes around 20% of the bending force for beam steering, is not constant around the ring. The amplitude and the direction of the Earth's magnetic field vary along the ring as shown in the figure 3.11 [44-45]. In this figure, at every 10 degrees, there is a horizontal dipole. The perturbations affect vertical steering more severely, since the horizontal components of the Earth's field tangent to the ring is responsible for the deflections. Such tangential components follow approximately a sine curve, and therefore vertical plane perturbations are modulated by a sinusoid.

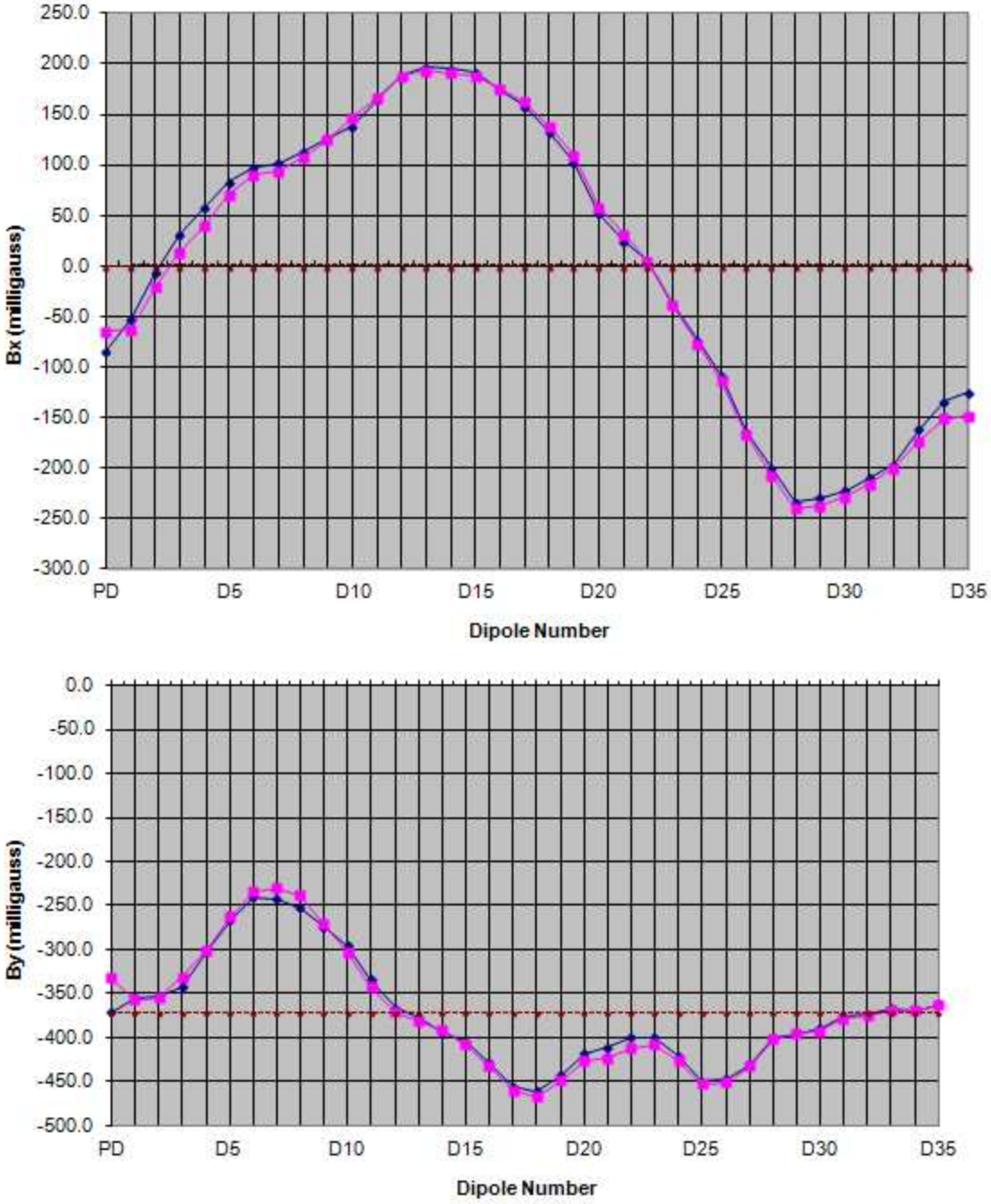

Figure 3.12: Measured Earth's magnetic field around the UMER ring. The top graph shows the Horizontal component while the bottom graph shows the vertical component. The Horizontal part of Earth's field is responsible for vertical perturbation [44].

3.5 Introduction to Advanced Wakefield Accelerator (AWA)

As most of the simulations for emittance measurement method discussed in chapter 5 are done for AWA, this section provides a brief introduction about this accelerator machine. AWA, standing for Advanced Wakefield Accelerator and located at ANL [46], is a medium energy LINAC with beam energy from 8 MeV up to 100 MeV. Figure 3.13 shows a schematic of AWA beam line. The length of the accelerator is close to 9 m. It has a RF gun which injects electron beam bunches of about 1 MeV energy and length 8 ps into the LINAC section. The charge of the bunch is normally 1 nC, however, it can be increased to around 10 nC by using a wider laser spot size. For the beam charge of 1 nC, the peak beam current is 125 A. There are 4 YAG diagnostics points on the beam line which provide beam intensity profile measurements. The AWA beam is round all along the lattice. The space after $z = 7\,m$ is available for quadrupole scan experiment. As the layout shows, the scanning lens which can be either of a quadrupole or a solenoid is located at $z = 7\,m$ and the OTR foils are placed half a meter away at $z = 7.5\,m$. Table 3.3 lists key parameters of the AWA.

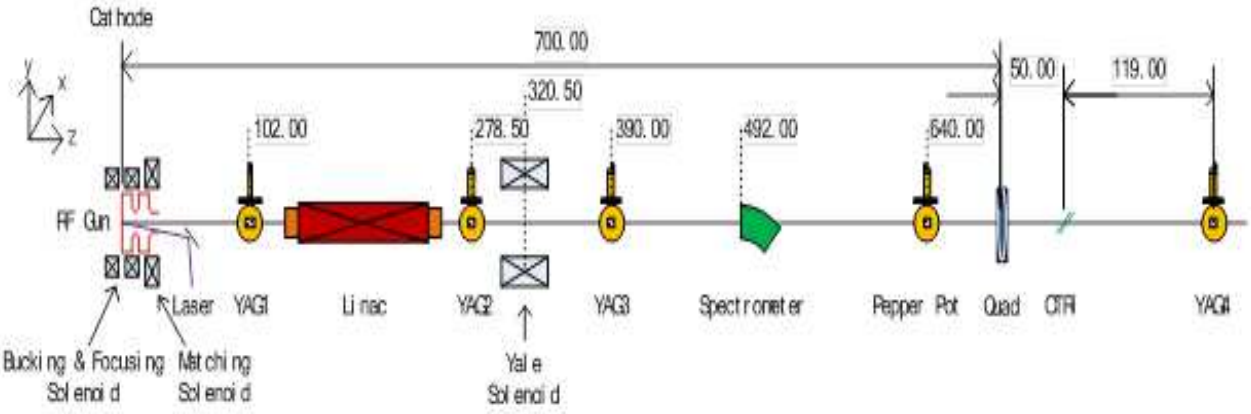

Figure 3.13: Schematic diagram of AWA beam line [47].

Table 3.3: Beam parameters in AWA [47].

Parameters	**Value**	**Unit**	**Comment**
R_laser	1	mm	Laser spot radius
Charge	1	nC	
FWHM	8	ps	Gaussian
Phi_Gun	50	deg	8 MeV after gun
Phi_Linac	90	deg	14 MeV after LINAC
I_BF	550	A	
I_M	320	A	
I_Yale	70	A	

Chapter 4: Measuring Emittance for Space Charge Dominated Beams

In this chapter, we present our first method for measuring emittance of beams with space charge, which is based on determining emittance from two measurements of beam size and divergence. First, in section 4.1, we review a method for determining the cross-correlation term from the scan of beam size. Then, in section 4.2, we present a closed-form solution for cross-correlation term from two measurements of the size and divergence. In first two sections, it is presumed that the beam is emittance dominated. In section 4.3, based on KV envelope equations, we present an iterative procedure for finding cross-correlation of a beam with space charge again with two pairs of size and divergence measurements [48-49].

In section 4.4, we, first, present the results of applying our method to simulated beams and then we discuss its noise analysis and numerical stability.

4.1 Determining the Cross-correlation Term From Beam Size Scans

In [15] it was shown that for an emittance dominated beam, the cross-correlation term can be determined at the minimum of a quadrupole scan of the beam radius or divergence as a function of focusing strength. Here, we follow a different approach to derive a relation for the cross-correlation term that can be easily extended to beams with space charge.

Figure 4.1 shows a typical quadrupole scan setup. The focal length of the quadrupole (or solenoid) is varied (scanned) to achieve a minimum spot size on the screen located downstream at a distance L from the quadrupole. Assuming no space charge, the *rms* transverse beam envelope in the drift region can be expressed as:

$$R(s) = \left({R_0}^2 + 2 \cdot R_0 \cdot {R'}_0 \cdot s + \left(\frac{\epsilon^2}{{R_0}^2} + {{R'}_0}^2 \right) \cdot s^2 \right)^{\frac{1}{2}} \tag{4.1}$$

where R_0 and R'_0 denote the initial 2×rms radius and slope of the envelope at the lens, ϵ is the effective emittance, and s is the distance from the lens on the axis along the beam direction. Here, the radius R stands for either of the two transverse radii, and we do not assume the beam is axissymmetric. Then for beam radius at the location of screen we have:

$$R(L) = \left({R_0}^2 + 2 \cdot R_0 \cdot {R'}_0 \cdot L + \left(\frac{\epsilon^2}{{R_0}^2} + {R'_0}^2 \right) \cdot L^2 \right)^{\frac{1}{2}} \tag{4.2}$$

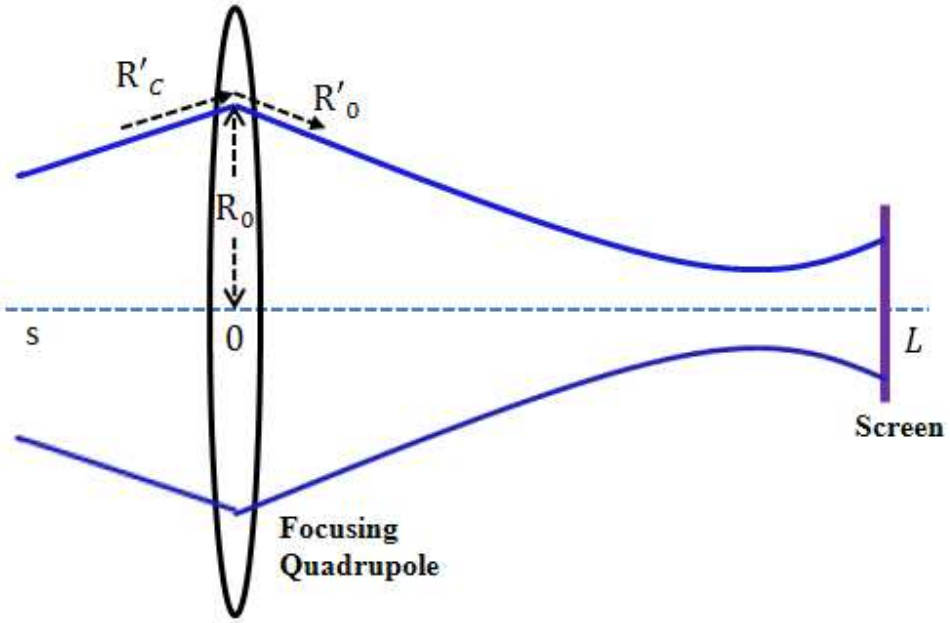

Figure 4.1: Diagram of a quadrupole scan setup to measure emittance. Beam enters the quadrupole with envelope R_0 and slope R'_C and leaves it with slope R'_0.

The focal length required to have minimum beam radius on screen, f_m, can be found by setting the derivative of $R(L)$ with respect to f equal to 0. According to Eq. (A3) in the Appendix, a variation in f simply translates to a variation in beam slope right after the lens, R'_0. When we take the derivative of R with respect to R'_0. The solution is:

$$R'_0|_{f=f_m} = -\frac{R_0}{L} \tag{4.3}$$

By plugging Eq. (4.3) into Eq. (4.1) we obtain the minimum beam radius at the screen:

$$R_{min}(L) = \frac{\epsilon \cdot L}{R_0} \tag{4.4}$$

To find the cross-correlation term we also need to calculate $R_m{}'(L)$, the slope of the envelope at the screen when the radius is minimum. Note that this is non-zero since the minimum radius does not correspond to a waist, which is defined as the value of R when $dR/ds = 0$; whereas the minimum radius in a quad scan occurs when $dR/df = 0$. Taking the derivative of $R(s)$ given in Eq. (4.1) with respect to s and evaluating it at $s = L$ we obtain:

$$R'(L) = \frac{R_0 \cdot R'_0 + \left(\frac{\epsilon^2}{R_0{}^2} + R'_0{}^2\right) \cdot L}{R(L)} \tag{4.5}$$

By substituting R'_0 and $R(L)$ from Eqs. (4.3) and (4.4) we get:

$$R'_m(L) = \frac{R_{min}(L)}{L} \tag{4.6}$$

$R'(L)$, alternatively, can be expressed as:

$$R'(L) = 2\frac{d\sqrt{< r_L^2 >}}{ds} = 2\frac{< r_L \cdot r'_L >}{\sqrt{< r_L^2 >}} = 4\frac{< r_L \cdot r'_L >}{R(L)} \tag{4.7}$$

Where r_L and r'_L denote the trace space x or y position and velocity of the particles at the screen. In case x, applying Eq. (4.7) to beam screen values at minimum radius and combining it with Eq. (4.6) leads to:

$$< x_L \cdot x'_L >= \frac{< x_L^2 >}{L} \tag{4.8}$$

Thus, the cross-correlation term can be determined from a single value of the beam size, i.e. its minimum measured value, and the x rms emittance can be written in terms of the measured rms beam radius, $\sqrt{< x_L^2 >}$, and rms beam divergence, $\sqrt{< \acute{x}_L^2 >}$ as:

$$\tilde{\epsilon}_x^2 =< x_L^2 > \left(< x'^2_L > - \frac{< x_L^2 >}{L^2}\right) \tag{4.9}$$

Likewise, $\tilde{\epsilon}_y^2$ can be computed from vertical (y) measurements. These expressions match those given in [15], which are obtained with a different method.

In summary, the envelope is measured over a range of quadrupole focusing strengths. Then, after fitting a quadratic to the data, f_m and the rms radius at the quad scan minimum are inferred from the curve. With the additional measurement of the rms divergence at f_m, the emittance is calculated from Eq. (4.9). Since we are dealing with an emittance dominated beam here, the advantage of this approach, in comparison to conventional quadrupole scan fitting, is that only one pair of simultaneously measured observables (size and divergence) are required to provide the emittance, whereas in a normal Courant Snyder quadratic fit at least three values of the beam size are necessary . However, as we will show the approach outlined above can be readily extended to provide a method to determine the emittance of a space charge dominated beam by using two pairs of values of the divergence and beam size measured along the quad scan, i.e. without requiring that they include the minimum value of any of these parameters.

4.2 Emittance from two samples of size and divergence

In this section, we present a method to determine the rms emittance from the rms radius and divergence measured for two arbitrary settings of the quadrupole focusing strength.

We assume that the following two sets of rms beam radii and divergences have been measured at two distinct focal lengths f_1 and f_2:

$$\begin{cases} f_1 \\ < x_1^2 > \\ < x_1'^2 > \end{cases} \quad , \quad \begin{cases} f_2 \\ < x_2^2 > \\ < x_2'^2 > \end{cases}$$

From these measurements, we can infer the cross-correlation terms, XC_i $(i = 1,2)$.

To see this first note that $\tilde{\epsilon}^2$ can be written in terms of beam parameters at each of the focal settings as:

$$\tilde{\epsilon}^2 = < x_i^2 >< x'^2_i > - XC_i{}^2 \ \ (i = 1,2) \tag{4.10}$$

This leads to:

$$XC_2{}^2 = XC_1{}^2 \ + \ A \tag{4.11}$$

Where A is defined as:

$$A \equiv < x_2^2 >< x'^2_2 > - < x_1^2 >< x'^2_1 > \tag{4.12}$$

We now find a second relation between the two cross-correlation terms. To do so, we need to express R_0, the initial beam radius, in terms of beam parameters at the screen. We note that if the beam starts with radius $R(L)$ and slope $-R'(L)$ at screen and propagates back toward the lens, then it obtains the radius R_0 and slope R'_0 after traversing the drift distance L. In other words, to derive R_0, we can switch R_0 and $R(L)$, and replace R'_0 with $-R'(L)$ in Eq. (4.2) to obtain:

$$R_0{}^2 = R(L)^2 - 2 \cdot R(L) \cdot R'(L) \cdot L + \left(\frac{16\tilde{\epsilon}^2}{R(L)^2} + R'(L)^2 \right) \cdot L^2 \tag{4.13}$$

By substituting the expression for $R'(L)$ given in Eq. (4.7) and simplifying, we obtain R_0 in terms of rms beam size and divergence as:

$$R_0{}^2 = 4(< x_i^2 > -2 \cdot XC_i \cdot L + < x'^2_i > \cdot L^2) \tag{4.14}$$

Likewise, we can express R'_0 in terms of beam parameters at the lens by switching R_0 and $R(L)$, and replacing R'_0 with $-R'(L)$ in Eq. (4.5) to get:

$$R'_{0i} = -4 \frac{< x'^2_i > \cdot L - XC_i}{R_0} \tag{4.15}$$

Using Eq. $(A3)$ from the appendix, we can express f_i, the focal length of the lens as:

$$\frac{1}{f_i} = \frac{R'_C - R'_{0i}}{R_0} = \frac{R'_C \cdot R_0 + 4 < x'^2_i > \cdot L - 4XC_i}{R_0{}^2} \tag{4.16}$$

Subtracting the two equations of (4.16) and substituting for ${R_0}^2$ using Eq. (4.14) for $i = 1$ (i.e. measurement set 1), we obtain following relation between two cross-correlation terms:

$$XC_2 = B \cdot XC_1 + C \tag{4.17}$$

With B and C defined as:

$$\begin{cases} B \equiv 1 - 2L\left(\frac{1}{f_1} - \frac{1}{f_2}\right) \\ C \equiv \left(< x_1^2 > + < {x'}_1^2 > \cdot L^2\right)\left(\frac{1}{f_1} - \frac{1}{f_2}\right) - \left(< {x'}_1^2 > - < {x'}_2^2 >\right) \cdot L \end{cases} \tag{4.18}$$

Combining equations (4.11) and (4.17) we get following quadratic equation for XC_1:

$$(B^2 - 1) \cdot {XC_1}^2 + 2 \cdot B \cdot C \cdot XC_1 + C^2 - A = 0 \tag{4.19}$$

Therefore XC_1 is given by :

$$XC_1 = \frac{-B \cdot C \pm \sqrt{A \cdot B^2 + C^2 - A}}{B^2 - 1} \quad , B \neq \pm 1 \tag{4.20}$$

By plugging XC_1 into Eq. (4.10), rms emittance can be calculated.

It should be pointed out that cancelling ${R'}_C$ is the main reason for needing two pairs of measurements instead of just one. We could also form a second equation between cross-correlations by using Eqs. (4.14), i.e. by matching the R_0 for two focal settings. For a thin lens, we should get the same answer whether we constrain the R_0 or the focal lengths f_1 and f_2 as we did above. However, for a real, thick lens, R_0 varies when the focusing strength of the lens changes. Therefore, a more accurate result is gained by constraining the focal lengths through Eqs. (4.16).

The method described here relies on two pairs of beam size and divergence samples to solve for cross-correlation term and consequently the emittance, while the common Courant-Snyder parameter fitting technique requires at least three samples of beam size (or divergence) [2]. Obviously, however, we can use multiple pairs to improve the statistical accuracy of the

measurement. Moreover, in comparison to the approach described above, we do not require that the quadrapole scan curve go through a minimum. This can be a valuable advantage considering the fact that practically, the minimum may not be approachable.

We now extend the approach we have followed in this section to the universal case when space charge is not negligible.

4.3 Measuring Emittance of a Beam with Space Charge

For a uniform beam distribution where space charge is linear, the beam envelope evolution in a drift region is described by the following pair of coupled, second order, nonlinear, ordinary differential equations (ODE):

$$R_j''(s) - \frac{2K}{R_x(s) + R_y(s)} - \frac{\epsilon_j^2}{R_j(s)^3} = 0 \tag{4.21}$$

Where j ranges over transverse coordinates x and y, and dimensionless quantity

$$K = \frac{qI_b}{2\pi\epsilon_0 m(c\beta\gamma)^3} \tag{4.22}$$

is defined as the generalized perveance, which represents the effect of space charge defocusing forces. In Eq. (4.22), q is charge of the beam particles and I_b is the beam peak current. Equations (4.21), also known as Kapchinskij-Vladimirskij (KV) envelope equations, are consistent with the KV phase space distribution which is an equilibrium solution of the Vlasov equation [50]. Due to the nonlinearity of the envelope equations in this case, a closed-form solution similar to Eq. (4.1) cannot be given However, we will show that these Equations can be solved using an iterative numerical approach.

As before, we use a lens-drift-screen setup; however, due to the coupled nature of Eq. (4.21) we consider the separate cases based on beam cross-section right before the lens and the type of

lens: 1) a round beam with symmetric focusing lens; 2) an elliptical beam with either lens type; and 3) a round beam with an asymmetric focusing lens. In the following sections, we discuss each case.

4.3.1 Round beam with symmetric focusing lens

If a round beam ($R_x = R_y = R$) enters a symmetric focusing lens such as a solenoid, then the beam maintains its roundness throughout the drift section and therefore we get two independent equations for both R_x and R_y:

$$R_j''(s) - \frac{K}{R_j(s)} - \frac{\epsilon_j^2}{R_j(s)^3} = 0 \tag{4.23}$$

Later in this section, we will present our scheme for solving these equations.

As R_x and R_y are equal in this case, we drop the index j and treat all parameters for x. Multiplying Eq. (4.23) by R' and then integrating with respect to s leads to the following first order ODE:

$$R'(s) = \pm\left[{R_0}'^2 + \epsilon^2 \cdot \left(\frac{1}{{R_0}^2} - \frac{1}{R(s)^2}\right) + 2K \cdot \ln\left(\frac{R(s)}{R_0}\right)\right]^{1/2} \tag{4.24}$$

where R_0 and ${R_0}'$, again, denote the radius and slope of the envelope at the lens. Similar to the zero space charge case, we need to have the beam envelope relation in terms of at-screen radius and slope quantities. This can be done simply by switching R_0 and ${R_0}'$ with beam quantities at the screen, $R(L)$ and $-R(L)'$, and applying a minus to the LHS of Eq. (4.24). Such minuses are necessary as we are treating the envelope evolution along $-s$. Thus, envelope ODE in terms of envelope parameters at screen can be expressed as:

$$R'(s) = \mp\left[R(L)'^2 + \epsilon^2 \cdot \left(\frac{1}{R(L)^2} - \frac{1}{R(s)^2}\right) + 2K \cdot \ln\left(\frac{R(s)}{R(L)}\right)\right]^{1/2} \tag{4.25}$$

This form of envelope ODE can easily be solved by numerical integration in packages like MATLAB [34].

As there is no closed form solution to this equation for large K, we cannot provide a closed form answer for emittance. Based on the analysis of previous section for negligible space charge case, the following procedure is devised to determine the emittance.

We start with a guess for cross-correlation term and try to infer focal setting applied to the lens by solving Eq. (4.25). Beam radius and divergence measurements at the screen are translated to $R(L)$ and $R(L)'$ and therefore inferred focal length is going to be a function of the guessed cross-correlation. We use the error between calculated focal length with actual focal length to correct our guess for cross-correlation and reiterate the procedure. Finally, after several steps, as the inferred focal length converge toward the actual one we come within a close vicinity of the actual cross-correlation.

4.3.1.1 Numerical Procedure

The detailed steps of the procedure are described here. As before we need two sets of beam radius and divergence measurements at two distinct focal lengths f_1 and f_2:

$$\begin{cases} f_1 \\ < x_1^2 > \\ < x_1'^2 > \end{cases} \quad , \quad \begin{cases} f_2 \\ < x_2^2 > \\ < x_2'^2 > \end{cases}$$

Henceforth, we use subscript n, denoting the step number, alone or besides the measurement numbers 1 or 2 on all parameters that change over subsequent steps.

1. $XC1_1$, initial guess for the cross-correlation term at f_1, is chosen according to the discussion in next section.

2. Using Eq. (4.11), $XC2_n$, the cross-correlation term at f_2, is calculated as:

$$XC2_n = \pm\sqrt{{XC1_n}^2 + A} \tag{4.26}$$

3. Next, ϵ_n (not to be confused with normalized emittance) and ${R'}_i(L)$ for two measurement sets ($i = 1,2$) are calculated as:

$$\begin{cases} \epsilon_n = 4[< x_1^2 > \cdot < {x'}_1^2 > - {XC1_n}^2]^{1/2} \\ {R'}_1(L)_n = 2\dfrac{XC1_n}{\sqrt{< x_1^2 >}} \\ {R'}_2(L)_n = 2\dfrac{XC2_n}{\sqrt{< x_2^2 >}} \end{cases} \tag{4.27}$$

Note that all three relations are in term of $XC1_n$.

4. ODE Eq. (4.25) can now be solved for finding at-lens envelope radius and slope conditions of measurements 1 and 2:

$$\begin{cases} R(0)_{1n} \quad , \quad R'(0)_{1n} \\ R(0)_{2n} \quad , \quad R'(0)_{2n} \end{cases}$$

5. According to Eq. (A3), for f_{1n} and f_{2n} estimates of focal lengths we have:

$$\begin{cases} f_{1n} = \dfrac{R(0)_{1n}}{{R'}_C - R'(0)_{1n}} \\ f_{2n} = \dfrac{R(0)_{2n}}{{R'}_C - R'(0)_{2n}} \end{cases} \tag{4.28}$$

Canceling the unknown ${R'}_C$ between these two equations and replacing f_{2n} with its final value f_2 leads to:

$$f_{1n} = \frac{f_2 \cdot R(0)_{1n}}{R(0)_{2n} + f_2 \cdot (R'(0)_{2n} - R'(0)_{1n})} \tag{4.29}$$

This equation is used to update f_{1n} at each step n. As before, the necessity for two pair of measurements arises from ${R'}_C$.

6. It can be easily checked that f_{1n} is a function of $XC1_n$. i.e. $f_{1n} = g(XC1_n)$. $XC1_n$ should be modified so that reiteration of the procedure from entry 2 makes f_{1n} closer to the target value f_1. In other words, $XC1_n$ is zero of this equation:

$$g(XC1_n) - f_1 = 0 \tag{4.30}$$

Since derivative of the function g is not known, a modified form of Newton method [35] was used to find $XC1_n$ as zero of this equation. In first step ($n = 1$), $XC1_2$ is valued in the vicinity of XC_1:

$$XC1_2 = 0.95\, XC1_1 \tag{4.31}$$

We may need to pick $XC1_2$ closer to $XC1_1$ if $XC1_2$ makes the RHS of Eq. (4.26) imaginary. After the first step ($n \geq 2$), $XC1_n$ is updated according to:

$$XC1_{n+1} = XC1_n - \frac{XC1_n - XC1_{n-1}}{g(XC1_n) - g(XC1_{n-1})} \cdot (g(XC1_n) - f_1) \tag{4.32}$$

Interval halving is another numerical root finder method that can be used to update $XC1_n$. After updating $XC1_n$ either way, the procedure is repeated from entry 2 until f_{1n} converges with desired precision toward f_1. The process can also be stopped when the variation on emittance calculated at two consecutive steps is less than some δ% of the calculated emittance, where delta is usually chosen between 1 and 10. Finally, beam effective emittance is the last ϵ_n calculated in entry 3.

4.3.1.2 Choosing an Initial Value For $XC1$

Generally, choosing appropriate initial value is important for converging problems. Initial value for $XC1$ should satisfy two constraints: ${\epsilon_1}^2 > 0$ and ${XC2_1}^2 > 0$ i.e. both quantities are real. The first condition sets a hard minimum for absolute value of $XC1$, while the second one

specifies a soft upper bound if $A < 0$. There will be no upper limit when $A \geq 0$. According to relations (4.26) and (4.27) for $XC2_n$ and ϵ_n we have:

$$\begin{cases} |XC1_1| < \sqrt{< x_1^2 >< x'^2_1 >} \\ |XC1_1| \gtrsim \sqrt{-A} \qquad if\ A < 0 \end{cases} \tag{4.33}$$

We define interval R_{XC} as the distance between the two bounds:

$$R_{XC} \equiv \sqrt{< x_1^2 >< x'^2_1 >} - \sqrt{-A} \quad if\ A < 0 \tag{4.34a}$$

And:

$$R_{XC} \equiv \sqrt{< x_1^2 >< x'^2_1 >} \qquad if\ A \geq 0 \tag{4.34b}$$

$XC1_1$ is chosen to be at the middle of this interval:

$$XC1_1 = S_1 \cdot \begin{cases} \sqrt{-A} + \frac{R_{XC}}{2} & if\ A < 0 \\ \frac{R_{XC}}{2} & if\ A \geq 0 \end{cases} \tag{4.35}$$

Where S_1 getting values from $\{-1, +1\}$ determines the sign of $XC1_1$. Usually, sign of $XC1_1$ is known beforehand, however, one may try the other case if the first choice of sign leads to a divergent solution.

In interval halving method we need to determine the initial interval I_1 too. For the negative A, such interval can be chosen as:

$$I_1 = S_1 \cdot \left[\sqrt{-A} + 0.05 \cdot R_{XC} \qquad \sqrt{< x_1^2 >< x'^2_1 >} - 0.05 \cdot R_{XC} \right] \tag{4.36a}$$

And for positive A:

$$I_1 = S_1 \cdot \left[0.05 \cdot R_{XC} \qquad \sqrt{< x_1^2 >< x'^2_1 >} - 0.05 \cdot R_{XC} \right] \tag{4.36b}$$

4.3.2 Elliptical beam with either lens type

A quadrupole is the only example we can provide for an asymmetric focusing lens. For these cases Eq. (4.21) should be solved for both R_x and R_y. A quadrupole or an elliptical beam manifests as different initial conditions for differential Eq. (4.21) and therefore the beam hits the screen with different radius and divergence values for x and y. Measuring emittance in such cases will be discussed later.

If the beam before entering the lens is elliptical or the lens is a quadrupole then the evolution of the x and y envelopes can diverge. We extend the approach discussed for round beam to cover such beams.

First, similar to the round beam case discussed above, we multiply Eqs. (4.21) by $R_j{}'$ and then integrate with respect to s for j ranging over x and y. We receive following coupled first order ODE's in terms of beam values at $s = L$:

$$\begin{cases} R_x'(s) = \mp\left[R_x'(L)^2 + \epsilon^2 \cdot \left(\frac{1}{R_x(L)^2} - \frac{1}{R_x(s)^2}\right) + 4K \cdot \ln\left(\frac{R_x(s)+R_y(s)}{R_x(L)+R_y(s)}\right)\right]^{1/2} \\ R_y'(s) = \mp\left[R_y'(L)^2 + \epsilon^2 \cdot \left(\frac{1}{R_y(L)^2} - \frac{1}{R_y(s)^2}\right) + 4K \cdot \ln\left(\frac{R_y(s)+R_x(s)}{R_y(L)+R_x(s)}\right)\right]^{1/2} \end{cases} \tag{4.37}$$

where we have assumed that x and y emittances are about the same. Obviously, to solve these equations we need beam quantities in the y plane as well. Thus, two sets of beam radius and divergence measurements at two distinct focal lengths f_1 and f_2 are:

$$\begin{cases} f_1 \\ < x_1^2 >, < y_1^2 > \\ < x_1'^2 >, < y_1'^2 > \end{cases} \quad , \quad \begin{cases} f_2 \\ < x_2^2 >, < y_2^2 > \\ < x_2'^2 >, < y_2'^2 > \end{cases}$$

We can follow the same procedure as before, except than envelope slopes in y should be measured at entry 3 after calculating the emittance. To this end, we first calculate the cross-correlations in y for two measurements 1 and 2 according to:

$$\begin{cases} YC1_n = 4[{\epsilon_n}^2 - < y_1^2 > \cdot < {y'}_1^2 >]^{1/2} \\ YC2_n = 4[{\epsilon_n}^2 - < y_2^2 > \cdot < {y'}_2^2 >]^{1/2} \end{cases} \tag{4.38}$$

And then slopes can be calculated as:

$$\begin{cases} {R'}_{y1}(L)_n = 4\dfrac{YC1_n}{\sqrt{< y_1^2 >}} \\ {R'}_{y2}(L)_n = 4\dfrac{YC2_n}{\sqrt{< y_2^2 >}} \end{cases} \tag{4.39}$$

To numerically solve ODE's in (4.38), both equations are integrated simultaneously in entry 4 of the numerical procedure. It can easily be checked that by converging $XC1_n$ toward its actual value other three cross-correlation terms converge toward their actual values as well.

4.3.3 Round beam with an asymmetric focusing lens

This case is treated similar to the case elliptical beam with either lens type.

4.4 Simulation Results

In this section, we validate our emittance measurement approach by simulating the lens-drift-screen experiment using the self-consistent electrostatic particle-in-cell code WARP [51-52]. In the simulations, WARP can include all the effects that simple envelope solver in MATLAB ignores. For instance, while the envelope solver presumes that the beam distribution is uniform and space charge forces are linear, WARP can simulate non-uniform distributions like a Gaussian with nonlinear space charge forces.

The code WARP has been successfully benchmarked against experimental data. The code simulates space charge effects in 2D or 3D by advancing particles in a transverse slice under the impact of external forces and self-consistent self-fields. The self-fields are calculated on a mesh of sufficient resolution to capture the beam potential variations and the particles are advanced

using the leap-frog algorithm. We used a 256×256 grid for the Poisson solver, a step size of 2 mm along z, and 500,000 particles. It was proved to us that with these values we could have accurate results as test simulations with more particles or higher resolution resulted in no perceptible difference in the final result.

Figure 4.2 shows the beam structure that was defined in WARP. As can be seen the lens has length 20 cm and it is located at z=20 cm. The drift length, L, is 40 cm. First, we used a uniform distribution for the simulated beam. Based on presumed beam parameters ϵ, K and an initial envelope radius at the edge of solenoid, WARP generates a set of beam radius and divergence rms values $< x^2 >$ and $< x'^2 >$ at end of the drift section where beam divergence and size are supposedly measured, e.g., using OTRI. The focal length of the lens, f, is calculated according to a hard edge model of the lens. The performance of the method for the several grades of the space charge was tested. First, a low space charge beam with following parameters:

$$\begin{cases} K = 8.82 \times 10^{-5}\,, \epsilon = 19.5\ \mu m \\ R_0 = 3\ mm\,, \qquad L = 200\ mm \end{cases}$$

was simulated with a solenoid. Two pairs of beam radius and divergence samples taken at focal lengths, $f_1 = 134\ mm$ and $f_2 = 232\ mm$ were:

$$\begin{cases} \sqrt{< x_1^2 >}^{f_1} = 3.5\ mm \\ \sqrt{< x'^2_1 >} = 1.3\ mrad \end{cases}, \qquad \begin{cases} \sqrt{< x_2^2 >}^{f_2} = 4.2\ mm \\ \sqrt{< x'^2_2 >} = 1.2\ mrad \end{cases}$$

These samples were fed into the procedure. Figure 4.3 shows convergence curves for emittance and also the focal lengths. As can be seen, the emittance converges to within 1% of its simulated value after just 5 iterations. Figures 4.4(a) and 4.4(b) show emittance convergence curves for space charge dominated beams with $K = 2.83 \times 10^{-4}$ and $K = 7.06 \times 10^{-4}$ respectively. Still, the convergence is fast and errors in calculation of emittance are satisfactory.

To study performance of the procedure for an elliptical beam, a quadrupole was used to generate the samples. Figure 4.5 shows the emittance convergence curve for such an asymmetric beam.

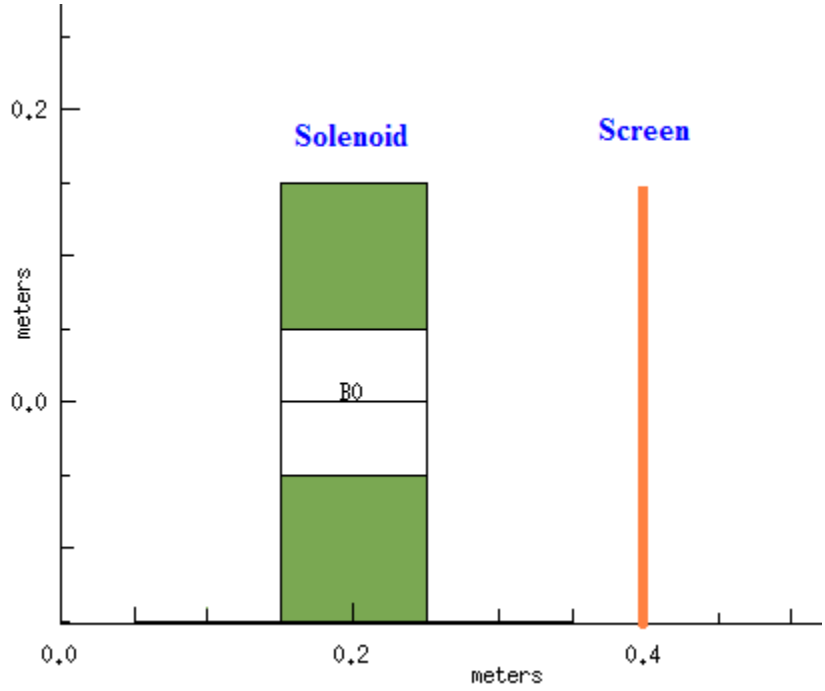

Figure 4.2: solenoid-drift-screen setup used in WARP.

To see effectiveness of the proposed procedure we have compared our results with the emittance measured by two other methods, i.e. the conventional Courant Snyder parameter fitting technique and the minimum beam size method calculated from Eq. 4.9. Figure 4.6(a) shows scan of beam radius done for a high space charge beam with $K = 7.06 \times 10^{-4}$. Note the poor quality of a quadratic fit to the data, represented by fairly low goodness-of-fit [53] value $R^2 = 0.95$, which is a sign that emittance measured by methods ignoring space charge are not reliable. In contrast, the quadratic fit ($R^2 = 0.99$) shown in Figure 4.6(b) for the emittance dominated beam is excellent. In Figure 4.7 we compare the emittance obtained with different methods as a function of the parameter K. As expected, the error in determining the emittance

obtained using the conventional Courant Snyder quadratic fitting technique and the minimum beam size methods, which are both accurate for emittance dominated beams, becomes increasing large as space charge increases. In contrast, our two points fit method gives acceptable values for the emittance for all values of the K parameter shown.

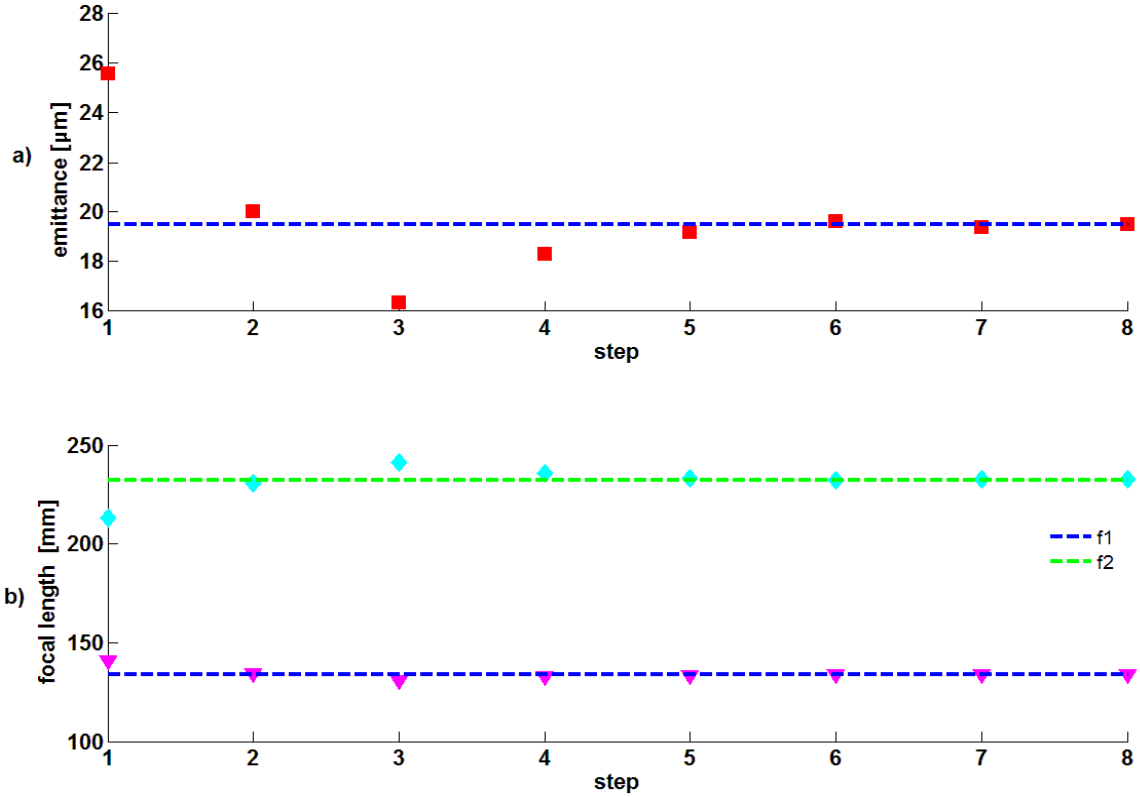

Figure 4.3: Plots show convergence of emittance (a) and focal lengths f_1 and f_2 (b) for a low space charge beam with $K = 8.82 \times 10^{-5}$. Dashed line in (a) indicates the actual emittance while squares indicate the calculated emittance at each step.

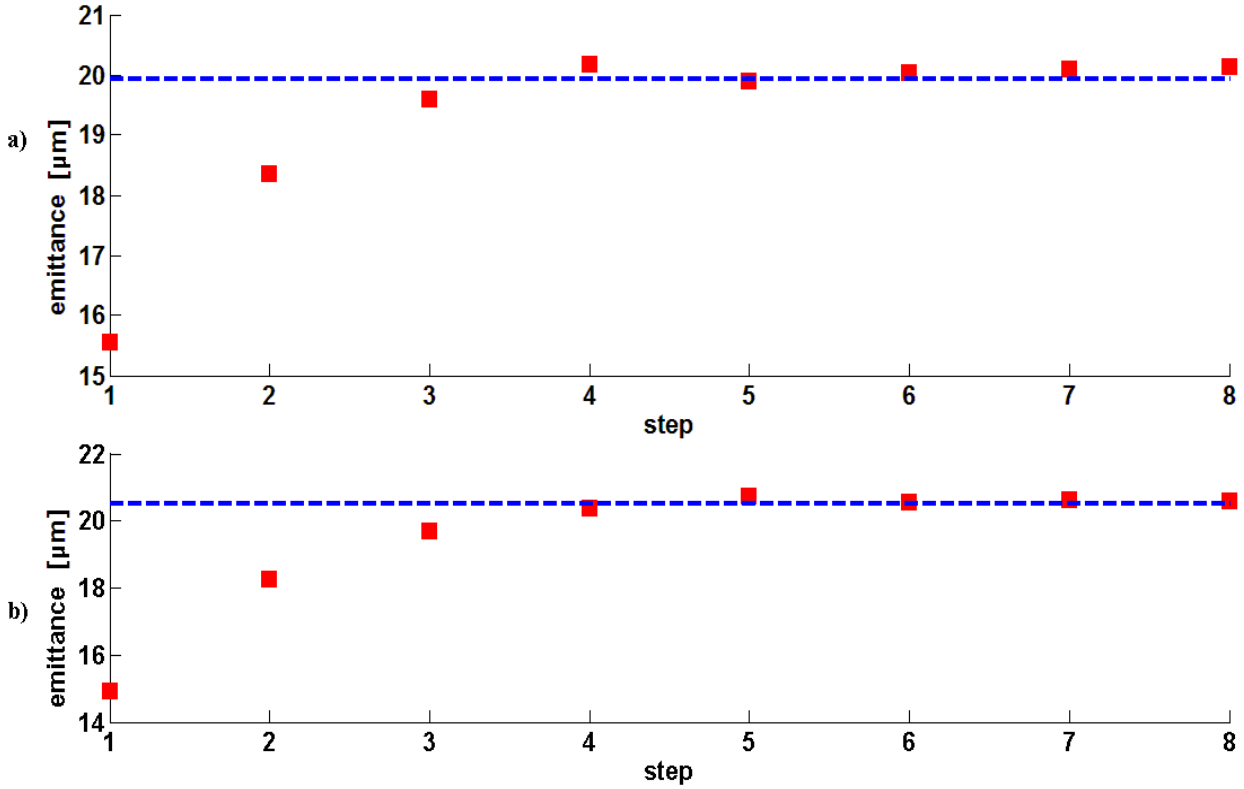

Figure 4.4: Plot showing convergence of emittance for (a) a medium space charge beam ($K = 2.83 \times 10^{-4}$), and (b) for a high space charge beam ($K = 7.06 \times 10^{-4}$).

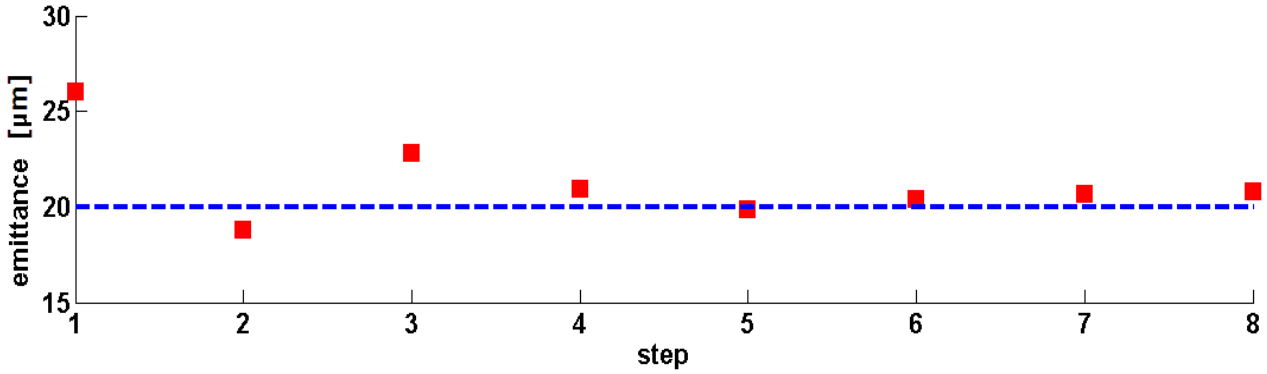

Figure 4.5: Plot showing convergence of emittance for an elliptical beam with medium space charge ($K = 2.83 \times 10^{-4}$).

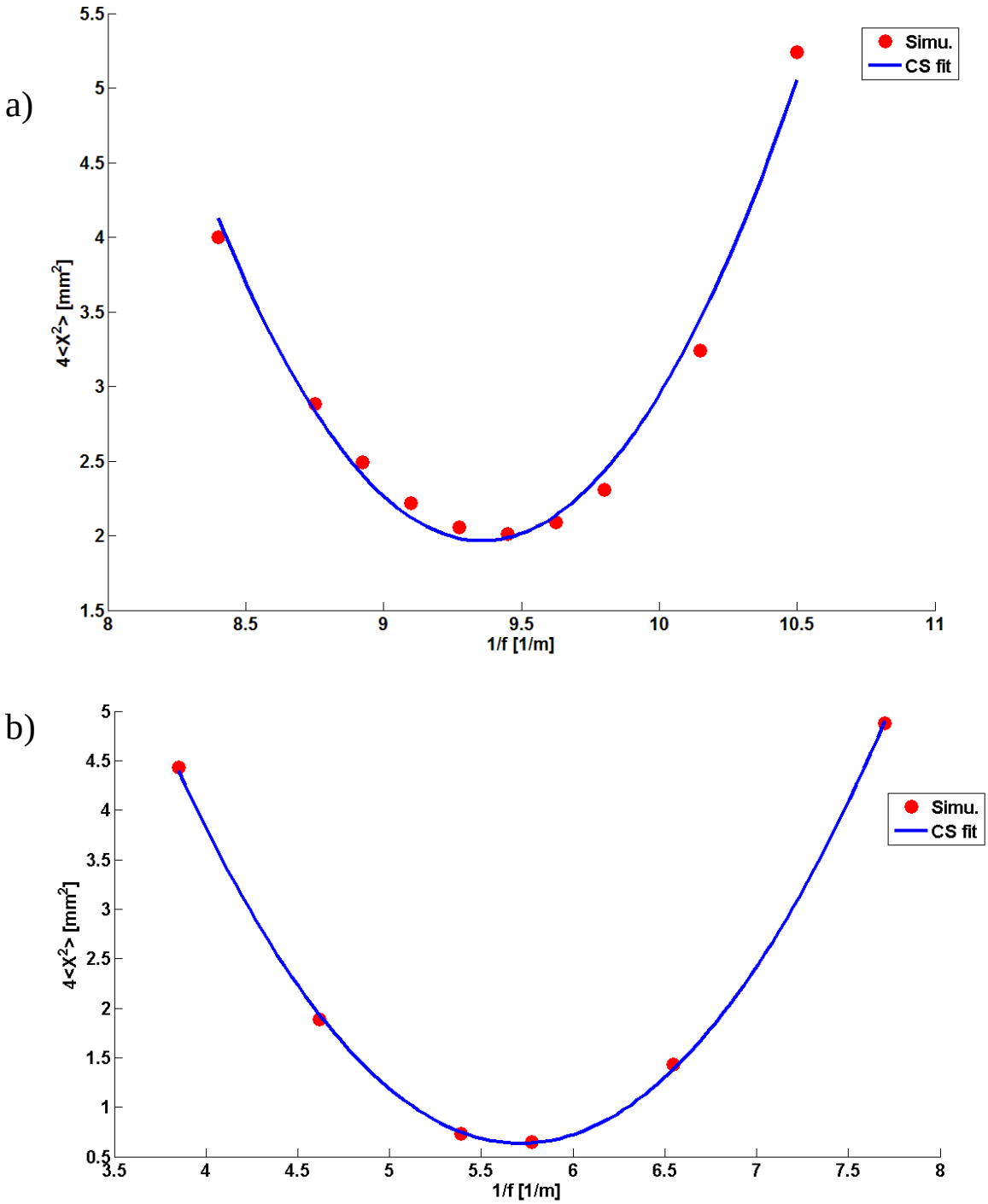

Figure 4.6: Plot showing quadrupole radius scan for (a) beam with high space charge ($K = 7.06 \times 10^{-4}$) and (b) emittance-dominated beam ($K = 7.35 \times 10^{-6}$). Blue curve is a quadratic fit to the simulated data samples shown with red circles. The goodness-of-fit parameter is 0.95 for case (a) and 0.999 for case (b).

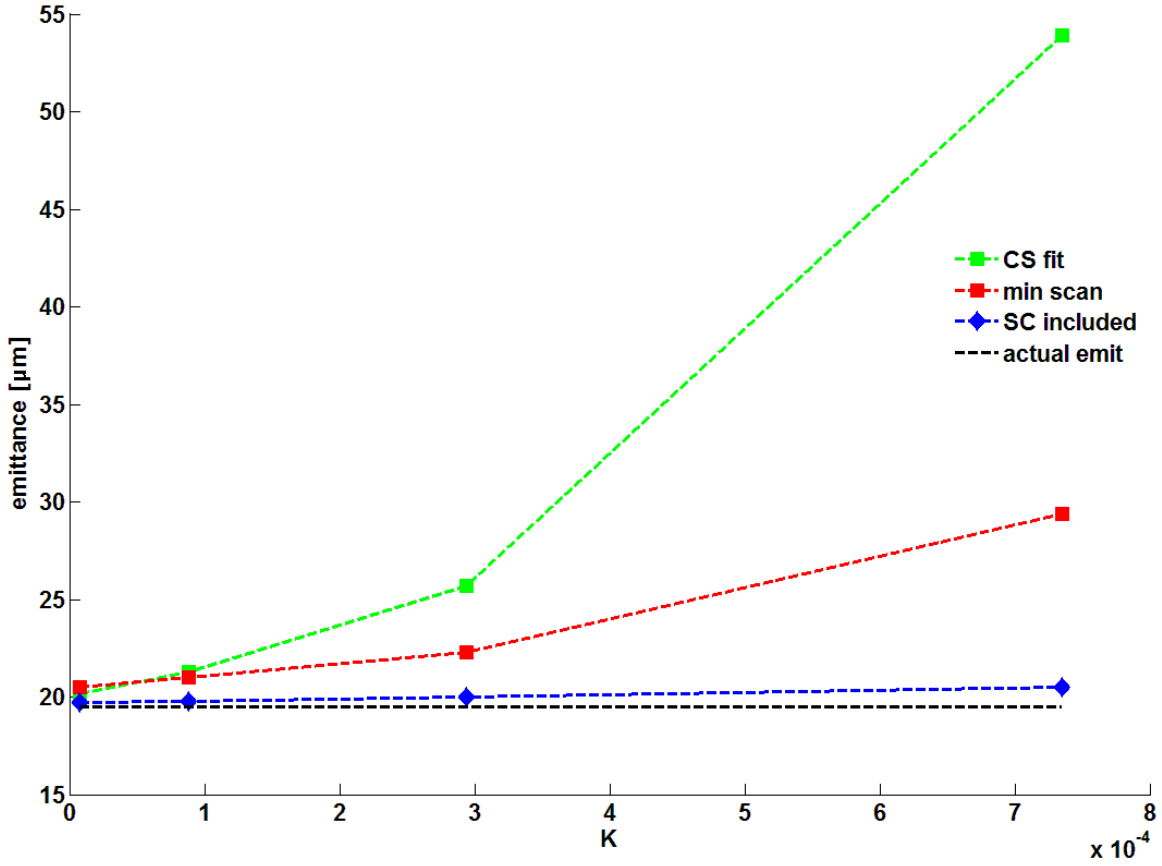

Figure 4.7: Comparison of the emittance measured using different methods as a function of beam perveance (K): dashed green curve: CS parameter fitting method, red curve: cross-correlation determination at minimum of quad beam size scan, blue curve: two value method including space charge, showing small deviation from the actual emittance.

In a real experiment there are errors associated with the measurements. These errors will, certainly, lead to error in the calculation of cross correlation and consequently the emittance. Such emittance errors are affected by the choice of focal lengths.

There are two criteria's for selecting the focal strengths, f_1 and f_2. First, simple error analysis of the emittance relation shows that for a precise calculation, cross-correlation term should not be larger than the emittance itself.

This way, a 10% error in cross correlation translates roughly to the same 10% error for the emittance. If the cross correlation is about 3 times the emittance then the same 10% error in cross correlation introduces a 30% error into emittance. A good rule of thumb is to measure the emittance and see how it is compared with the cross correlation. The result could be dismissed if emittance is smaller.

The second criterion is how far or how close f_2 can be chosen in respect to f_1. Expectedly, choosing closely spaced focal lengths lead to large errors, and therefore it should be avoided. This can be easily checked from the Eq. (23) for the negligible space charge case. To limit the error gain due to the denominator of this equation one may choose f_2 according to:

$$\frac{1}{f_1} - \frac{1}{f_2} > \frac{1}{10L}$$

Figure 4.8 shows how the error on beam divergence affects the emittance precision in the case of high space charge simulated beam. The relative error in emittance is less than 17% for a 10% error in divergence. We notice that by varying f_2 toward f_1, the error increases and at $f_2 = 96\,mm$ which corresponds to $\frac{1}{f_1} - \frac{1}{f_2} \sim \frac{1}{15L}$ the error dramatically increases to more than 100%.

Table 4.1 lists emittance calculation error for various errors in each of beam values for two pairs of size and divergence. Overall, the approach shows robust response to errors in measurements.

Table 4.1: Errors in emittance with respect to beam measurement errors for the high space charge beam ($K = 7.02 \times 10^{-4}$). Beam samples are taken at focal lengths $f_1 = 93\ mm$ and $f_2 = 116\ mm$.

Measurement error	Relative error in emittance
$\sqrt{< x_1^2 >}$: 10%	17%
$\sqrt{< x_1^2 >}$: 5%	6%
$\sqrt{< x_1'^2 >}$: 5%	7%
$\sqrt{< x_1'^2 >}$: 10%	17%
$\sqrt{< x_2^2 >}$: 10%	9%
$\sqrt{< x_2'^2 >}$: 10%	10%

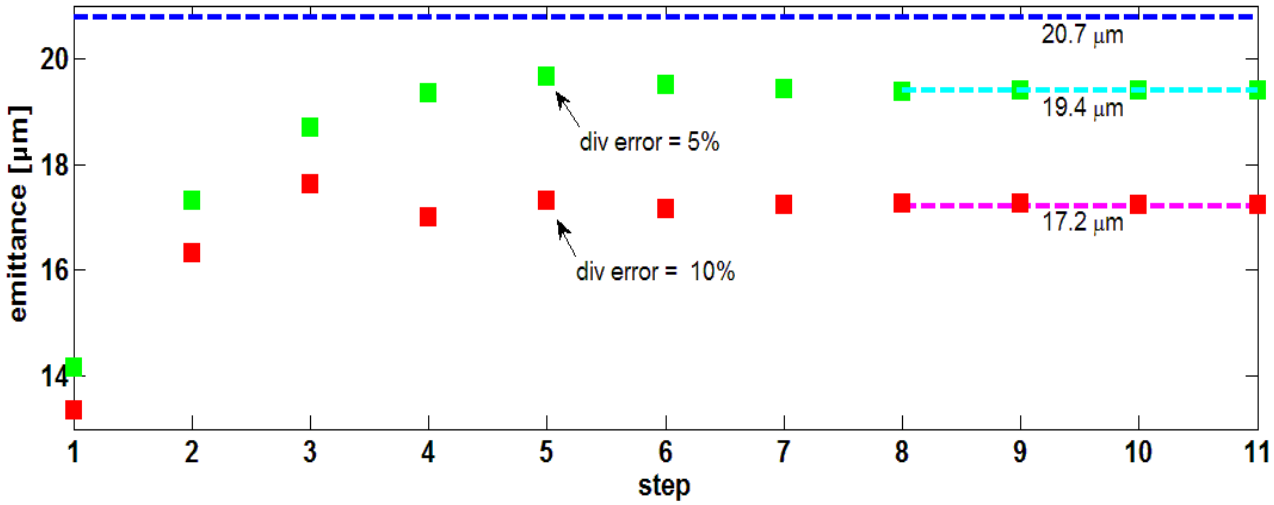

Figure 4.8: Plot showing convergence of emittance for a round beam with high space charge ($K = 7.02 \times 10^{-4}$) when there are 5% and 10% errors in the divergence sampled at the focal length f_1.

The theory makes use of the rms envelope equations, which assumes that emittance is conserved in between the lens and the screen. While such assumption is fulfilled for many beam distributions such as KV, Gaussian, and Thermal (Maxwell-Boltzmann), the emittance varies considerably for some of more realistic distributions with strong space charge. Expectedly, the method is not accurate for extremely high space charge when space-charge driven emittance

growth is appreciable over the drift distance. It was primarily to test this assumption that we conducted self-consistent WARP simulations with different distributions. While the simulations test the distribution-dependent errors, there may be other sources of machine-specific emittance growth that will introduce additional errors.

A similar problem has been studied tomographic phase space reconstruction, where a linear space charge model was assumed [54]. The result of that investigation is that the error from such assumption is limited to 13%, and fits the empirical formula:

$$Error\ (\%) = \ 3 \ + \ 9.8\,\chi^2 \tag{4.40}$$

where χ is the intensity parameter. This parameter is ill-defined for a non-matched beam over the drift distance of quadrupole scan experiment, still an at-lens calculated value according to:

$$\chi = \frac{K}{K + \frac{\epsilon^2}{R(L)^2}} \tag{4.41}$$

can be used to have an estimate of the error.

Fortunately, there is a way to avoid such uncertainties in the measurements. Instead of using KV envelope equations at entry 4 of the method, we can simulate the beam behavior with initial condition given at entry 3 and a distribution inferred from the beam imaging system. The procedure is continued from entry 5 by two pairs of $R(0)$ and $R'(0)$ calculated from the simulations. By using Particle in Cell (PIC) simulations code like WARP we can take any effect into account such as a realistic model of the solenoid and image charge forces which is now considerable for an extremely space charge beam. It is worthwhile to notice that after convergence the emittance given by simulator for the lens may be different than the screen emittance given to it at entry 3. Therefore, by simulating the beam over the drift, we can always calculate the real emittance right before the lens regardless of how much it is different from the

screen emittance. In the other words, the effect of experiment set up on emittance, as measured quantity, is diminished. The results are reliable, as long as the simulator can give us accurate results for the beam distribution at the lens. Needless to say, it is far less challenging for a simulator to give accurate results for the lens-drift-screen set up as a small part of the whole accelerator.

Chapter 5: Measuring Emittance from Scan of Beam Size and Divergence Product

The method discussed in last chapter was based on measuring cross-correlation to determine the emittance. In this chapter, we discuss a method that measures the emittance at magnetic focus settings ($1/f_i$) where the cross-correlation term is negligible. At these values the emittance is simply calculated as the product of beam size and divergence.

According to rms emittance equation for x-plane, the squared product of beam rms size and divergence can be written as:

$$< x^2 >< x'^2 > = \tilde{\epsilon}^2 + < x \cdot x' >^2 \tag{5.1}$$

and thus this product is always greater than or equal to the rms emittance. Our goal is to specify the conditions where the cross-correlation is negligible in a region near the minimum of the product vs. 1/f curve. Then by scanning the focal length (f) in a quadrupole or solenoidal-drift setup and measuring both the beam size and divergence we can infer the rms emittance at the minimum of the product curve [55]. This chapter continues as follows. First, in section 5.1, we treat the condition problem for both the emittance and space charge dominated regimes. Then, in section 5.2, we present some practical considerations of the method. In section 5.3, we discuss the results of validating our approach with simulated beams, and finally, in section 5.4, we show how using a quadrupole may weaken the effects of space charge forces and consequently allow for more precise measurements of the emittance.

5.1 Making Cross-correlation Term Negligible

In this section, we first derive the condition for cross-correlation of emittance dominated beams to be negligible at the minimum of Size and Divergence (SD) versus 1/f curve, and then discuss such constraint for beams with space charge.

We suppose the same quadrupole-drift-screen setup as used in the common quadrupole scan experiment. Based on Eqs. (4.5) and (4.7) of the last chapter, we can expand Eq. (5.1) as:

$$< r_L^2 >< r'^2_L > = \tilde{\epsilon}^2 + \frac{1}{16}\left(R_0 \cdot {R'}_0 + (\frac{\epsilon^2}{{R_0}^2} + {{R'}_0}^2) \cdot L\right)^2 \tag{5.2}$$

where subscript L denotes the measurements at screen, which is located at the distance L from the center of the lens. ${R'}_0$ is related to f, the focal length of the quadrupole, through Eq. (C3) which is also given here:

$$\frac{1}{f} = \frac{{R'}_C - {R'}_0}{R_0} \tag{5.3}$$

Plugging Eq. (5.3) into Eq. (5.2) leads to:

$$< r_L^2 >< r'^2_L > = \tilde{\epsilon}^2 + \frac{1}{16}\left(A\frac{1}{f^2} + B\frac{1}{f} + C\right)^2 \tag{5.4}$$

Where, B, and C constants are given as:

$$\begin{cases} A = {R_0}^2 L \\ B = -{R_0}^2 - 2R_0 {R'}_C L \\ C = R_0 {R'}_C + \dfrac{\epsilon^2}{{R_0}^2} + {{R'}_C}^2 L \end{cases} \tag{5.5}$$

Note that the rms emittance, ϵ^2, appears in the relation for C. We assume that the emittance is constant over the drift length and it does not vary when focal strength of the lens changes. Then the rms emittance is equal to the product of beam size and divergence at zeros of the quadratic equation on the r.h.s of Eq. (5.4). The existence of such zeros is tied to the

condition $B^2 \geq 4AC$ which translates to the following constraint when A, B, and C given by Eqs. 5.5 are used:

$$L \leq \frac{{R_0}^2}{2\epsilon} = L_{max} \tag{5.6}$$

Since the envelope size at lens, R_0, and the effective emittance ϵ are properties of the beam, Eq. (5.6) provides a condition on the drift length which insures that the cross-correlation term is zero at least one focal strength. The inequality (5.6) can be applied to either of x or y planes. The overall constraint on L is obviously the minimum of the x and y limits:

$$L \leq \min\left(\frac{< x_0^2 >}{2\tilde{\epsilon}_x}, \frac{< y_0^2 >}{2\tilde{\epsilon}_y}\right) \tag{5.7}$$

To see how this constrains the drift length in a real measurement system we plug in some typical representative values. Assuming envelope rms radius of 1.8 mm and rms emittance of about 0.2 microns at the location of lens, the upper limit on L is calculated as:

$$L \leq \frac{1.8^2}{2 \times 0.0002} \simeq 8\ m$$

Note that in this example the beam is round with similar emittances for both planes. Although we need to calculate the L_{max} based on the R_0 and ϵ to be given by the simulations, we can generally have an approximate upper limit based on worst case estimates of these parameters. Using more conservative values of 1.5 for rms size and 0.25 microns for the rms emittance gives the modified limit of:

$$L \leq \frac{1.5^2}{2 \times 0.00025} = 4.5\ m$$

The upper limit of 4.5 m guarantees that there is at least one focal setting for which the beam rms size divergence product is equal to rms the emittance.

The limit on L can also be explained in terms of the location of beam envelope waist. Note that if the beam waist occurs between the lens and the screen, then the slope of the envelope at the screen is never zero. In the other words, the slope always remains positive indicating a divergent beam. This leads us to hypothesize that there is a maximum for S_W, the distance between the lens and the waist, and this maximum is equal to L_{max}. Here, we show that this hypothesis is in fact true.

The S_W is obtained by finding zero of $R'(s)$, given in Eq. (4.5) with L replaced by s:

$$S_W = \frac{-R_0 \cdot {R'}_0}{\frac{\epsilon^2}{{R_0}^2} + {{R'}_0}^2} \tag{5.8}$$

When we vary the focal length, ${R'}_0$ changes according to Eq. (5.3). Therefore, the maximum of S_W can be found by evaluating the S_W at the value of ${R'}_0$ where the derivative of S_W with respect to ${R'}_0$ vanishes. We obtain:

$${R'}_{0m} = -\frac{\epsilon}{R_0} \quad where \ \frac{dS_W}{d{R'}_0} = 0 \tag{5.9}$$

and thus:

$$S_W(max) = \frac{{R_0}^2}{2\epsilon} = L_{max} \tag{5.10}$$

Figure 5.1 shows several plots of the radius of the beam envelope as a function of the distance z along the beam line for different values of ${R'}_0$. It can be easily seen that since beam slope is always positive after the waist, for L larger than L_{max}, the envelope slope and therefore cross-correlation according to Eq. (4.7) remains non-zero for the whole range of focal strengths.

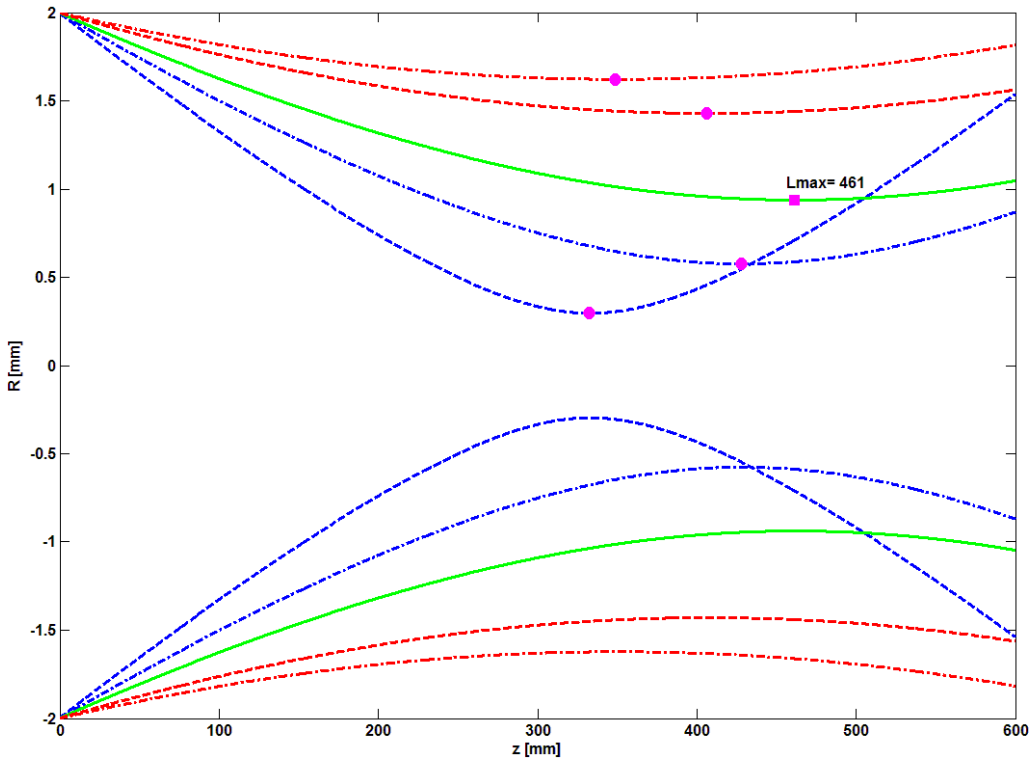

Figure 5.1: Plots show how envelope waist responds to variation in focal strength of the lens for a space charge dominated beam. Increasing R'_0 from 0 to R'_{0m}, changes the waist location from 0 to $S_W(max)$. The red curves show two of such envelopes. The green plot represents an envelope with waist at $S_W(max)$ which is equal to L_{max}. Further increasing the R'_0 makes the waist come closer as can be seen from the blue envelope plots. Theoretically, the waist can come as close as possible to lens by going to higher focal strengths. Notice that beam slope after $S_W(max)$ is always upward (nonzero) suggesting that SD product scan measured at $L > S_W(max)$ becomes larger than rms emittance.

The fact that the limit on L is the limit on maximum distance a waist can form, helps to better explain the dependence of maximum drift length on space charge. It should be noted that the equivalency of L_{max} and $S_W(max)$ is true regardless of space charge. While we proved that this is true for an emittance dominated beam, we need to resort to following explanation for why these two values should match in general. We showed that L_{max} cannot be larger than $S_W(max)$.

The simple question is: can it be smaller than $S_W(max)$? The answer is negative due to the fact that cross-correlation at $s = S_W(max)$ is zero, and therefore L_{max} cannot be smaller than $S_W(max)$. Thus, these two should be equal.

Now, we consider the case where the beam has some space charge, and check how the limit on L changes. Intuitively, space charge should make the L bound smaller as repulsive inter particle forces add to the thermal expansion of the beam due to emittance. Mathematically, this is equivalent to having a larger effective emittance in the denominator of the Eq. (5.6), which consequently lowers the upper bound on L.

As in the case of emittance dominated beams, the KV envelope equation can be used to solve for the beam slope and the envelope along the drift length. However, as it is shown in [48] $R'(L)$ cannot be written in terms of beam parameters at the lens in the same way as has been done previously (see Eq. (4.5)). Consequently, cross-correlation cannot be given in a closed form as a function of the focal length f; thus an analytical approach to derive an upper limit on L deems impossible. Instead, we study the variation of the upper bound on the drift length in relation to amount of space charge in the beam, represented by the generalized perveance K, by numerically solving the envelope equations. In the section 5.3, we validate our analysis with Parmela simulation results.

Figure 5.2(b) shows a number of SD product scan plots for a low space charge beam for different values of L. As can be seen, when L is large the SD product scan curve touches the emittance line at two focal strengths representing the two roots of the quadratic equation in r.h.s of Eq. (5.4). By increasing L, these two points get closer and eventually they merge with each other. This single minimum point is achieved at $L = L_{max}$ and further increase of L results in a displacement of the minimum from the emittance line. The reason the minima move toward each

other as L increases can be understood analytically in the emittance dominated case. The difference of the two zeros of the quadratic equation on the r.h.s of Eq. (5.4) can be written as:

$$\left|\frac{1}{f_{m1}} - \frac{1}{f_{m2}}\right| = \sqrt{\frac{1}{L^2} - \frac{1}{{L_{max}}^2}} \tag{5.11}$$

Thus, increasing L makes the zeros closer to each other until they become equal at $L = L_{max}$. The same behavior is also seen for beam with space charge.

As can be noticed from the example given in figures 5.2(a) and 5.2(b), L_{max}, measured to be 4.8 m for the low space charge beam is smaller than the no space charge case, i.e. 6.48 m.

To see the trend of space charge effects on L_{max} we can measure it by the same way for higher space charge beams. Figures 5.3(a) and 5.3(b) provide SD product scan plots over several values of L for medium and high space charge beams. L_{max} calculated for these space charge regimes decreases to 2.4 m and 0.85 m respectively.

Table 5.1 lists L_{max} with respect to K for several grades of space charge. To have a comparative measure of space charge of the beams, the χ value, representing the relative space charge and emittance forces, are also given for each beam. Note that the focal strength range over which the minimum is attainable increases as L decreases.

a)

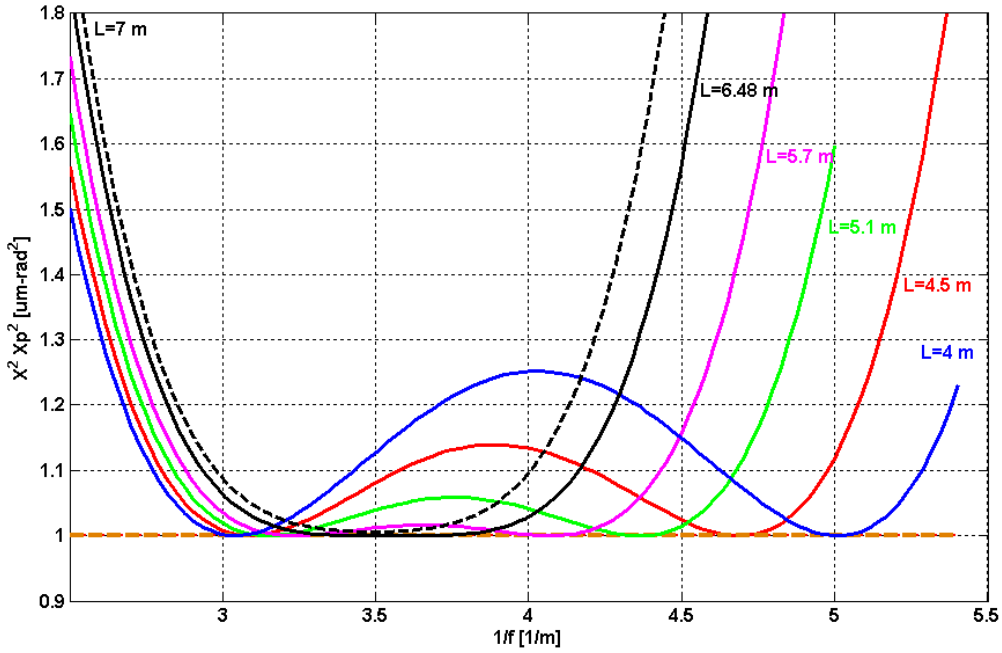

b)

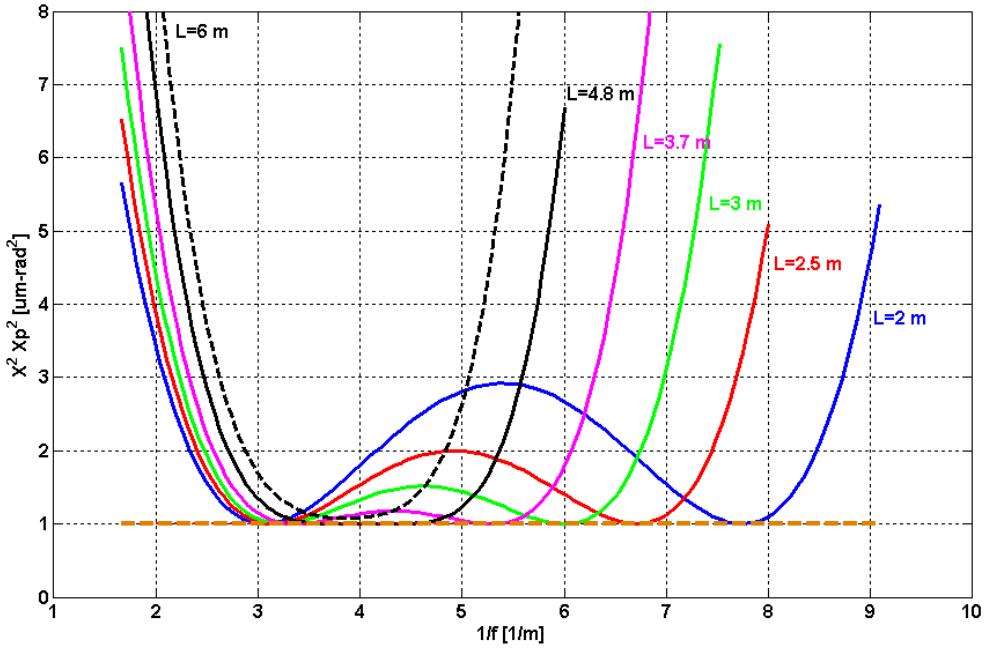

Figure 5.2: Plots showing SD product scan curves over several values of L for (a) an emittance dominated beam ($K = 0$), and (b) a low space charge beam ($K = 1e-6$). Emittance is 1 μm in both cases. The black curve represents the case when L is equal to L_{max}. The dashed black shows the case when L is smaller than L_{max} and then the SD scan does not touch the emittance line shown in dashed brown. Other curves show various instances of SD scans that have two minimums both equal to the emittance.

Table 5.1: Results of calculating L_{max} for several grades of space charge. The L_{max} drops as parameter K increases.

K	$\boldsymbol{\chi}$	$\boldsymbol{L_{max}}$ $[\boldsymbol{m}]$
0	0	6.48
$1e-7$	0.0909	4.8
$1e-6$	0.5000	2.4
$1e-5$	0.9091	0.86
$3.1e-5$	0.9688	0.50
$5e-5$	0.9804	0.39

Theoretically, we can determine emittance by measuring only one of the minimums of the SD product scan when L is smaller than L_{max}. However, we note that the minimum of SD product scan gives the emittance at $s = L$ and not at the location of the lens where it is presumed to be measured. In reality, for sufficiently small L the measured emittance at screen deviates, although by small amounts, from the emittance at the lens. This means that the lens-drift-screen setup used for the measurement of the emittance is affecting the quantity of measurement, in the same way as a thermometer may alter the temperature it measures. Therefore, small L may adversely affect the whole emittance measurement and should be avoided.

a)

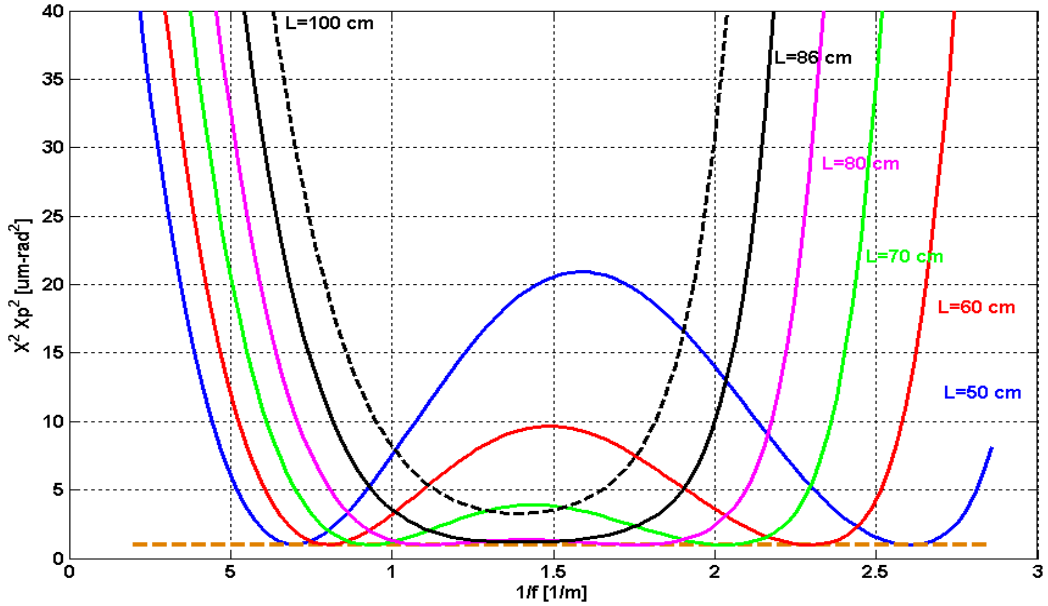

b)

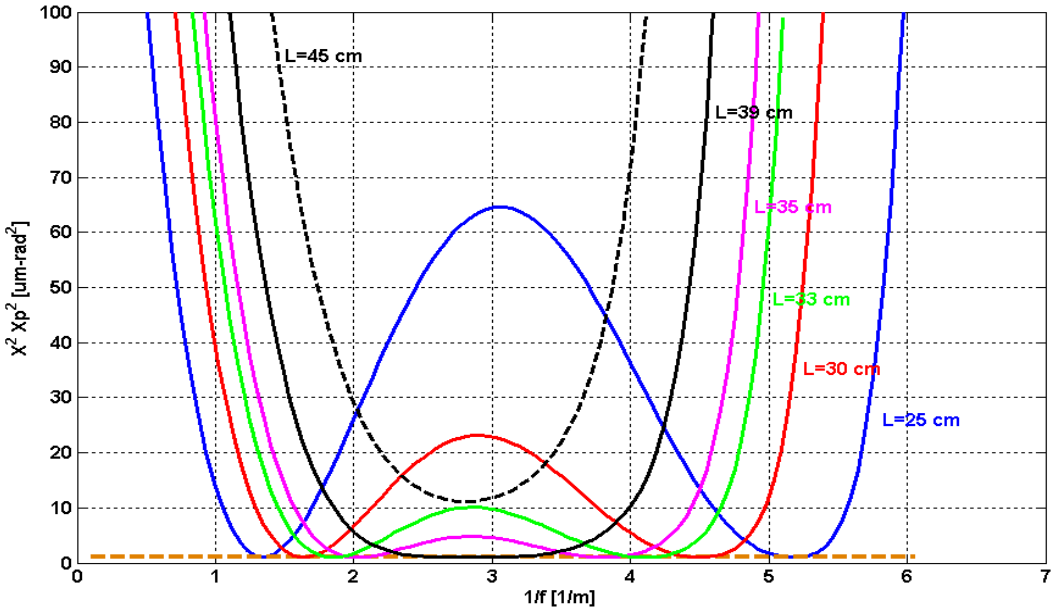

Figure 5.3: Plots showing SD product scan curves over several values of L for (a) a medium space charge beam ($K = 1e-5$), and (b) a high space charge beam ($K = 5e-5$). Emittance is 1 μm in both cases. The black curve represents the case when L is equal to L_{max}. The dashed black shows the case when L is smaller than L_{max} and then the SD scan does not touch the emittance line shown in dashed brown. Other curves show various instances of SD scans that have two minimums both equal to the emittance.

5.2 Practical Considerations

Measuring divergence poses more challenge than measuring the beam size. Therefore, it is favorable to limit the focal range and then the number of divergence measurements. Since it is simple to measure the minimum of beam size and find the focal length where it occurs, we will first consider the condition when both the minimum of the SD product scan and the beam size approximately match. In [48] it is shown that at the minimum of beam size scan we have:

$$R'_0|_{f=f_m} = -\frac{R_0}{L} \tag{5.12}$$

On the other hand, the minimums of SD product scan occur at zeros of the quadratic equation in r.h.s of Eq. (5.4). The one closer to the minimum in beam size scan is:

$$R'_0 = -\frac{R_0}{2L} \pm \frac{R_0}{2}\sqrt{\frac{1}{L^2} - \frac{1}{{L_{max}}^2}} \tag{5.13}$$

For $L \ll L_{max}$ we obtain:

$$R'_0 \gtrsim -\frac{R_0}{L} \tag{5.14}$$

Therefore, if L_{max} is much larger than the drift length, which may happen when the initial beam envelope radius is large or emittance is small, we reach a regime where cross-correlation term at the minimum of beam size scan becomes negligible. To measure the emittance in this case, it is only necessary to measure divergence at a single focal length where beam size minimum occurs.

The minima become farther apart as L becomes larger. This leads us to adopt the following strategy in order to minimize the number of beam divergence measurements. First, we find the beam size minimum. Then we increase the R'_0 by decreasing the focal strength of the lens and sample the beam divergence. This way, the minimum in SD product scan is found by sampling beam divergence at fewer numbers of focal settings.

One of the potential problems in using SD product scan method for measuring emittance is an impractical measurement range for the beam divergence around the minimum of the scan curve. Generally, the OTRI technique can measure divergence down to about $0.01/\gamma$ or about $0.5\,mrad$ for the situation with acceptable errors. Therefore, cases shown in Figure 5.3 (a) cannot be measured accurately if the divergence goes down to $0.2\,mrad$. The remedy is to trade the beam divergence with the beam size by decreasing the beam radius right before the scanning lens. It has been shown that for the emittance dominated beam, the minimum of the divergence scan is related to R_0, initial beam radius at the lens, by [?]:

$$< x' >_{min} = \frac{\epsilon}{R_0} \tag{5.15}$$

Such dependence, although in a weaker form, is true for beams with space charge. To decrease R_0, we can adjust the focal strength of the lens right before the scanning lens. However, we note that by decreasing R_0, we are also decreasing L_{max}, which can affect the feasible drift length of the experiment. Therefore, there is a trade-off between the L_{max} and minimum of the divergence, $< x' >_{min}$. Figure 5.4 shows how these two vary with respect to R_0 for a beam with moderate space charge.

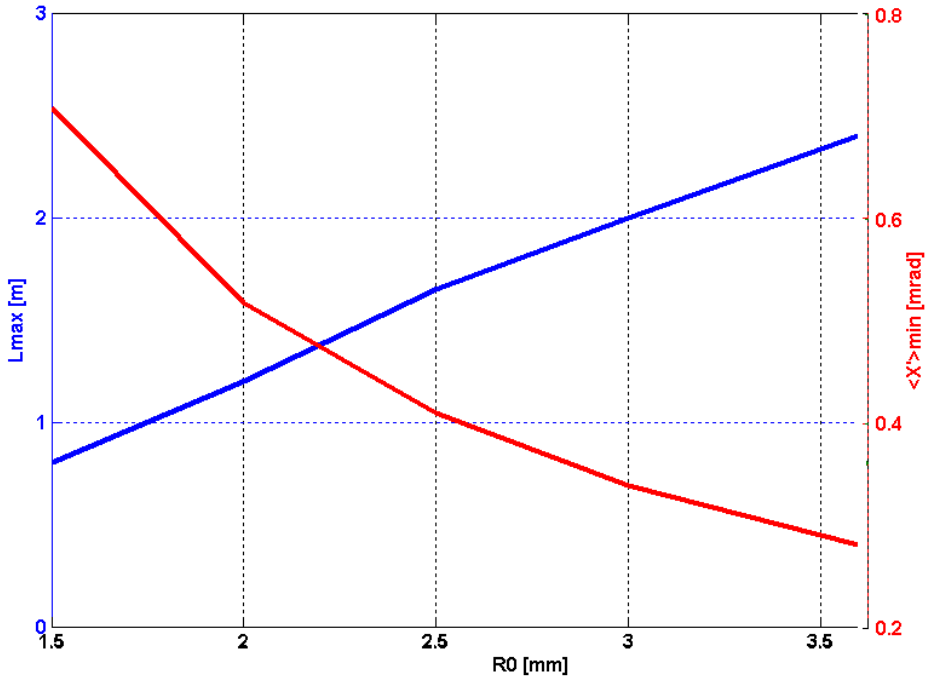

Figure 5.4: Plot showing variation of L_{max} and $< x' >_{min}$ with respect to R_0 for a beam with moderate space charge ($K = 1e-6$, $\epsilon = 1\ \mu m$). The $< x' >_{min}$ is measured at $L = 50\ cm$.

5.3 Simulation Results

In this section, we present testing results of our SD product scan approach to measure the emittance with simulated beams. We used the software PARMELA [56-57] to simulate the lens-drift experiment. Similar to the WARP, PARMELA uses a self-consistent electrostatic particle-in-cell model to simulate the beam. To produce more realistic results, the AWA lattice with lens-drift-screen setup was used. The code PARMELA has been successfully benchmarked against AWA experimental data in the past [58].

The diagram in figures 5.5 shows the modified lattice of AWA with a scanning solenoid located at $z = 700\ cm$ and OTRI screens placed at a distance $L = 1\ m$. The length of the solenoid is 10 cm. The simulations were done for beam energies of 8.5 MeV and 14 MeV. As it was pointed out earlier in the chapter 3, the AWA uses a photo RF-gun, and the PARMELA

generates the beam distribution based on radius, wavelength, and power of the laser spot shone on the photo-cathode. We calculated the L_{max} earlier in this chapter for the AWA and it was about 8.5 m. Therefore, the drift length of 1 m, which is far smaller than L_{max}, helps us to have two distinct minimums for the SD product scan. For the AWA nominal charge of 1 nC, and the beam pulse FWHM of 8 ps, the peak current is 125 A, which in turn leads to the following value for the generalized perveance:

$$K = \frac{2 \cdot I}{I_0 \cdot (\beta\gamma)^3} \cong 7.16 \times 10^{-7}$$

As the simulation starts from the gun, PARMELA does not require the emittance to be specified. The beam is simulated over the whole lattice including the lens-drift-screen located between $z = 700\ cm$ and $z = 800\ cm$. Figure 5.6 shows normalized emittance evolution curve of the AWA lattice assuming no focusing is applied in the scanning lens. The rms emittance at location of the screen is approximately 0.18 μm. Plots in figure 5.7 show sample simulated envelope curves for both solenoid and quadrupole lenses.

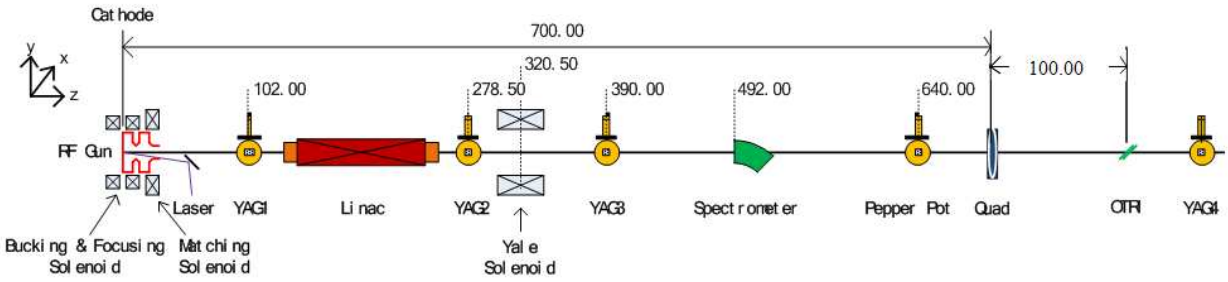

Figure 5.5: Modified lattice of AWA with a solenoid located at z=700 cm and OTR screens placed at the distance 1 m from it.

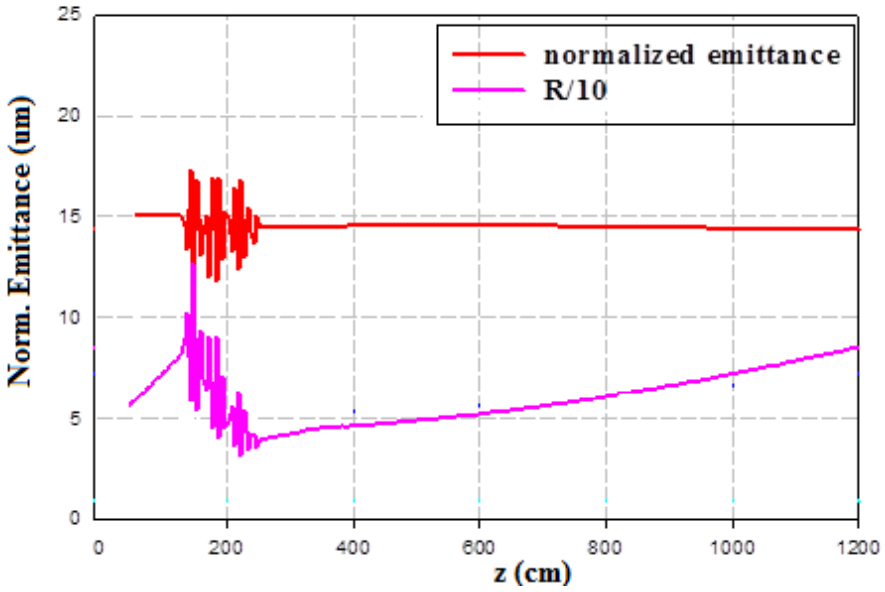

Figure 5.6: The red curve shows the rms normalized emittance for the simulated 1 nC beam in AWA. The scanning lens is a solenoid located at $z = 700\ cm$. Starting from end of the LINAC, the normalized emittance remains fairly constant. The purple curve shows the ratio of space charge to emittance forces. As it is mostly beyond 50, the 1 nC beam is space charge dominated.

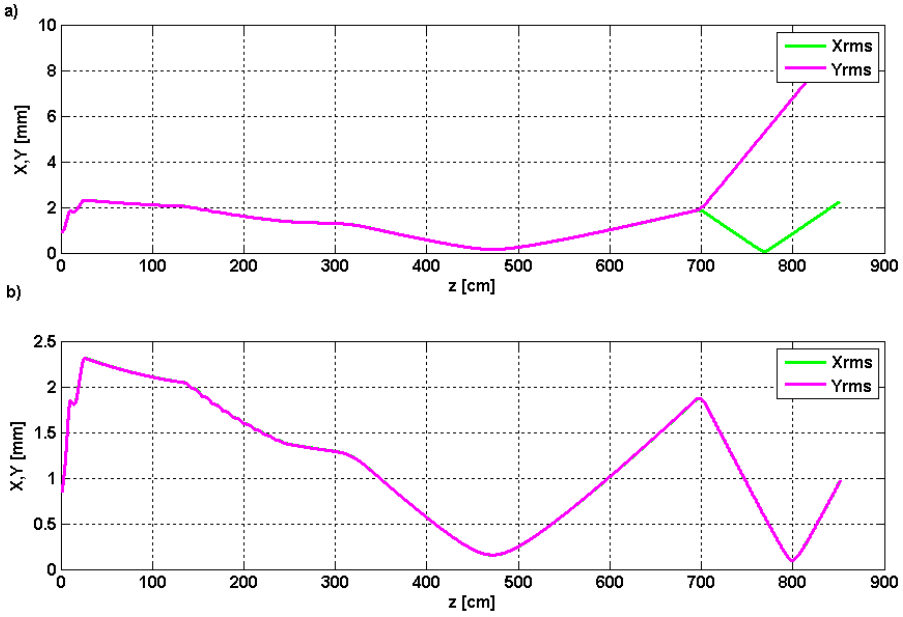

Figure 5.7: Simulated rms envelopes of 1 nC beam in AWA for scanning lens located at z=700 cm to be (a) a quadrupole and (b) a solenoid. The beam charge is 1 nC. As can be seen the beam stays round over the whole accelerator length in the case solenoid. The size of waist in the case quadrupole is smaller than the case solenoid mainly because the space charge repelling forces are more effective in the solenoid case. A complete analysis of this quadrupole behavior is given in the next section.

As will be discussed in the next section, the quadrupole makes the beam less space charge dominated in the drift region. Therefore, to verify the effectiveness of the mentioned approach for space charge dominated beams we used a solenoid.

PARMELA varies the focal strength of the solenoid by varying the magnetic field over the range [0 - 3000] Gauss and generates a set of beam radius and divergence rms values $< x^2 >$ and $< x'^2 >$ at end of the drift section, where the beam size and divergence are supposedly measured, e.g. using OTR and OTRI, respectively. The green plot in Figure 5.8 shows the SD product while the black line depicts the simulated rms emittance of the beam at the screen. This

line touches the scan curve at its two minima verifying that SD product minima produce the true beam emittance. It should be noted that the 1 nC beam is a space charge dominated beam according to the purple plot of Figure 5.6 which shows the relative space charge and emittance forces. The fact that L is small has led to having two distinct minimums for the SD scan curve. As it was mentioned earlier whenever the SD curve has two distinct minimums then the cross-correlation is zero at the minimums and thus such minimums are equal to rms emittance.

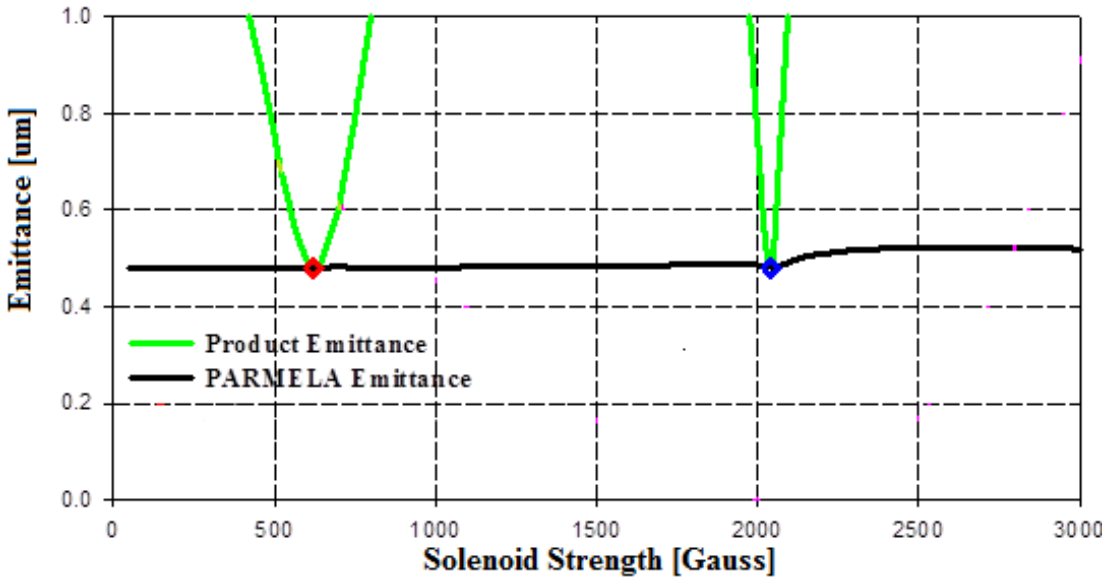

Figure 5.8: SD product scan for 1 nC beam in AWA. There are two distinct minimums, and emittance remains roughly unchanged for the whole focusing range of the solenoid.

We also did the simulated experiment for the 10 nC beam bunch. Figure 5.9 shows similar plots for this case. As can be seen, even for such a high space charge beam, the minimums are still equal to rms emittance, although the value of rms emittance for 10 nC beam is different than the 1 nC beam. Also, the rms emittance is modulated by the focal strength of the lens in this case. This is due to the fact that the 10 nC beam shows emittance growth for the strong focusing part of the scan curve. The minimum always determines the emittance at the

screen although this emittance may be different than the emittance at the location of the lens, as pointed out earlier.

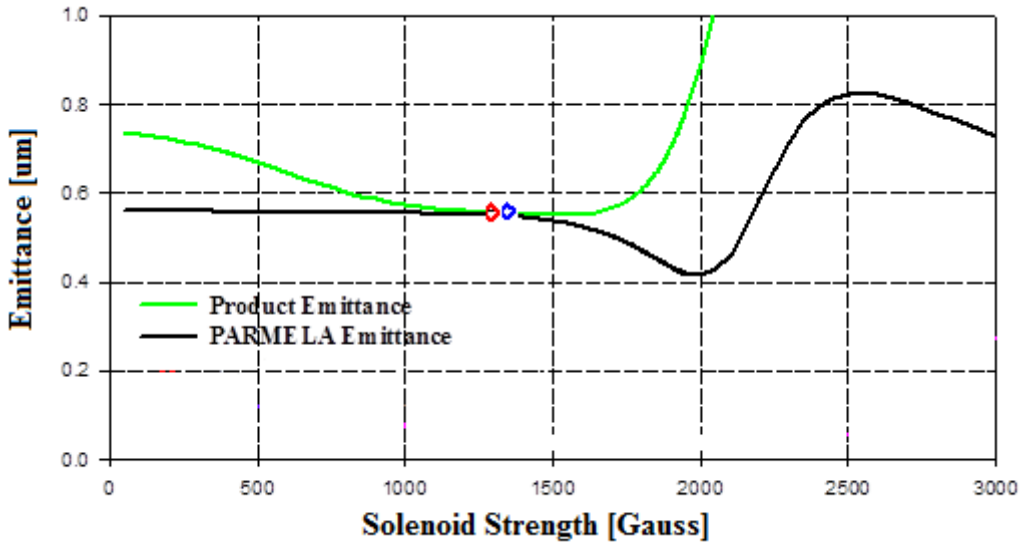

Figure 5.9: SD product scan for 10 nC beam in AWA. As can be seen two minimums merge together in this terminal case. Increasing the charge or lowering the drift length makes the green curve to detach from the black emittance curve. For strong focusing of bigger than 1500 gauss is applied the emittance varies considerably, however, for the focusing range that the experiment is concerned, the emittance remains constant and equal to the emittance right before the solenoid.

5.4 Space Charge Dilution in the Quadrupole

Although methods discussed in the last section and the previous chapter facilitate measuring emittance for beams with space charge, it is always desirable to mitigate the effects of space charge and make the beam behave more like an emittance dominated beam. In this section, we discuss how the choice of lens may affect the balance of emittance and space charge forces.

First, we consider the case when a uniform symmetric lens such as a solenoid is used for focusing. Assuming that the beam is round before the scanning solenoid, it remains round in the drift region as well, and thus the envelope over the drift is described by:

$$R'' - \frac{K}{R} - \frac{\epsilon^2}{R^3} = 0 \tag{5.16}$$

The space charge and emittance relative forces is given as:

$$FR_S = \frac{K \cdot R^2}{\epsilon^2} \tag{5.17}$$

Now, we consider the case when lens is a quadrupole, and assume that it focuses in x plane and defocuses in y plane. The X envelope over the drift region in this case is described by the coupled envelope equation:

$$X'' - \frac{2K}{X+Y} - \frac{\epsilon^2}{X^3} = 0 \tag{5.18}$$

Where it is also assumed that: $\epsilon^2 = {\epsilon_x}^2 = {\epsilon_y}^2$.

The relative forces in this case is given as:

$$FR_Q = \frac{2K \cdot X^3}{(X+Y)\epsilon^2} \tag{5.19}$$

As the beam in y plane is divergent, the Y envelope size becomes far bigger than the X size close to the focused part of the beam. This means that FR_Q is expected to be smaller than FR_S for the same focusing strength applied to both lenses. Therefore, while the beam may be space charge dominated right before the quadrupole, it can behave like an emittance dominated beam in the drift region. The following example based on actual AWA beam parameters illustrates how the relative forces can be different for quadrupole and solenoid.

Figure 5.10 shows how FR_S and FR_Q change over the drift length for the AWA envelope curves given in figure 5.5. As can be seen, FR_S is greater than 1 for most part of the drift region

while the FR_Q is less than 1 over the whole drift section, and therefore we can safely regard the beam as emittance dominated in the case quadrupole.

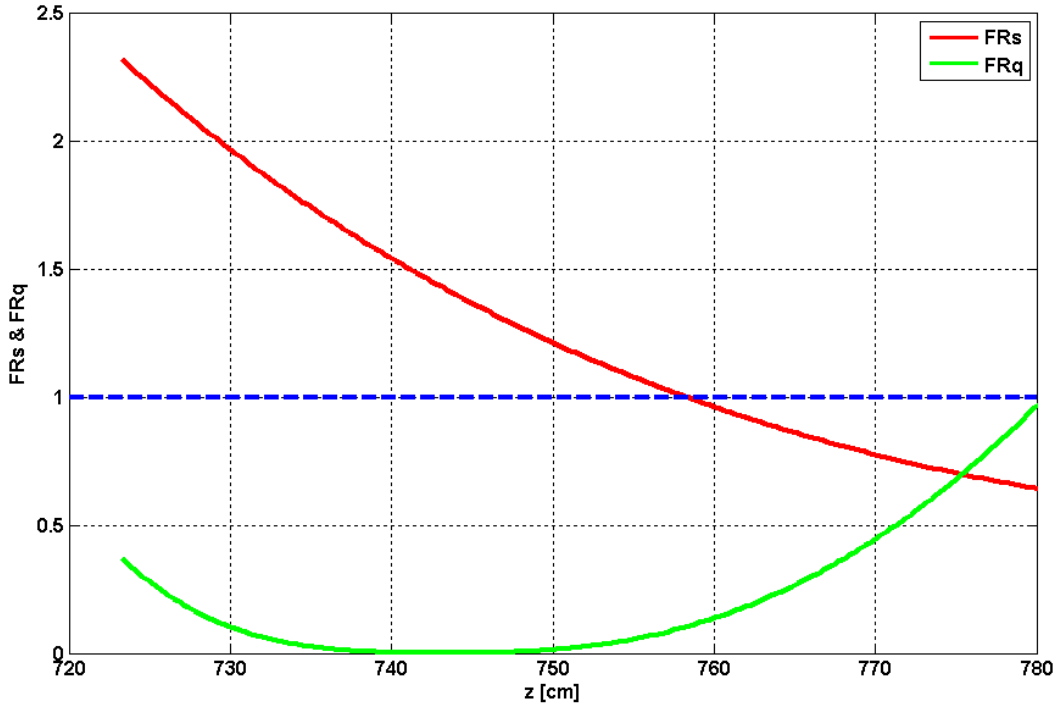

Figure 5.10: Emittance and space charge force ratios over the drift section for the AWA beam simulations of figure 5.5.

As the beam is space charge dominated before the lenses, it is interesting to notice that the use of quadrupole almost reverses the force balance by producing an emittance dominated beam close to the screen. The physical explanation for this behavior is that the beam is shrunk in one plane (x) while being expanded in the other plane (y). Therefore, space charge forces are being consumed for expansion in y, hence they are not much efficient in x plane. One implication of such space charge dilution in the quadrupole case is that the focused envelope (X) becomes more similar to envelope of an emittance dominated beam passed through either lens.

Chapter 6: Experimental Studies of Orbit Control for Space Charge Dominated Beams

This chapter discusses the proposed approaches and their experimental implementations for steering of beams with space charge in UMER. High intensity beams are sensitive to lens nonlinearities and as such nonlinearities increases toward the wall of the ring (especially for imperfect lenses used in research rings), beam excursions inside lenses should be limited more for such beams.

In UMER there is no beam position monitor inside or next to each quadrupole and thus orbit information is not known inside these important focusing elements. To address this problem especially in the high space charge cases, I have developed a method to indirectly infer beam position inside quadrupoles.

Optimizing beam injection is another important subject as it is essential, especially for high space charge beams, to have small betatron oscillations about the closed orbit. In fact, a good closed orbit can be simply made useless by bad injection that leads to high beam excursions. A method has been developed to address this issue.

The chapter is organized as four sections. Section one discusses orbit deterioration due to space charge. Section two covers error-tolerant measurements of closed orbit, and also the measurement of extended closed orbit inside quadrupoles. Next sections cover steering solutions implemented in UMER. The chapter closes with a section on optimizing beam injection.

6.1 Quality of Orbit Requirement for Space Charged Beams

Since steering involves controlling the orbit of the bunch centroid, and as the centroid space charge forces cancel each other, in principle, the steering should not be affected by the amount of the charge in the bunch. However, observations have shown that dipole settings fine-tuned for lower currents can lead to severe beam scraping when applied to higher currents [28]. For example, figure 6.1 compares the BPM signals for two beams in the injection part of the UMER. One is a low space charge beam with a peak current of 6 mA and the other is a high space charge with a peak current of 80 mA. As can be seen, the high space charge beam undergoes severe scraping at the BPM1 (located at the IC2 according to the figure 3.12), while the low space charge beam passes almost intact.

It should be pointed out that steering is not the culprit for all the beam losses. In fact, mismatching and envelope growth can rapidly "kick out" a considerable amount of charge even under "decent" steering.

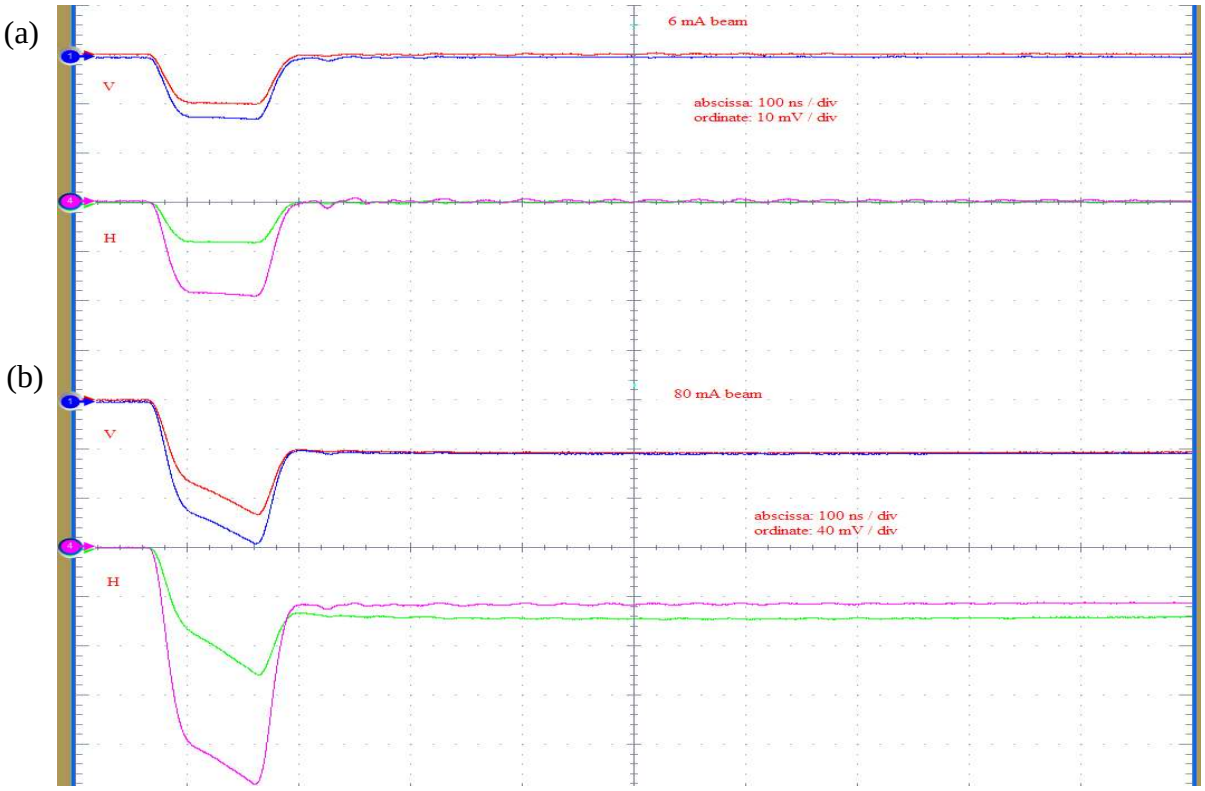

Figure 6.1: Beam position monitor (BPM) signals at IC2 (see figure 3.12) as a function of time for the (a) 6 mA and (b) 80 mA beams, for the same steering settings. The 4 curves in each case correspond to the signals from the 4 plates of the BPM, both horizontal (H), and vertical (V). The fact that the baseline does not return to zero in the 80 mA case is a clear signature of beam scraping.

Apparently, similarly distorted signals from all four plates can be attributed to a swelling beam envelope scraping off the plates. There are three reasons justifying this claim. First, if we calculate the beam centroid position in the case 80 mA by using signals at the edge of distorted pulses, we come up with the same position as the 6 mA beam. It means that the higher current beam is not undergoing external kicks or image charge induced forces. Second, the negative ramps for the BPM plate signals show that charge is deposited on the plates at a roughly constant rate, therefore giving us the distorted plate signal:

$$v(t) = V_b + \frac{I_b}{C}t \tag{6.1}$$

Where V_b is the induced voltage due to the beam centroid, I_b is rate of depositing (scraping) charge on the plate, and C is the capacitance of each plate. As the figure 6.1 shows the scraping current, I_b, is the same for all four plates. If we suppose that there is envelope growth or halo has formed around the beam, then such constant beam charge deposition can be explained.

I did another experiment bolstering my above argument. Based on the steering method discussed in [59], a new setting was made for the steerers in the injection part of UMER, so that the beam passed right through the center of quadrupoles. I used this setting and captured the BPM signals for the 80 mA beam current. Figure 6.2 shows the BPM plate signals. As can be seen there are no distortions in this case. Thus it seems that the intense SC beam is very sensitive to being off-center while passing through the lenses. This experiment and above two arguments lead us to the conclusion that higher intensity beams need higher quality closed orbits.

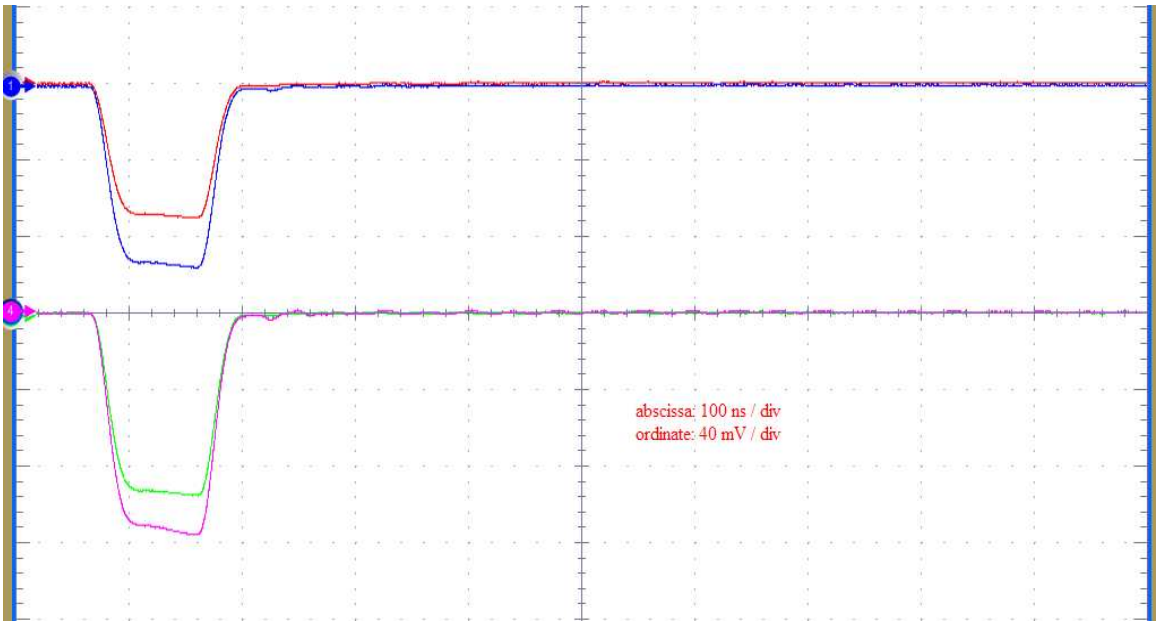

Figure 6.2: BPM signals in IC2 (see figure 3.12) as a function of time for the 80 mA beam captured while using the corrected steering setting making the centroid to pass through the center of the quadrupoles.

Such relation between beam charge and requirement on the quality of closed orbit can be better understood if we analyze the beam centroid behavior with respect to total charge of the beam. By increasing the space charge of the beam, the coherent tune changes due to image charge forces [28]. Therefore, the beam centroid at quadrupoles change and this affects the amount of bending each quadrupole provides for the beam. To put it simply, when the closed orbit at the location of a quadrupole is off center (non-zero) by x_Q (y_Q) then on average the beam is bent by:

$$\theta_x \sim g \cdot x_Q \quad or \quad \theta_y \sim g \cdot y_Q$$

Where g is the field gradient of the quadrupole. Usually this angle is far less than bending angle in a horizontal dipole, however, when the closed orbit inside the lens is quite off-center such angle may modify the closed orbit considerably. Overall, orbit deterioration due to the space charge happens according to the diagram in figure 6.3.

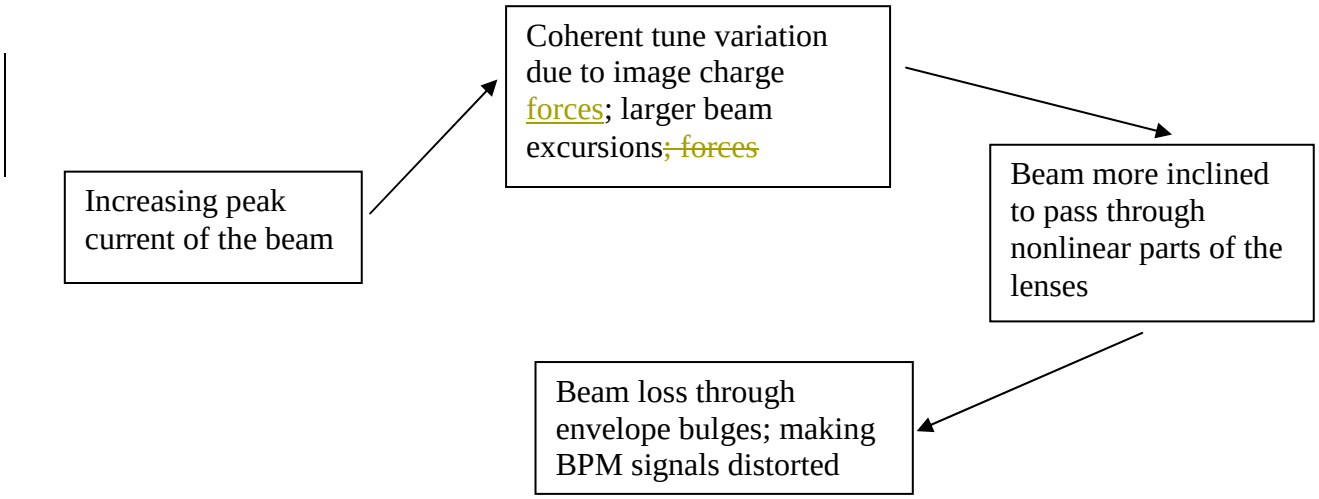

Figure 6.3: Diagram of processes leading to beam loss when the beam carries more charge.

It should be noticed that varying tune for a low space charge beam has no effect on beam steering and closed orbit quality remains unchanged. For high space charge beams two tunes are

defined; coherent tune for beam centroid and incoherent tune for beam particles. It is the coherent tune shift that affects steering for high space charge beams.

6.2 Closed Orbit Measurement in UMER

6.2.1 Modified Closed Orbit Formula

In circular machines such as UMER, fine steering of the beam is dependent on accurate measurement of the equilibrium orbit also known as the closed orbit. At the start of commissioning or trying new ring configurations, which happens frequently for UMER, the beam does not survive for many turns, and consequently averaging over beam position samples is not a precise indicator of the equilibrium orbit. Therefore, a useful closed orbit formula developed at CERN that uses as few as four consecutive samples of betatron oscillations [60]:

$$x_{co} = \frac{{x_2}^2 - {x_3}^2 + x_2 \cdot x_4 - x_1 \cdot x_3}{3(x_2 - x_3) - x_1 + x_4} \tag{6.2}$$

As this formula is ratio of two expressions, it shows a large response to noise in beam position measurements when the denominator becomes small. To overcome this limitation, revised formulas were developed that avoid a term in denominator by including the tune in calculations. This is not a matter of concern as usually, like in Response Matrix processing, first we measure the tune and then the closed orbit.

I derived the following two closed orbit formulas:

$$x_{co4} = \frac{1}{2} \cdot \left(x_2 + x_3 + \frac{x_1 + x_4 - x_2 - x_3}{\Gamma} \right) \tag{6.3}$$

and

$$x_{co3} = x_2 + \frac{x_1 + x_3 - 2 \cdot x_2}{\Gamma} \tag{6.4}$$

Where Γ , the tune dependent term is given as:

$$\Gamma = 4 \cdot \sin(\nu_x \cdot \pi)^2 \tag{6.5}$$

Likewise, vertical closed orbit can be calculated. While the latter formula relies on as few as three position samples to give the closed orbit and this might be helpful in some occasions, error analysis showed that the former has less sensitivity to both the position measurement noise and tune error [61].

Figure 6.4 shows two sets of measurements of the horizontal closed orbit as a function of dipole currents for dipoles 1 to 7 and all 14 BPMs as part of the procedure for measuring response matrix in UMER. The upper graphs were measured with the original formula given in [60], while the other set uses x_{co4}. As the perturbation is small, the closed orbit should show a linear response to perturbation and this can be seen for almost all elements of matrix that have been measured with the modified formula x_{co4}. On the other hand, the elements measured with the original formula of Eq. (6.2) show much non-linearity in variations contrary to expectations. Some curves cannot even show a trend (monotonic increase or decrease) in variations.

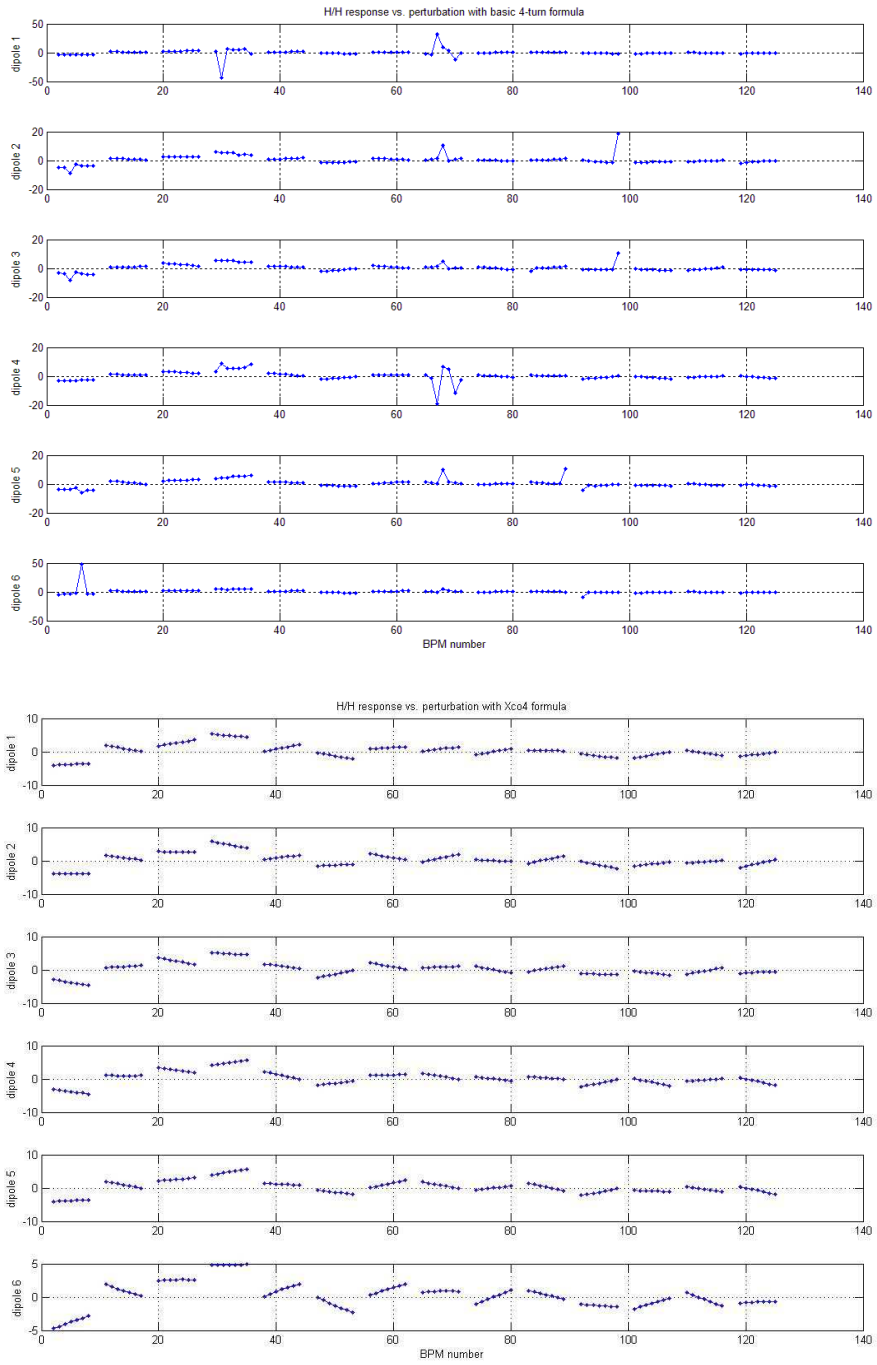

Figure 6.4: Part of horizontal closed orbit response matrix measurements of UMER with x_{co} (upper set) and x_{co4} (lower set).

The accuracy of the new formulas was also verified by applying them to sample beam position data from the SPEAR 3 storage ring at SLAC.

6.2.2 Measurement of the Closed Orbit at the lenses

As it was pointed out earlier, small research rings usually cannot afford for accommodating sufficient number of BPMs to sample the closed orbit. It is obvious that such low sampling does not provide much information about the closed orbit as compared to standard 4-6 samples per betatron wavelength, and makes the fine adjustment of the orbit impossible. For instance in UMER, the closed orbit has always been measured just inside the 14 chambers where BPMs are located around the ring (see figure 3.12). As the common tune is 6.7-6.8, this leads to having mere 2 samples of closed orbit per betatron wavelength.

In [62], I have shown that how the beam centroid could be sampled inside a quadrupole based on indirect position scanning data from nearby BPMs. A summary of the scheme is given here.

According to the figure 6.5, it is supposed that beam centroid passes through the quadrupole at the distance x_Q from the center (in horizontal plane). The beam centroid position in a BPM downstream is measured to be x_B.

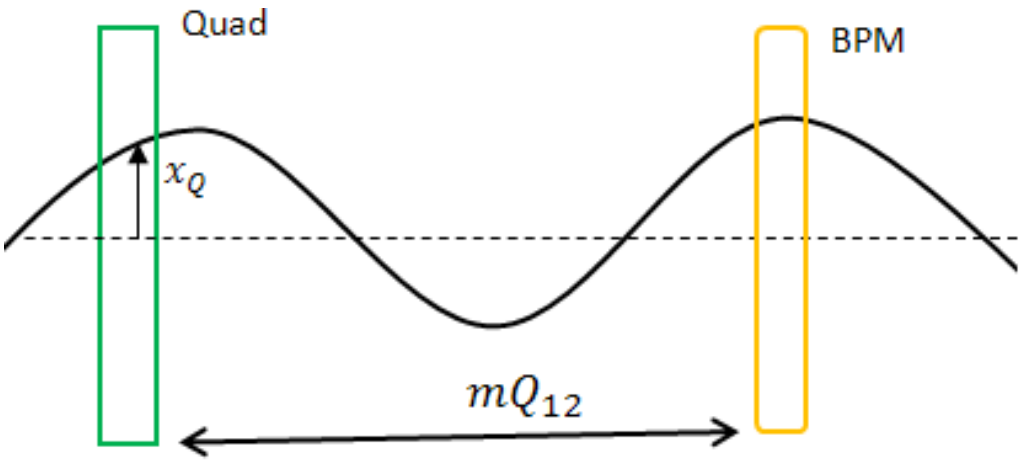

Figure 6.5: diagram showing betatron oscillation of beam centroid passing through a quadrupole and a BPM downstream.

The x_Q can be determined by measuring the slope of variation in x_B vs. scanning quadrupole current I_Q according to:

$$x_Q = \frac{\Delta x_B}{\Delta I_Q} \cdot \frac{P \cdot I}{l \cdot q \cdot g} \cdot \frac{1}{\mathrm{m}_{12}} \tag{6.6}$$

The r.h.s. of Eq. (6.6) has three parts: A quadrupole scanning term that should be measured, the transfer matrix coefficient m_{12} and the constant coefficient,

$$\frac{P \cdot I}{l \cdot q \cdot g}$$

Where P is the particle momentum, I is the quadruple current, l is effective length of the quadrupole, q is electron charge, and g is field gradient inside the quadrupole.

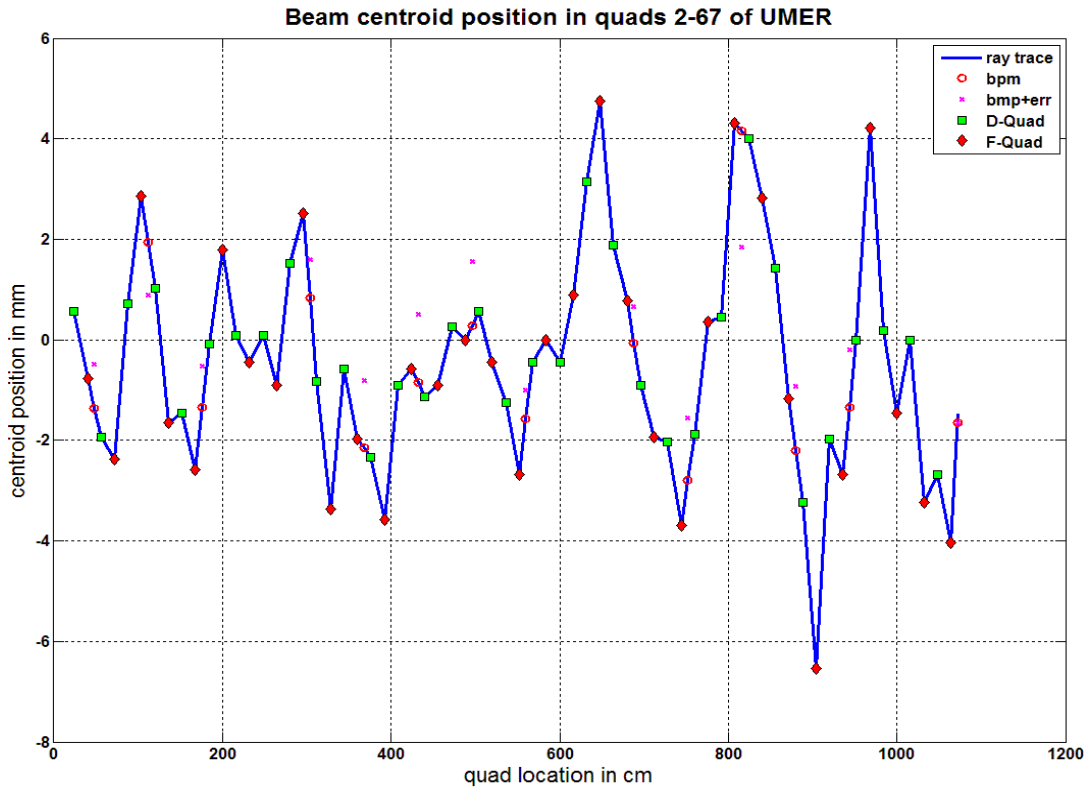

Figure 6.6: Extended horizontal first turn orbit measured for UMER.

Based on this formula, the extensive closed orbit can be sampled at extra 72 quadrupole locations around the ring. This redundant sampling helps to compensate for errors in the

measurements. Eventually, the acquired closed orbit gives a big picture of the beam behavior and facilitates reaching the optimum beam steering for the ring. Figure 6.6 shows the extended horizontal first turn orbit measured for UMER. The first turn orbit is, approximately, equivalent to the closed orbit when the beam is injected on the closed orbit (see section 6.4).

6.3 Orbit Control in UMER

6.3.1 Response Matrix Based Orbit Control

The Closed Orbit Response Matrix (CO-RM) approach has been widely used in system diagnosis and beam centroid control [21]. By applying perturbation somewhere in the ring at a dipole, the closed orbit all around the ring is modified. The closed orbit can be measured by sampling trajectories for three or four turns at BPMs and then calculating the closed orbit (at BPMs) according to formulas given in the section 6.2. The rate of change of closed orbit at a specific BPM j to a change in perturbation angle in dipole i defines CO-RM element i, j as:

$$R_{ij} = \frac{dxCO_j}{d\theta_i} \tag{6.7}$$

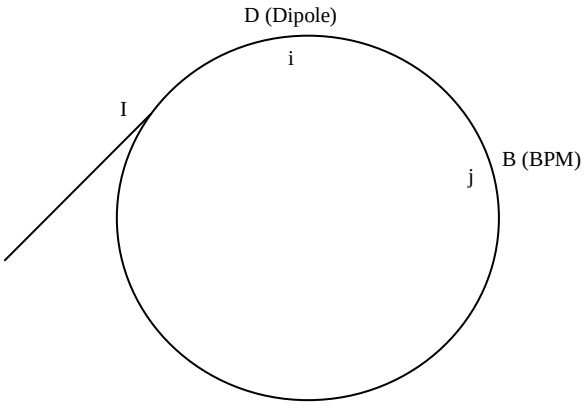

Figure 6.7: Diagram showing part of a ring with perturbation i and monitor j.

As there is no way to measure the angle of deflection θ_i, in practice, we measure ΔI, variation in current of the dipole. $\Delta\theta_i$ is proportional to ΔI_i, and then measured response matrix element $\mathcal{R}_{ij}$ can simply be related to R_{ij} by the following equation:

$$\mathcal{R}_{ij} = \frac{\Delta xCO_j}{\Delta I_i} \cong \frac{dxCO_j}{dI_i} = \frac{dxCO_j}{d\theta_i} \cdot \frac{d\theta_i}{dI_i} = -\frac{\alpha}{I} \cdot R_{ij} \tag{6.8}$$

where α is the bending angle at a dipole and I is the current leading to that bending. Therefore, there is a negative proportionality coefficient between measured and defined closed orbit response matrix elements. The response matrix $\boldsymbol{R}$ is usually a non-square matrix with N_D (number of dipoles) rows and N_{BPM} (number of BPMs) columns.

If the ring behaves linearly enough then distortion vector $\boldsymbol{CO}$ (at BPMs) can be related to perturbation current vector $\Delta\boldsymbol{I}$ at the dipoles according to:

$$\boldsymbol{CO} = \boldsymbol{R} \times \Delta\boldsymbol{I} \tag{6.9}$$

It is obvious that by applying correction $-\Delta\boldsymbol{I}$ to dipoles, opposite sign distortions are produced and thus, overall, zero distortion for closed orbit is gained at least at the BPMs. To find $\Delta\boldsymbol{I}$, we should calculate the Singular Value Decomposition (SVD) of **R**. To put it simply, SVD gives the inverse of a Non-Square matrix. As it is shown in the [63], the SVD of $\boldsymbol{R}$ is:

$$SVD(\boldsymbol{R}) = ((\boldsymbol{R^T} \times \boldsymbol{R})^{-1} \times \boldsymbol{R^T}) \tag{6.10}$$

And therefore $\Delta\boldsymbol{I}$ can be obtained as:

$$\Delta\boldsymbol{I} = ((\boldsymbol{R^T} \times \boldsymbol{R})^{-1} \times \boldsymbol{R^T}) \times \boldsymbol{CO} \tag{6.11}$$

The correction steering current vector, $\boldsymbol{I_c}$ is, then, calculated as:

$$\boldsymbol{I_c} = \boldsymbol{I} - \Delta\boldsymbol{I} \tag{6.12}$$

To sum up the whole RM based steering procedure: The response matrix $\boldsymbol{R}$ and closed orbit position vector $\boldsymbol{CO}$ (x or y) are measured and then by plugging them into Eq. (6.10) we receive the correction vector $\Delta\boldsymbol{I}$ necessary to make the Mean Square error of orbit (rms of closed orbit) minimum.

One of the problems encountered in RM based beam control is that correction currents sometimes are out of range. Based on analysis done in this work, a procedure was developed for bringing back out of range correction currents. I successfully applied CO-RM method for beam steering and could acquire very smooth and bump-free closed orbits. I also investigated the linear behavior of the ring and introduced some linear signatures for the ring. The reference [64] covers such linearity studies done for UMER.

6.3.2 Most Effective Dipoles Based Orbit Control

As the RM method was so dependent on initial good linear conditions to work well, I investigated another beam orbit control approach called the Most Effective Dipoles (MED) [42]. The MED strategy simply adjusts current of the most effective dipoles by small predefined amount ΔI in each step. To find the most effective dipoles, MED applies $\pm\Delta I$ perturbation to all N_D dipoles (of one plane) and calculates RMS of the closed orbit for $2 \cdot N_D$ possible settings. A dipole with minimum rms of the closed orbit for one of its applied perturbations is considered as most effective dipole. Only the MED is corrected by $+\Delta I$ or $-\Delta I$ at each step. The process is continued until the target rms of closed orbit is achieved, or further reduction in the rms of closed orbit seems impossible.

The major advantage of MED in comparison to RM based orbit correction is its lower susceptibility to linear behavior of the beam. The fact that the RM technique perturbs current of

each dipole by several $\Delta I's$ to measure the derivative of position to perturbation i.e. $\frac{\Delta x}{\Delta I}$ means that current setting should be good enough for the beam not being scrapped off at the edges of perturbation interval. This implies that orbits currently residing in linear domain of the ring are correctable by RM method. On the other hand, MED does not need good linear response to perturbation. However, since MED corrects orbit slowly over many steps, the whole orbit control based on solely MED takes a longer time to complete.

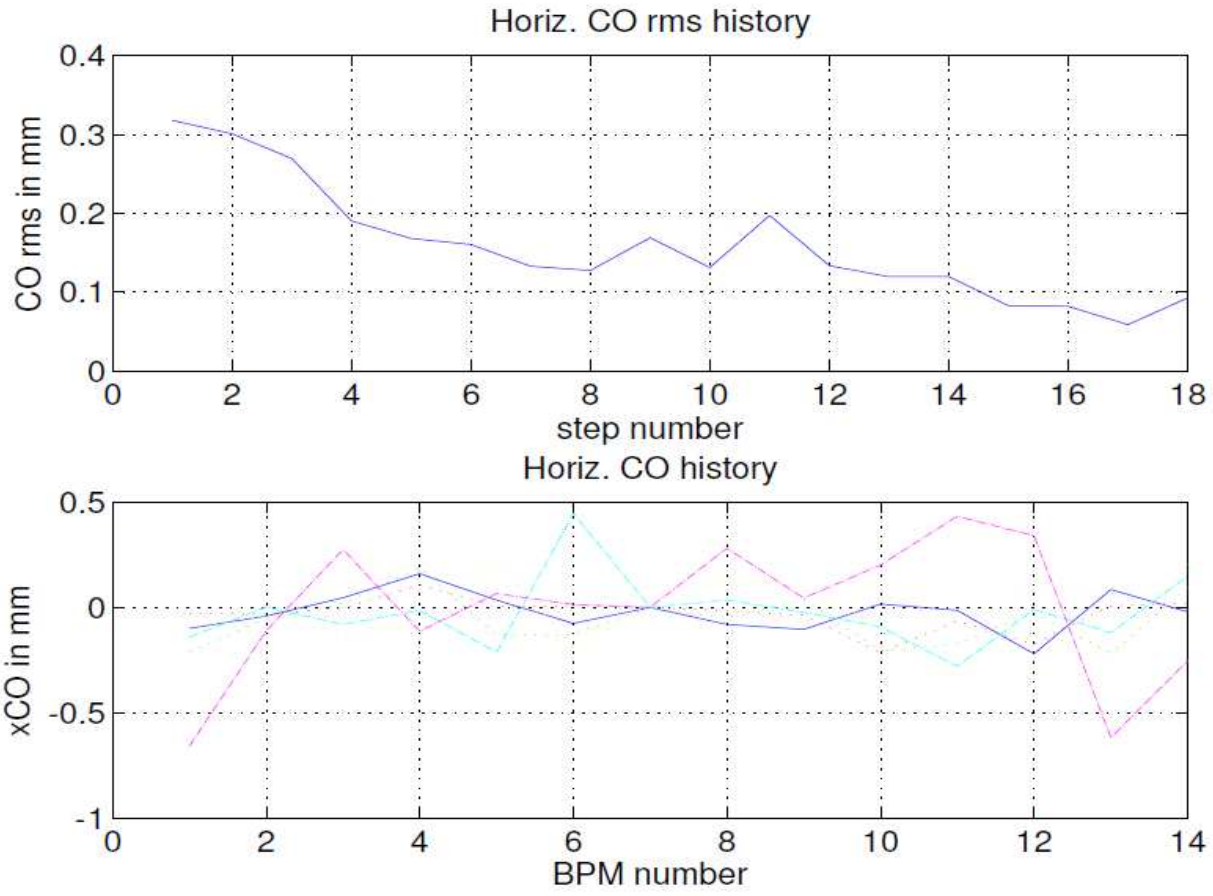

Figure 6.8: The upper graph shows how RMS of closed orbit in x plane convergences toward its minimum in MED. The lower graph shows various intermediate xCOs. The blue curve is closed orbit with minimum rms.

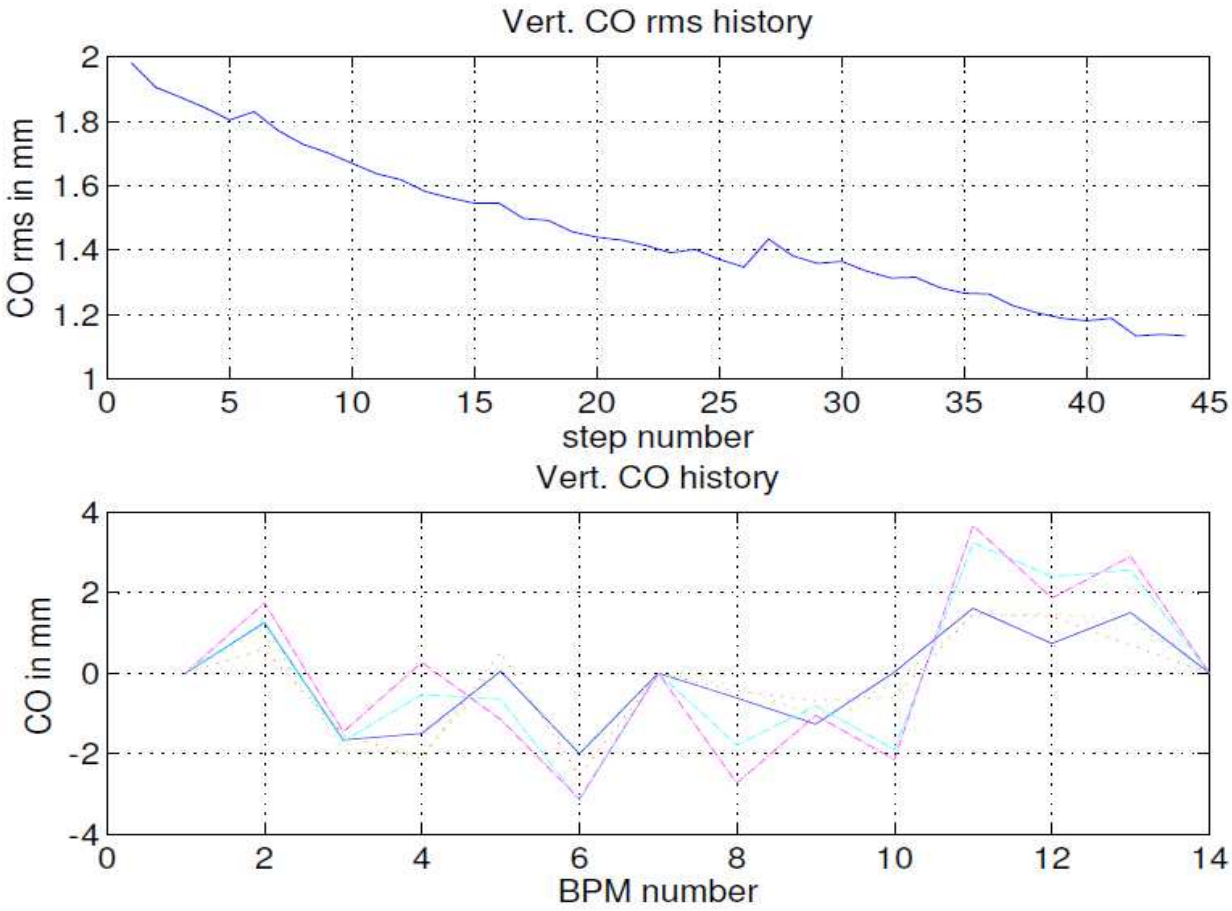

Figure 6.9: The upper graph shows how rms of closed orbit in y plane convergences toward its minimum in MED. The lower graph shows various intermediate yCO. The blue curve is closed orbit with minimum rms.

Results of employing MED orbit corrections are shown in figures 6.8 and 6.9. As can be seen in the horizontal case, the rms of the closed orbit is reduced about 75% from 0.32 mm to 0.08 mm over 17 steps. The final closed orbit is well inside the range of ± 0.1 mm. The MED method can simply be extended to modify several of most effective dipoles at each step. The MED strategy modifying a set of most effective dipoles offers a faster convergence provided the step ΔI is chosen appropriately. In addition, the p-norm of the closed orbit defined below can be

used as quality indicator of the closed orbit instead of the RMS. The p-norm of closed orbit is defined as:

$$p - norm(CO) = \sqrt[p]{\sum_{i=1}^{N_{BPM}} \frac{CO(i)^p}{N_{BPM}}} \tag{6.13}$$

where $CO(i)$ denotes the i-th sample of the closed orbit in x or y plane.

As can be seen p-norm simply reduces to RMS when $p = 2$. Higher p's give greater weight to large closed orbit samples and thus they are made smaller faster than other samples. Therefore, higher values of p may be used if there is a large variance in closed orbit samples. Otherwise, there is not much advantage in comparison to the rms of the closed orbit.

6.4 Fine Tuning Beam Injection

6.4.1 Minimizing Betatron Amplitude

While a good beam centroid alignment leading to a smooth closed orbit is an essential part for prolonging the beam lifetime, it is not sufficient. As discussed earlier, the beam excursions are due to both the average and the amplitude of the betatron oscillations. A good quality closed orbit removes the contribution from the average or DC part, while it remains the task of optimizing beam injection to reduce the amplitude or AC part. According to the figure 6.10, it can easily be checked that if at the first location where injected beam intercepts the closed orbit (in x or y plane) beam paths are not tangent, then they can never be tangent somewhere else in the ring.

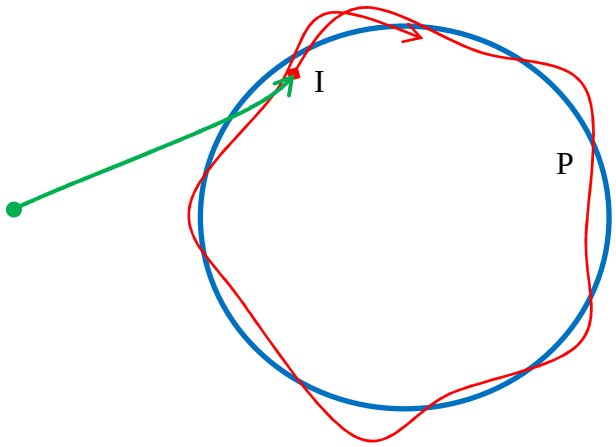

Figure 6.10: diagram showing injection off the closed orbit.

This is because:

$$\begin{cases} \begin{bmatrix} x_P \\ \acute{x}_P \end{bmatrix} = M_{IP} \times \begin{bmatrix} x_I \\ \acute{x}_I \end{bmatrix} \\ \begin{bmatrix} x_P \\ \acute{x}_P \end{bmatrix} = M_{IP} \times \begin{bmatrix} x_{CI} \\ \acute{x}_{CI} \end{bmatrix} \end{cases} \tag{6.14}$$

Where $\begin{bmatrix} x_P \\ \acute{x}_P \end{bmatrix}$ is the beam coordinates at the location P, $\begin{bmatrix} x_I \\ \acute{x}_I \end{bmatrix}$ is the beam coordinates at the injection point I, $\begin{bmatrix} x_{CI} \\ \acute{x}_{CI} \end{bmatrix}$ is the closed orbit coordinates at the injection point I, and $M_{IP}$is the transfer matrix from I to P. Therefore, if the two paths match (in both distance and slope coordinates) at a location like P, they should match all over the closed orbit.

My scheme for optimum beam injection is based on the MED method. The control set includes last two dipoles in the injection section (SD5H/V and SD6H/V in UMER). The error signal is simply the betatron amplitude which is fixed around the ring. It should be noted that span of betatron oscillations at each BPM denoted by x_i is less than betatron amplitude, a_β, due

to the different betatron phase of BPMs. Technical note [65] discusses derivations for amplitude, a_β. In summary, a_β, can be calculated as:

$$a_\beta = \frac{\sqrt{(x_1 - x_{CO})^2 + (x_2 - x_{CO})^2 - 2.(x_1 - x_{CO}).(x_2 - x_{CO}).\cos(2\pi\nu)}}{|\sin(2\pi\nu_x)|} \tag{6.15}$$

Where x_i denotes betatron sample at turn i, x_{CO} is closed orbit at location of the BPM, and ν_x is the tune of horizontal plane. The average value over all measurements is a good representation of a_β. Each step of MED would lower a_β, so that eventually, a minimum (ideally to be 0) is reached in the final step.

6.4.2 Optimizing Orbit in Transport Line of UMER

For a long time, it was well known that the beam was not passing though the center of quadrupoles in the injection. When conducting a beam matching, e.g. the empirical matching, the change of quads strength will affect the beam centroid motion and eventually the betatron oscillation of the beam in the ring. Here we show a localized method to correct the beam centroid in the injection.

According to Eq. (6.6), for x_Q, beam position inside a quadrupole, we can write:

$$\alpha \cdot x_Q = \frac{\Delta x_B}{\Delta I_Q} \tag{6.16}$$

Where

$$\alpha = \frac{l \cdot q \cdot g}{P \cdot I} \cdot \mathrm{m}_{12} \tag{6.17}$$

Similarly, there is a linear relationship between the corrector current and the beam centroid position in the quadrupole as:

$$\mathrm{x}_Q = a.I_Q + b \tag{6.18}$$

The scanning term can be determined by combining Eqs. (6.16) and (6.18) as:

$$\frac{\Delta x_B}{\Delta I_Q} = \alpha \cdot x_Q = \alpha \cdot a \cdot I_D + \alpha \cdot b \tag{6.19}$$

To let $x_Q = 0$, we need to have:

$$I_D = \frac{b}{a} = \frac{\alpha \cdot b}{\alpha \cdot a} \tag{6.20}$$

Where $\alpha \cdot a$ and $\alpha \cdot b$ can be obtained by linear fitting of the data (I_D $\frac{\Delta x_B}{\Delta I_Q}$).

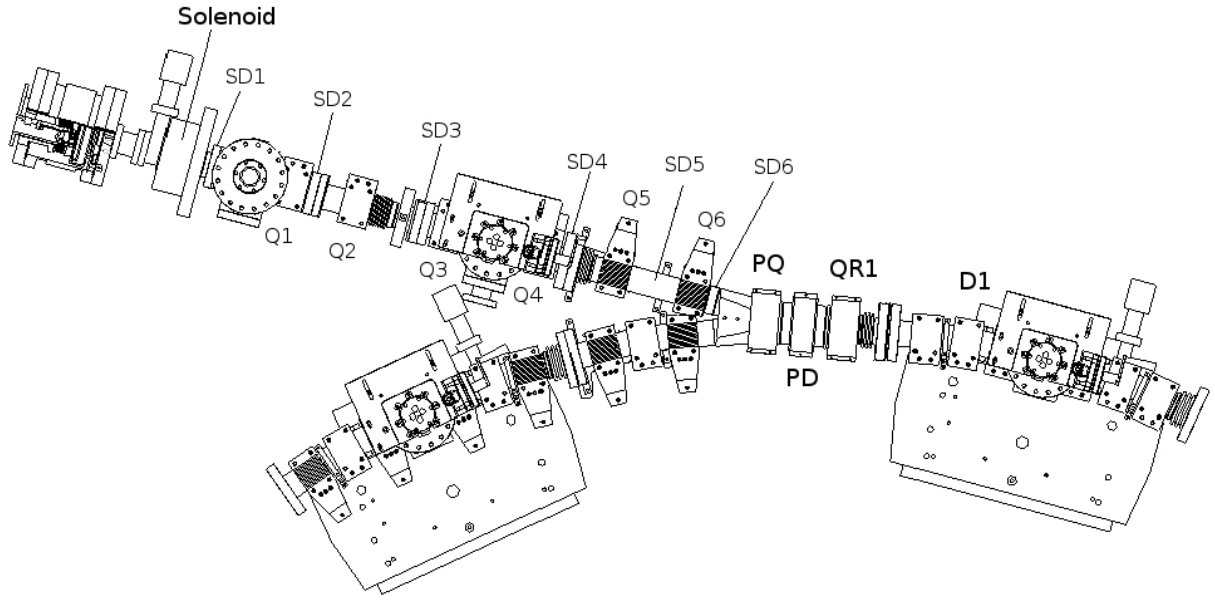

Figure 6.11: The magnet components in the injection

Figure 6.11 shows the magnet components in the injection. As can be seen, there are six dipoles and six quadrupoles hence each quadrupole can be associated with a specific~~has its own~~ corrector. For each quadrupole, we use the corrector that is before it, and the corrector and the quadrupole pair should have enough space between them to avoid a large divergence of the beam centroid as shown in figure 6.12. Notice that in figure 6.12, even though the beam passes though

the center of the quadrupoles, the beam might be too close to the pipe when going to the next corrector.

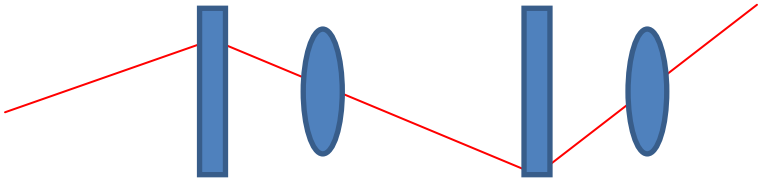

Figure 6.12: Large divergence generated by a pair of quadrupole and corrector being too close to each other.

Applying these criteria, we can have the pairs (SD1, Q2), (SD2, Q3), (SD3, Q4), (SD4, Q6). In the reality, the beam is almost correct to center of the pipe through the first two correctors. The result of this correction is listed in table 6.1.

Table 6.1: Values for the SD correctors for beam centroid correction in the injection.

Dipole	**Value / A**
SD1	-0.12
SD2	-0.79
SD3	-0.11
SD4	-1.63

Appendix A

Relation between Beam Envelope Parameters at Lens with Its Focal Length

According to the figure 1, the beam envelope slopes at entry and exit of the lens represent particle trajectories tangent to envelope right before and after the lens. Entry and exit beam coordinates are related by the transfer matrix of converging thin-lens with the focal length f through:

$$\begin{bmatrix} R_0 \\ R'_0 \end{bmatrix} = \begin{bmatrix} 1 & 0 \\ -\frac{1}{f} & 1 \end{bmatrix} \times \begin{bmatrix} R_0 \\ R'_C \end{bmatrix} \tag{A1}$$

This leads to:

$$R'_0 = -\frac{R_0}{f} + R'_C \tag{A2}$$

Or alternatively:

$$\frac{1}{f} = \frac{R'_C - R'_0}{R_0} \tag{A3}$$

It should be noted that in a quad-scan experiment R'_C and R_0 remain unchanged throughout the scan process, while the R'_0 follows variations in f.

Bibliography

[1] B. E. Carlsten., J. C. Goldstein, P. G. O'Shea, and E. J. Pitcher, "Measuring emittance of non-thermalized electron beams from photoinjectors," *Nuclear Instruments and Methods in Physics Research*, Section A 331, 791 (1993).

[2] C. Eckman *et al.*, "Development of an Automatic MATLAB based Emittance Measurement Tool for the IAC Accelerators," *in Proceedings of the IPAC 2012*, 2012.

[3] E. Chiadroni *et al.*, "High Energy Emittance Measurement at SPARC," *in Proceedings of the DIPAC 2009*, pp 402-404, 2009.

[4] R. Spesyvtsev, *et al.*, "A transverse slice emittance measurement system using quadrupole scan technique and streak readout at PITZ, in Proceedings of the FEL 2008, Gyeongju, S. Korea, August (2008).

[5] C. Thomas *et al.*, "Single shot transverse emittance measurement from OTR screen in a drift transport section," *Journal of Instrumentation* 6 (2011) P07004.

[6] C. G. Limborg, S. M. Gierman, and J. G. Power, "A Modified Quad Scan Technique for Emittance Measurement of Space Charge Dominated Beams," *in Proceedings of the IEEE PAC 2003*, pp. 2667-2669, May 2003.

[7] P. A. P. Nghiem *et al.*, "Studies of Emittance Measurement by quadrupole Variation for the IFMIF-EVEDA High Space Charge Beam," *in Proceedings of the IPAC 2011*, pp. 652-654, 2011.

[8] C. Lejeune and J. Aubert, "Emittance and Brightness: Definitions and Measurements," *Advances in Electronics and Electron Physics*, Supplement 13A, pp. 159-259 (1980).

[9] R. B. Fiorito and D. W. Rule, "Optical transition radiation beam emittance diagnostics", *AIP Conf. Proc. 319*, p. 21-37 (1994).

[10] A. Shkvarunets and R. Fiorito, "Optical synchrotron and edge radiation diagnostics for relativistic electron beams", *AIP Conf Proc. 732*, 11th Beam Instrumentation Workshop, T. Shea and R. Shipley eds., p.429-436 , (2004).

[11] R. B. Fiorito, A. G. Shkvarunets, T. Watanabe, V. Yakimenko, and D. Snyder, "Interference of diffraction and transition radiation and its application as a beam divergence diagnostic," *Phys. Rev. ST Accel. Beams*, Vol. 9, pp. 052802, (2006).

[12] M. Holloway, R. B. Fiorito, A.G. Shkvarunets, S. V. Benson, D. Douglas, P. Evtushenko and K. Jordan, "Measurements of multiple components in the JLAB ERL electron beam with optical transition and diffraction radiation", *Phys. Rev. ST Accel. and Beams*, Vol. 11, 082801 (2008).

[13] P.G. O'Shea, M. Reiser, R.A. Kishek, et. al., "The University of Maryland Electron Ring (UMER)," *Nuclear Instruments and Methods A464*, 646-652, 2001.

[14] R.A. Kishek, *et al.*, "The University of Maryland Electron Ring (UMER) enters a new regime of high-tune-shift rings," *Proc. Part. Acc. Conf.*, Albuquerque, NM, USA, 2007.

[15] C. F. Papadopoulos, R. B. Fiorito, et. al "Determination of true *rms* emittance from OTR measurements," *Proceedings of PAC 2009*. (2009).

[16] D. Stratakis, R. A. Kishek, H. Li, S. Bernal, M. Walter, B. Quinn, M. Reiser, and P. G. O'Shea, "Tomography as a diagnostic tool for phase space mapping of intense particle beams," Phys. Rev. ST Accel. Beams 9, 112801 (2006).

[17] K. Tian, Doctoral Dissertation, University of Maryland, 2008.

[18] S. G. Anderson, J. B. Rosenzweig, G. P. LeSage, and J. K. Crane, "Space-charge effects in high brightness electron beam emittance measurements," *Phys. Rev. ST Accel. Beams*, Vol 5, 014201 (2002).

[19] A. U. Luccio, "Computer Study of Harmonic Orbit Correction in the AGS Booster," AD Booster Technical Note, No. 131, Oct. 1988.

[20] A. Friedmann and E. Bozoki, "Eigenvector Method for Optimized Orbit Correction", AIP Conference Proceedings, 315, Upton, NY, 1993.

[21] J. Safranek, "Experimental Determination of Storage Ring Optics Using Orbit Response Measurements," Nuclear Instruments and Methods in Physics Research A, 388, pp 27-36, 1997.

[22] J. Safranek, "Linear Optics From Closed Orbits (LOCO)-An Introduction," Beam Dynamics Newsletter, No. 44, International Committee for future Accelerators, Issue Editor, Dec. 2007.

[23] H. Li, "Control and Transport of Intense Electron Beams," PhD dissertation, University of Maryland, College Park, 2004.

[24] M. Walter, et. al, *"Beam Control and Steering in the University of Maryland Electron Ring (UMER),"* Proceedings of 12th Workshop on Advanced Accelerator Concepts (AAC), Lake Geneva, WI, 10-15 July, 2006.

[25] M. Walter, et. al, *"Multi Turn Operation at the University of Maryland Electron Ring (UMER),"* Proceedings of Particle Accelerator Conference, Albuquerque, New Mexico, 2007.

[26] C. Wu, E.H. Abed, B. Beaudoin, S. Bernal,I. Haber, R.A. Kishek, C. Pa- padopoulos, M. Reiser, D. Sutter, and P.G. O'Shea, "A Robust Orbit-Steering and Control Algorithm Using Quadrupole-Scans as a Diagnostic," Proceedings of the 2007 IEEE Particle Accelerator Conference, Albuquerque, New Mexico, 2007.

[27] C. Wu, "Precision Control of Intense Electron Beams in a Low-Energy Ring" PhD dissertation, University of Maryland, College Park, 2009.

[28] Martin Reiser, *Theory and Design of Charged Particle Beams* (Wiley, New York, 2008).

[29] E. Wilson, *An Introduction to Particle Accelerators,* Oxford University Press, New York, 2001.

[30] R. A. Kishek, *Beam Physics Lecture Notes,* Fall 2011.

[31] E.D. Courant and H.S. Snyder, *"Theory of the Alternating-Gradient Synchrotron,"* Annals of Physics, Volume 281, Issue 1-2, pp 360-408, 2000.

[32] F.J. Sacherer, "RMS Envelope Equations with Space Charge", IEEE Transaction on Nucl. Sci. NS-18, 1105 (1971).

[33] Michiko G. Minty and Frank Zimmerman, *Measurement and Control of Charged Particle Beams* (Springer-Verlag, New York, 2003).

[34] The Mathworks Inc., www.mathworks.com.

[35] G. J. Borse, *Numerical Methods with MATLAB* (PWS Publishing Company, 1997).

[36] J.D. Jackson, *Classical Electrodynamics,* John Wiley & Sons Inc., 1999.

[37] I.M. Frank and V.L. Ginsburg, "Transition Radiation and Transition Scattering",*Journal of Phys*ics, vol. 9 (1945) p 353.

[38] R. B. Fiorito, Private Communication, 2012-13.

[39] A. Shkvarunets, R. Fiorito, P. O'Shea, J. Power, M. Conde, and W. Gei, "Optical diffraction-dielectric foil radiation inter- ferometry diagnostic for low energy beams," in *IEEE Particle Accelerator Conference, 2007. PAC*, pp. 4012–4014, 2007.

[40] R.A. Kishek, Private Communication, 2011-13.

[41] C. G. Limborg, SLAC Summer school lecture notes, 2013.

[42] J. Koutchouk, *"Trajectory and Closed Orbit Correction,"* Frontiers of Particle Beams: Observation, Diagnosis and Correction, Proceedings, Anacapri, soladi Capri, Italy, (Lectures Notes in Physics 343, M. Month, S. Turner Eds), p46, 1988.

[43] M. Sands, "The Physics of Electron Storage Rings – An Introduction", SLAC-121, 1970.

[44] D. Sutter, Earth's Magnetic Field Measurements 2004-2009, Technical Data, www.umer.umd.edu, 2009.

[45] D. Sutter, Private Communication, 2011-13.

[46] http://www.aai.anl.gov/history/project_pages/awa.html.

[47] J. G. Power, Private Communication, 2012-13.

[48] K. Poor Rezaei, R. B. Fiorito, R. A. Kishek, and B. L. Beaudoin "New Technique to Measure Emittance for Beams with Space Charge", *Physical Review Special Topics – Accelerators and Beams*, Vol. 16, 082801, 2013.

[49] K. Poor Rezaei, R. B. Fiorito, and R. A. Kishek "A Novel Technique to Measure Emittance for Beams with Space Charge", *Proceedings of NAPAC-13*, 2013.

[50] S. M. Lund and B. Bukh, "Stability properties of the transverse envelope equations describing intense ion beamtransport," *Phys. Rev. ST Accel. Beams*, Vol 7, 024801 (2004).

[51] *A. Friedman*, "Simulation of Intense Beams for Heavy Ion Fusion," *Nucl*. *Instrum*. Meth. *Phys*. *Res*. *A544*, *160*, (*2005).*

[52] http://hif.lbl.gov/theory/WARP_summary.html.

[53] Goodness-of-fit: www.mathworks.com/help/curvefit/evaluating-goodness-of-fit.html.

[54] D. Stratakis, R.A. Kishek, I. Haber, S. Bernal, M. Reiser, and P.G. O'Shea, "Experimental Study of Phase Mixing of Intense Nonlinear Beam Distributions," *Phys. Rev. ST Accel. Beams*, Vol. 12, 064201 (2009).

[55] K. Poor Rezaei, R. B. Fiorito, and R. A. Kishek "Novel Approach for Measuring Emittance of Beams with High Space Charge", submitted to *Physical Review Special Topics – Accelerators and Beams*.

[56] L. Young and J. Billen, "The Particle Tracking Code Parmela," Proceedings of the Particle Accelerator Conference, Vol. 5, pp. 3521 – 3523, 2003.

[57] http://laacg.lanl.gov/laacg/services/serv_codes.phtml#parmela.

[58] M. E. Conde, "Survey of Advanced Dielectric Wakefield Accelerators," Proceedings of the Particle Accelerator Conference, pp. 1899-1903, 2007.

[59] H. Zhang and K. Poor Rezaei, "Beam Centroid Correction in the Injection", Technical Note UMER-2012-3-25-HZ-KPR, March 2012.

[60] P. Bryant and K. Johnson, The Principles of Circular Accelerators and Storage Rings, Cambridge University Press, 1993.

[61] K. Poor Rezaei, "Non Noise-Prone Formulas for Closed Orbit", Technical Note 4, August 2011.

[62] K. Poor Rezaei, "Measuring Beam Centroid Position Inside Quadrupoles", Technical Note 7, March 2012.

[63] K. Poor Rezaei, "Minimum Perturbation For Correcting Orbit", Technical Note 3, July 2011.

[64] K. Poor Rezaei, "Studying Inter-turn Response Matrix Parameters Variation", Technical Note 2, August 2011.

[65] K. Poor Rezaei, "Measuring Betatron Amplitude", Technical Note 8, December 2012.